NUMERICAL SIMULATION ON AERODYNAMICS OF A SUPERSONIC FLEXIBLE PARACHUTE SYSTEM USING A FLOW AND STRUCTURE COUPLING METHOD

Xiaopeng XUE

NUMERICAL SIMULATION ON AERODYNAMICS OF A SUPERSONIC FLEXIBLE PARACHUTE SYSTEM USING A FLOW AND STRUCTURE COUPLING METHOD

Xiaopeng XUE

Department of Aerospace Engineering

Nagoya University

A Dissertation
submitted for the degree of
Doctor of Engineering

2013

Abstract

The present doctoral thesis basically treats the supersonic flow over a parachute system, where the compressible Navier-Stokes equations are numerically solved. The parachute system employed here consists of a capsule and a canopy. In some cases with a relatively small trailing distance between the capsule and the canopy, the flow field around a parachute model shows complex flow patterns including wake/shock and/or shock/shock interactions. Therefore, the objective of the present thesis is to investigate the effects of such wake/shock and shock/shock interactions on the flow fields, and the aerodynamics and shape of the canopy associated with the performance of the parachute system, where rigid or flexible canopies are employed.

In the rigid canopy case, three-dimensional calculations were performed for two models: Model A and Model B. The former is the same as the experiment, where the canopy is connected with the capsule by a rod, and the whole system is supported by another rod, while the latter does not have these rods. Numerical results show good agreement with the experimental data in the case of the model A. In addition, it is found that the differences in flow feature between the models A and B are rather small. On the other hand, the unsteady flow pulsation phenomenon was observed here in this study. In the development of this phenomenon, the bow shock is first formed ahead of the capsule, and then inflates periodically and moves outward in the radial direction. This is caused by upstream propagation and lateral expansion of the complicated capsule wake/rear shock and foreshock/rear shock interaction systems.

In the flexible canopy case, two-dimensional, axisymmetric and three-dimensional calculations were performed, using the immersed boundary method in the fluid-structure coupling scheme. The mass-spring-damper

(MSD) model was applied to solve the structural dynamics of the flexible canopy. The objective of this study is to analyze the effects of aerodynamic interference such as wake/shock interaction on the canopy dynamics and to examine the effects of parameters such as Mach number, the ratio of the diameter of the capsule to that of the canopy, and the trailing distance between the capsule and canopy. As a result, it is found that the immersed boundary method works well to solve supersonic flexible parachute problems.

In the two-dimensional parachute case, only the steady foreshock and the wake/rear shock interaction were observed, which was produced by the weak interference and large deformation of the canopy. In addition, in the axisymmetric parachute case, the complicated wake/rear shock and foreshock/rear shock interactions were observed. In this case, as Mach number increases, the shock wave ahead of the capsule becomes more conical in shape, which causes stronger aerodynamic interactions, and the interaction locations are closer to the canopy. As a result, the canopy is subject to large deformation including shrinkage.

On the other hand, in the three-dimensional flexible parachute case, it is found that there are two key factors for the parachute dynamics; one is the unsteady change in the canopy shape and the other the aerodynamic interference between the capsule wake and the canopy shock. As the trailing distance relatively increases, the phenomenon of " canopy area oscillation" was generated; however, reducing the canopy size in the case of relatively small trailing distance, the canopy was less deformed. In addition, when Mach number was reduced to Mach 1.6, the canopy was also less deformed, due to the weaker interactions between the capsule wake and the canopy shock, leading to a large drag coefficient.

To Taoye

Acknowledgements

The present work was carried out in Fluid Dynamics Laboratory, Department of Aerospace Engineering, Nagoya University.

I would like to express my deepest gratitude and greatest appreciation to my advisor Prof. Y. Nakamura. I am deeply thankful for his constant encouragement and guidance, and for the knowledge and insights that he shared on my research. Sincerely thanks for contributing to my papers. I am truly grateful for all the help and support during my doctoral study.

I wish to thank Prof. K. Mori and Prof. K. Doi for their thought provoking discussions and valuable suggestions on the research. I would like to thank Prof. K. Kitamura and Dr. H. Yokoi for their interesting discussions and constructive advices. I wish to express my special thanks to my classmate Dr. Y. Wang for his patient support and helpful experiences. Many thanks to all members of Nakamura Laboratory. I would like to thank the dissertation referees, Prof. Y. Nakamura, Prof. A. Sasoh in the same department, Prof. K. Ishii from Information Technology Center, and Prof. K. Mori for their comments to improve my dissertation.

I would like to thank China Scholarship Council (CSC) for the financial support during my study in Japan. I am also thankful to Nagoya University for giving much support to my study and life.

I am grateful to Institute of Space and Astronautical Science (ISAS/JAXA) for permitting us to use the supersonic wind tunnel at ISAS.

I would like to express my great thanks to my parents for their encouragement and support during my study. I wish to express my special thanks to my wife's parents for taking care of my daughter during my stay in Japan. I would like to thank my wife, Taoye, for her love, and for her full support

and constant encouragement, especially in my most difficult times. I also thank my daughter who brings me endless joy.

Contents

List of Figures vii

List of Tables xi

Nomenclature xii

1 Introduction 1

1.1 Introduction . . . 1

1.1.1 Background . . . 1

1.1.2 Review of Related Work . . . 2

1.2 Motivation and Objective . . . 6

1.3 Thesis Outline . . . 7

2 Computational Methods 9

2.1 Introduction . . . 9

2.2 Flow Calculation . . . 9

2.2.1 3D Navier-Stokes Equations . . . 9

2.2.2 Navier-Stokes Equations in Generalized Coordinate System . . . 11

2.2.3 Axisymmetric Navier-Stokes Equations . . . 14

2.2.4 Evaluation of Inviscid Flux . . . 15

2.2.4.1 AUSM Scheme . . . 15

2.2.4.2 SHUS Scheme . . . 16

2.2.4.3 SLAU Scheme . . . 17

2.2.5 Time Advancement . . . 18

2.2.6 Boundary Conditions . . . 18

2.3 Structure Calculation . . . 19

2.4 Fluid-Structure Coupling Method 20
2.4.1 Immersed Boundary Method 23
2.4.2 Fluid-Structure Coupling Scheme 23

3 Three-Dimensional Flow Around Axisymmetric Rigid Parachute 26
3.1 Introduction 26
3.2 Rigid Parachute Models 26
3.3 The Method of Simulation 28
3.3.1 Computational Conditions 28
3.3.2 Numerical Method 28
3.3.3 Grid Generation and Grid Convergence 28
3.3.4 The Pressure Sensor in the Experiment 30
3.3.5 Validation of the Numerical Method 31
3.4 Unsteady Aerodynamic Interactions 33
3.4.1 Flow Features of Process 1 36
3.4.2 Flow Features of Process 2 36
3.4.3 Flow Features of Process 3 44
3.5 Effect of Connecting Rod 47
3.6 Effect of Mach Number 48
3.7 Summary 50

4 Two-Dimensional Flexible Parachute 52
4.1 Introduction 52
4.2 Computational Method and Conditions 52
4.3 Two-Dimensional Parachute Model 53
4.4 Canopy Shape Variation 55
4.5 Unsteady Aerodynamic Interaction 56
4.6 Effect of Mach Number 58
4.7 Summary 62

5 Axisymmetric Flexible Parachute 63
5.1 Introduction 63
5.2 Computational Method and Conditions 63
5.3 Axisymmetric Parachute Model 66

5.4 Canopy Shape Variation 67
5.5 Unsteady Aerodynamic Interaction 67
5.6 Effect of Mach Number 70
5.7 Summary 71

6 Three-Dimension Flexible Parachute **73**
6.1 Introduction 73
6.2 Computational Method and Conditions 73
6.3 Three-Dimensional Flexible Parachute Model 76
6.4 The Effect of Parachute Trailing Distance 80
6.5 The Effect of the Capsule and Canopy Size 87
6.5.1 Capsule Size 87
6.5.2 Canopy Size 92
6.6 The Effect of Mach Number 95
6.7 Summary 96

7 Conclusion **99**

Bibliography **103**

List of Figures

1.1 In MSL mission, the Curiosity and its supersonic parachute are landing to Mars surface; the inset picture shows a cutout of the Curiosity and MSL parachute [1] 2
1.2 The descent of Curiosity in MSL mission [2] 3
1.3 Instantaneous flow fields around the parachute system at different instants [3] 6

2.1 Overview of the tangential force acting on the mass nodes of flexible canopy surface, the red point is a mass node of canopy surface 20
2.2 MSD model of the canopy from Fig. 2.1 21
2.3 The normal force acting on the mass nodes of flexible canopy surface . . 22
2.4 Velocity vectors in fluid and virtual cell [4] 22
2.5 Relationship between the velocities of fluid and virtual cell [4] 23
2.6 The fluid-structure coupling method used in this study [90] 24
2.7 The fluid-structure coupling scheme 25

3.1 Models used in the present computation 27
3.2 Grids for parachute models 29
3.3 Pressure change due to grid 30
3.4 The location of point A inside the canopy 32
3.5 Comparison of the experimental averaged pressure data and CFD time-resolved data of point A (see Fig. 3.4) 32
3.6 Numerical pressure histories at point Q (see Fig. 3.1), A, B, C and D correspond to the time locations shown in Fig. 3.7 33

3.7 Shadowgraph pictures (left) and the corresponding density gradient contours in simulation (right) 34
3.8 Averaged pressure distribution on surfaces of Model A 35
3.9 Pulsation mode for Mach of 2.0: Mach number contours(left) and pressure contours (right)(cont'd) 37
3.9 Pulsation mode for Mach of 2.0: Mach number contours(left) and pressure contours (right)(cont'd) 38
3.9 Pulsation mode for Mach of 2.0: Mach number contours(left) and pressure contours (right)(cont'd) 39
3.9 Pulsation mode for Mach of 2.0: Mach number contours(left) and pressure contours (right) 40
3.10 Time variations of pressure at two different places in Mach 2.0 pulsation case 41
3.11 Schematic of the flow field in process 1, based on frame 2 of Fig. 3.9 . . 42
3.12 Schematic of the flow field in process 2, based on frame 6 of Fig. 3.9 . . 43
3.13 Velocity vectors and pressure contours near the corner of canopy in frame 4 43
3.14 Velocity vectors and pressure contours in the interaction region, based on frame 6 of of Fig. 3.9 44
3.15 Schematic of the flow field in the early stage of process 3, based on frame 8 and 9 of Fig. 3.9 45
3.16 Schematic of the flow field in the late stage of process 3, based on frame 13 of Fig. 3.9 46
3.17 Comparison of averaged pressure distribution on typical surfaces between model A and model B 47
3.18 Mach number contours of model B in two instantaneous flow fields: frame 6 (left) and frame 8 (right) 48
3.19 Mach number contours of model A in two instantaneous flow fields for Mach 1.6 case 49
3.20 Mach number contours of model A in two instantaneous flow fields for Mach 2.2 case 49
3.21 Effect of Mach number on averaged pressure distribution on parachute surfaces 50

4.1 Two-dimensional parachute model 54
4.2 Time variations of canopy shape 54
4.3 Pressure contours at four different times 55
4.4 Time variations of pressure coefficient at point A (see Fig. 4.1) 56
4.5 Time variations of payload force on two sides 57
4.6 Time variations of pressure coefficient of point A inside the canopy (see Fig. 4.1) at three Mach number cases 58
4.7 Comparison of canopy shape at two different times for the Mach number cases 59
4.8 Pressure contours at three different times at Mach 1.6 60
4.9 Pressure contours at two different times at Mach 2.1 61

5.1 Time variations of canopy shape 64
5.2 Density gradient contours around the flexible parachute at Mach 2.0; T is a period 65
5.3 Time history of projected frontal area of canopy 66
5.4 Pressure coefficient at point A (see Fig. 4.1 of Chapter 4) on the canopy surface 66
5.5 Time history of payload force 67
5.6 Density gradient contours around the flexible parachute at Mach 1.6; T is a period 68
5.7 Density gradient contours around the flexible parachute at Mach 2.1; T is a period 69
5.8 Comparison of pressure coefficient at point A (see Fig. 4.1 of Chapter 4) on the canopy surface for the effect of Mach number 69
5.9 Comparison of time variations of projected frontal area of canopy for the effect of Mach number 70

6.1 Parachute system in the present computation 74
6.2 Grid for case C (see Table 6.1) in this study, the yellow region refers to the capsule body, and the red region the canopy surface. 74
6.3 Time-variations of canopy shape for case A 75
6.4 Time-variations of canopy shape for case B 76
6.5 Time-variations of canopy shape for case C 77

6.6 General flow features around the parachute systems. Mach number contours for cases A , B and C at one instant in time(cont'd) 78
6.6 General flow features around the parachute systems. Mach number contours for cases A, B and C at one instant in time 79
6.7 Pressure cycle on parachute canopy for case C 80
6.8 The comparison of drag coefficient for cases A, B and C 81
6.9 Time-variations of canopy shape for case D 82
6.10 Time-variations of canopy shape for case E 83
6.11 Force analysis of edge parts in the cross section (y=0) of the parachute system 84
6.12 Instantaneous pressure contours around canopy for cases D and E . . . 85
6.13 Time history of drag coefficient for cases A, D and E 86
6.14 Time-variations of canopy shape for case F 87
6.15 Time-variations of canopy shape for case G 88
6.16 Instantaneous pressure contours around canopy for cases F and G . . . 89
6.17 Time history of drag coefficient for cases B, C, F and G 90
6.18 Time-variations of canopy shape for case H 91
6.19 Time-variations of canopy shape for case I 92
6.20 Instantaneous pressure contours around canopy for cases C, H and I(cont'd) 93
6.20 Instantaneous pressure contours around canopy for cases C, H and I . . 94
6.21 Time history of drag coefficient for cases C, H and I 94

List of Tables

3.1 Freestream conditions employed in the present study 28
3.2 Grid used for grid convergence 30
3.3 The specification of pressure sensor used in this study [5] 31
3.4 Comparison of Strouhal numbers 31

6.1 Specification for three cases A, B and C 78
6.2 Values of parameters for cases D and E 88
6.3 Values of parameters for cases F and G 92
6.4 Values of parameters for cases H and I 95

7.1 Comparison between rigid and flexible parachute cases with respect to aerodynamic interference for Mach of 2.0 (“$\circ$” = occur, “$\times$” = does not occur) 99

Nomenclature

Roman Symbols

c	speed of sound, m/s
C_d	drag coefficient
C_p	pressure coefficient
D	diameter of canopy, mm
d	diameter of capsule front surface, mm
d_1	diameter of connecting rod, mm
d_2	diameter of supporting rod, mm
f	frequency, Hz
h	thickness of canopy, mm
M	Mach number
M_∞	freestream Mach number
P	pressure, Pa
P_0	total pressure, Pa
P_∞	freestream pressure, Pa
q	dynamic pressure, N/m^2
q_∞	freestream dynamic pressure, N/m^2

R specific gas constant for air

Re Reynolds number

St Strouhal number

t dimensional time, s

T_0 total temperature, K

U, V, W contravariant velocities

u, v, w velocities in x, y, z directions, respectively, m/s

X axial distance from capsule front surface to canopy inlet, mm

x, y, z Cartesian coordinate system, mm

X/d trailing distance

Greek Symbols

γ specific heat ratio for air

μ dynamic viscosity, Pa·s

ρ density, kg/m^3

τ pseudo-time

ξ, η, ζ generalized coordinate system

Subscripts

0 total value

∞ freestream value

Chapter 1

Introduction

1.1 Introduction

1.1.1 Background

The Mars Science Laboratory (MSL) mission that was launched by NASA in 2011 will attempt to conduct the further investigations on the Martian surface [6]. The Curiosity, a Mars rover, successfully landed on the surface of Mars on August 6, 2012 [7]. The descent of this spacecraft into the Martian atmosphere was decelerated from the supersonic to the subsonic speed by using a supersonic parachute system [8] (see Figs. 1.1 and 1.2), due to its low mass and high ratio of aerodynamic drag [3].

In this mission, the supersonic parachute plays a very important role in the entry, descent, and landing of the Mars rover [9]. To date, all the Mars landing missions have used similar entry, descent, and landing systems so as to safely land to the surface of Mars [10]. As the capsule enters into the atmosphere of Mars, it decreases velocity by atmospheric drag; when the capsule becomes supersonic speeds, a supersonic parachute is deployed to slow the capsule to subsonic speeds (see Fig. 1.2) [10, 11].

The supersonic decelerators for planetary entry were investigated experimentally from 1960's by the NASA [12]. In the early stage, the main purpose of the parachute programs was to define the requirements and functions of this aerodynamic decelerators, which can be used to accomplish in the further planetary exploration missions [9]. With the development of the technology, NASA qualified a Disk-Gap-Band (DGB) parachute for the Viking Lander mission to Mars [13, 14]. So far, the NASA has achieved several successful landings on Mars by using the supersonic parachute: Viking

Landers I and II successfully deployed their parachutes at Mach 1.1 for their descent into Mars atmosphere; the deployment of parachute system performed at Mach 1.7 in the Mars Pathfinder mission; and then the Mars Exploration Rover A and B deployed their parachutes with correspondent Mach numbers of 1.8 and 1.9, respectively; the Mars Phoenix system was deployed at Mach 1.9; the MSL mission employed a largest parachute, in which the deployment is planed to take place at a Mach number of 2.0. [9, 12, 15]

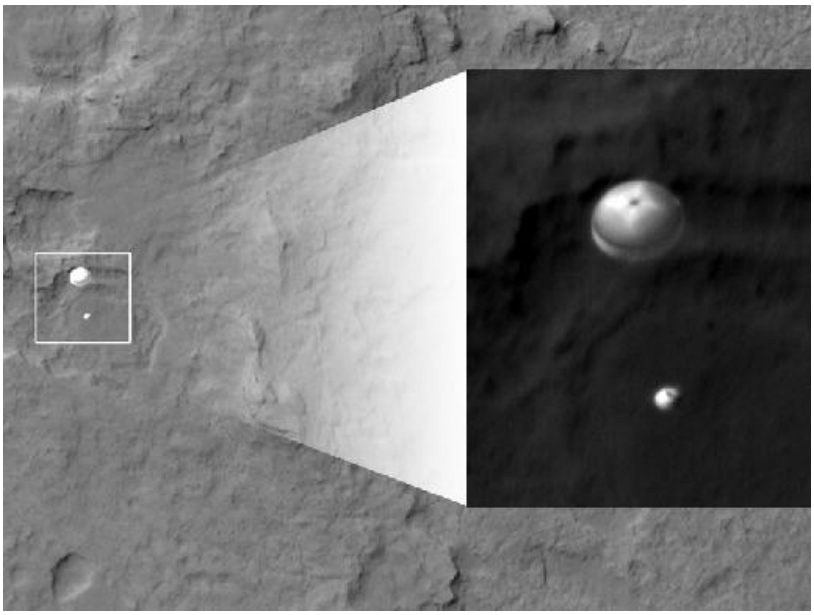

Figure 1.1: In MSL mission, the Curiosity and its supersonic parachute are landing to Mars surface; the inset picture shows a cutout of the Curiosity and MSL parachute [1]

1.1.2 Review of Related Work

Maynard [16] firstly investigated the aerodynamic characteristics of the parachutes at supersonic speeds, and found that the drag coefficient of the parachute system depends on such facts on canopy porosity, Mach number, the shape and size of drogue, and the distance between the drogue and the canopy, and revealed that the forebody wake has a big impact on the drogue-type parachute system. Johnson [17] studied that a conical-ribbon parachute system exhibited a high-frequency canopy breathing and the periodic overinflation at Mach number greater than 1.14. Maynard [18] carried out a

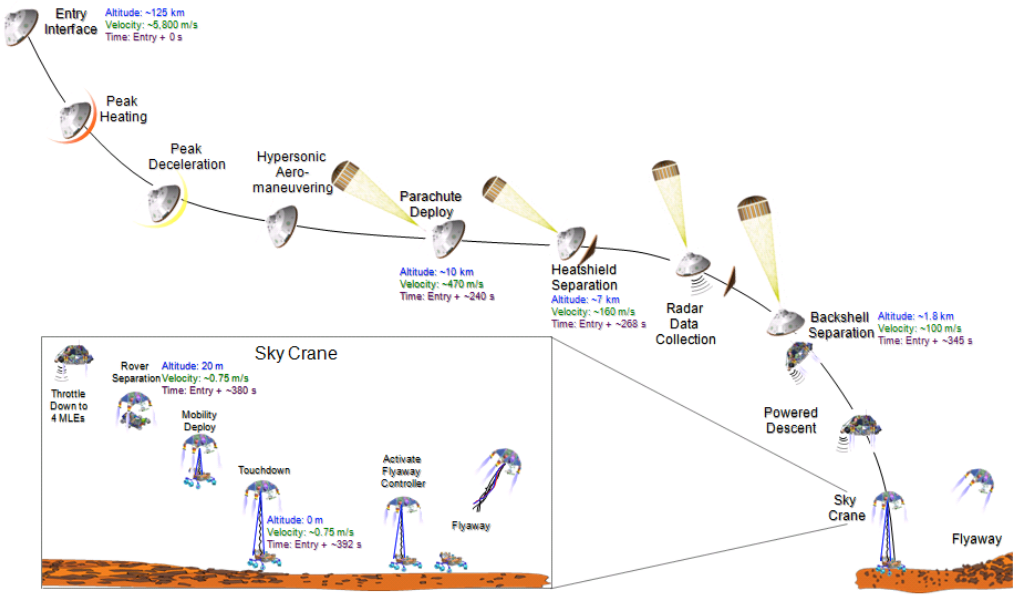

Figure 1.2: The descent of Curiosity in MSL mission [2]

wind-tunnel investigation of rigid and flexible parachute models, and found that Mach number and canopy porosity are the most important facts for the performance of the flexible parachute, and also observed the high-frequency breathing motion of the canopy, moreover, Mach number and the wake from the forebody seriously affect the drag coefficient of the rigid parachute model. Based on this results, some investigations of the improvement for supersonic decelerators were performed, including new parachute models such as conical-inlet parachutes [19], decelerator with isotensoid design [20], and the effect of angle of attack [21]. During that time, Eckstrom [22, 23] and Eckstrom et al. [24] conducted the wind tunnel and flight tests of the Disk-Gap-Band parachute system, and drew a conclusion that the DGB parachute is very stable in flight and has an effective drag coefficient.

In 1970's, for the Viking Lander mission to Mars, a series of wind-tunnel and flight tests of a Disk-Gap-Band (DGB) parachute were conducted. Maybue et al. [25] demonstrated the oscillatory drag characteristics of a DGB parachute using supersonic wind tunnel, and indicated that the parachute showed low-frequency canopy breathing, however, as Mach number increased from 2.0 to 3.0, the variations became more severe, and found that the canopy porosity has not significant effect on the parachute drag

performance, and an increase in the canopy trailing distance causes an increase in drag coefficient at Mach 2.5. Steinberg et al. [26] employed 10% scale, DGB parachute model to study the drag performance at a wide range of Mach number from 0.2 to 2.6, and examine the impact of trailing distance and the suspension line length. It was found that the forebody wake can remarkably affect the drag coefficient, and increasing the trailing distance, by changing the length of suspension line, can improve the drag performance. In addition, it was also found that a minimum drag coefficient was obtained at sonic Mach number, and the drag coefficient increases as Mach number is increased to 1.4. However, as Mach number continues to increase, the drag coefficient decreases again. Besides, several flight tests of the DGB parachute [27, 28] were carried out at supersonic, transonic, and subsonic speeds in the wake of full-scale Viking capsule, and found that the parachute canopy showed severe breathing and/or flapping motions until it reached a steady state.

Twenty years later, more experimental work of the DGB parachute were conducted for the Mars Pathfinder missions [29, 30], the Mars Exploration Rover mission [31, 32, 33, 34, 35], the Mars Phoenix mission [36, 37, 38, 39].

On the other hand, the research on the numerical simulation of supersonic parachute start relatively late, because it is very difficult, and needs to solve the problem of the separated, unsteady compressible flows around a flexible, bluff body, on the condition that the upstream is non-uniform [9]. Klimas [40, 41, 42] firstly proposed Vortex Element Methods for the simulation of the parachute canopies in an inviscid, incompressible flow. This method has been improved to be more effective and widely useful, however, so far limited for incompressible flows [9]. The early computational program for the DGB parachute system was developed to simulate the effect of the suspension line damping coefficient on the load and motion of parachute system at supersonic conditions [43], and analyze the dynamics and stability of the DGB parachute using the various parachute material compute models [44, 45]. With the development of computer technology and the advancement of numerical calculation, Computational Fluid Dynamics (CFD) technology was employed by Nelsen [46] to conduct the early research for predicting the supersonic flow field over the parachute model, where the rigid and ribbon three-dimensional parachute model in subsonic and supersonic flow were simulated by solving the compressible Navier-Stokes equations, and the results of the flow field feature and surface pressure distributions were obtained. Lafarge et

al. [47] proposed a CFD code coupled with the finite element structural analysis for a cross parachute system to compute the pressure distribution and the aerodynamic heating. And this coupled fluid structure simulation method had been developed and applied for 2D, 3D ribbon parachutes and other higher Mach parachutes by Taylor et al. [48] . The early researches on FSI coupled with Arbitrary Lagrangian Eulerian method to simulate flexible parachute system at supersonic conditions were presented by Lingard et al. [49, 50], and in which firstly showed the aerodynamic interference between the wake from the capsule and the canopy shock [9], and examined the effect of the forebody wake, Mach number and trailing distance on performance of the flexible parachute. Karagiozis et al. [3] performed well early on the simulation of large-scale flexible supersonic DGB parachute by using Large-Eddy Simulation coupled with a structural membrane based on finite element model, and reproduced the area oscillations of the canopy, which were often observed in the experiment at higher Mach number.

Moreover, it should be noted that it is the first time to use Computational Fluid Dynamics (CFD) as well as Fluid-Structures Interaction Method (FSI) to design and qualify the supersonic parachute system in the Mars Science Laboratory mission [9].

For the qualification of MSL mission, Barnhardt et al. [51] presented numerical simulation of a rigid parachute model by using the detached-eddy simulation (DES) method, and found that the time-dependent deficit in the wake interacts with the canopy shock, causing the flow field around the parachute to become highly unsteady. Using the same numerical method, Gidzak et al. [52, 53] further conducted the validation and compared with the data from wind tunnel tests, and found that the coupling of the capsule wake and the bow shock ahead of the canopy leads to a cyclic pressurization in the canopy, which causes the time variations in drag of a supersonic parachute, and further revealed that the timescale for the canopy motions is larger than the one for its drag variations. Simultaneously Sengupta et al. [8, 12, 54, 55, 56, 57, 58, 59] conducted a multi-phase validation program: 2.1% of full-scale MSL rigid parachute tests was used to qualify the high fidelity CFD codes; 4% of full-scale MSL flexible parachute test was carried out to validate the FSI code; the validated FSI tools were applied to simulate the Mars type deployment of the full-scale MSL parachute.

The complete overview of the relative work on supersonic parachute can also refer to Ref. [3] and Ref. [9].

1.2 Motivation and Objective

From the past investigations, it was found that the parachute oscillation phenomenon (see Fig. 1.3) occurs at supersonic conditions, and this area oscillations can be observed for all types of parachutes [3]. Furthermore, the drag decreases and flow instability increases apparently owing to the interaction of the capsule wake with the canopy bow shock [60].

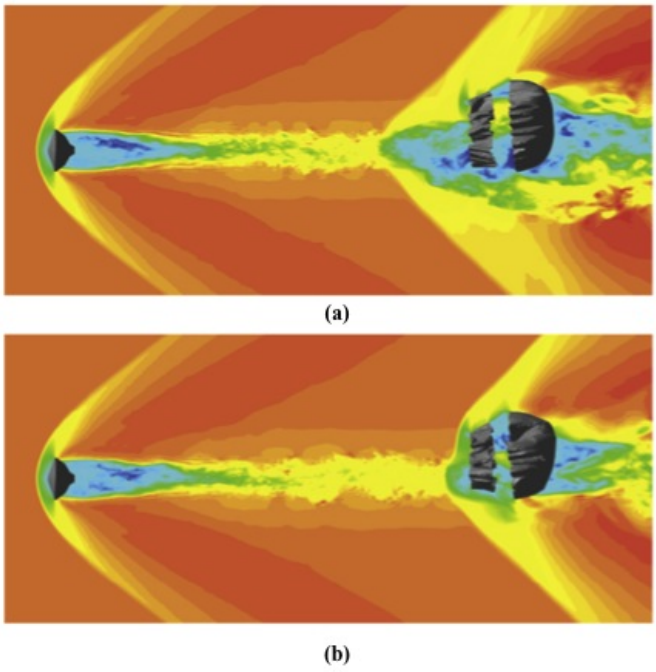

Figure 1.3: Instantaneous flow fields around the parachute system at different instants [3]

Fig. 1.3 shows a flexible parachute system in a supersonic flow, where two shocks occur in front of the capsule and canopy, respectively; and the wake-shock interaction can be observed in the region between the capsule and canopy, which causes the canopy change in shape and offers the unsteadiness in the flow field [3].

Moreover, recent experimental and numerical investigations by using subscale supersonic parachutes [12, 51, 57, 58, 59] also demonstrated that the flow instability comes from the aerodynamic interference due to the canopy bow shock and capsule wake, where the time-dependent momentum deficit of the capsule wake leads the canopy

shock change in shape, reducing mass enter into the canopy, and it depends on such facts as Mach number, Reynolds number, the forebody size, and the proximity to the forebody.

Therefore, it becomes important to fully understand the flow field interactions that take place in such two-body systems and identify those parameters that influence the aerodynamic interactions. The objective of this study is to predict the flow field and analyze the effect of aerodynamic interference on the parachutes in details, and make clear the difference between rigid and flexible cases, and use these common points to carry out parameter analysis and design optimization in the future research; and examine the performance of the flexible parachute system in terms of Mach number, the ratio of a capsule to a canopy diameter, and the trailing distance between the capsule and canopy. In addition, in this study it is necessary to make sure whether that the immersed boundary method can be employed to simulate the supersonic flexible parachute problems.

1.3 Thesis Outline

In this study we treat cases with a small trailing distance between the capsule and canopy, and the supersonic flow over rigid and flexible parachute models are studied numerically at supersonic speeds ranging from M=1.6 to M=2.2.

Chapter 2 presents the numerical methods used for the flow and structure calculations in this study, and the computational code validation is performed in Chapter 3, where the computation results show good agreement with experimental data. In Chapter 3, two rigid parachute models at a freestream Mach number of 2.0 are numerical simulated, where the complicated aerodynamic interferences and the unsteady flow field with pulsation phenomenon are shown and discussed in detail. Chapters 4, 5, and 6 present a way to apply the immersed boundary method to a fluid-structure interaction problem involving supersonic flexible parachute models, including two-dimensional, axisymmetric, three-dimensional models, respectively. In addition, the effect of Mach number on the flow field is examined in all the cases, as shown in Chapters 3, 4, 5, and 6. Moreover, the performance of the three-dimensional flexible parachute system depends on such factors as trailing distance, the ratio of a capsule to a canopy diameter

are investigated as shown in Chapter 6. Finally, Some general conclusions as well as the difference between rigid and flexible cases are summarized in Chapter 7.

Chapter 2

Computational Methods

2.1 Introduction

In this study, the supersonic flow over a parachute system was simulated by numerically solving compressible Navier-Stokes equations. Moreover, flexible case was treated by using the immersed boundary method together with the fluid-structure coupling scheme. In this chapter, the numerical methods for the flow and structure calculations are presented, including the fluid-structure coupling method. In addition, the validation for the Computational Fluid Dynamics (CFD) code will be carried out by comparing numerical results with experimental data in Chapter 3.

2.2 Flow Calculation

2.2.1 3D Navier-Stokes Equations

For an unsteady compressible flow, the three-dimensional dimensionless Navier-Stokes equations in the conservation form and Cartesian coordinates can be written as follows (see textbook [61, 62] for details):

$$\frac{\partial Q}{\partial t} + \frac{\partial E}{\partial x} + \frac{\partial F}{\partial y} + \frac{\partial G}{\partial z} = Re^{-1}\left(\frac{\partial E_v}{\partial x} + \frac{\partial F_v}{\partial y} + \frac{\partial G_v}{\partial z}\right) \tag{2.1}$$

where Q, E, F, G, E_v, F_v, G_v are given by

$$Q = \begin{bmatrix} \rho \\ \rho u \\ \rho v \\ \rho w \\ e \end{bmatrix}, \quad E = \begin{bmatrix} \rho u \\ \rho u^2 + p \\ \rho uv \\ \rho uw \\ (e+p)u \end{bmatrix}, \quad F = \begin{bmatrix} \rho v \\ \rho vu \\ \rho v^2 + p \\ \rho vw \\ (e+p)v \end{bmatrix}, \quad G = \begin{bmatrix} \rho w \\ \rho wu \\ \rho wv \\ \rho w^2 + p \\ (e+p)w \end{bmatrix},$$

$$E_v = \begin{bmatrix} 0 \\ \tau_{xx} \\ \tau_{xy} \\ \tau_{xz} \\ u\tau_{xx} + v\tau_{xy} + w\tau_{xz} + kT_x \end{bmatrix},$$

$$F_v = \begin{bmatrix} 0 \\ \tau_{yx} \\ \tau_{yy} \\ \tau_{yz} \\ u\tau_{yx} + v\tau_{yy} + w\tau_{yz} + kT_y \end{bmatrix},$$

$$G_v = \begin{bmatrix} 0 \\ \tau_{zx} \\ \tau_{zy} \\ \tau_{zz} \\ u\tau_{zx} + v\tau_{zy} + w\tau_{zz} + kT_z \end{bmatrix}$$

wherein Q represents the vector of conserved variables. ρ represents the density, u, v, w are the velocities in x, y, z directions, respectively. e represents the total energy per unit volume, p is the pressure. E, F and G represent the inviscid fluxes in x, y and z directions, respectively; and E_v, F_v, and G_v represent the viscous fluxes in x, y and z directions, respectively. τ_{ij} represents the viscous stress tensor, k denotes the thermal conductivity, T_i is the gradient of the temperature.

Here in a Newtonian fluid, the relationship between the viscous stress tensor and the rate of strain tensor is linear, the components of the viscous stress tensor can be written as follows (see details in Ref. [63, 64]):

$$\tau_{xy} = \tau_{yx} = \mu\left(\frac{\partial u}{\partial y} + \frac{\partial v}{\partial x}\right)$$
$$\tau_{yz} = \tau_{zy} = \mu\left(\frac{\partial v}{\partial z} + \frac{\partial w}{\partial y}\right)$$

$$\begin{aligned}
\tau_{zx} &= \tau_{xz} = \mu\left(\frac{\partial w}{\partial x} + \frac{\partial u}{\partial z}\right) \\
\tau_{xx} &= \lambda\left(\frac{\partial u}{\partial x} + \frac{\partial v}{\partial y} + \frac{\partial w}{\partial z}\right) + 2\mu\frac{\partial u}{\partial x} \\
\tau_{yy} &= \lambda\left(\frac{\partial u}{\partial x} + \frac{\partial v}{\partial y} + \frac{\partial w}{\partial z}\right) + 2\mu\frac{\partial v}{\partial y} \\
\tau_{zz} &= \lambda\left(\frac{\partial u}{\partial x} + \frac{\partial v}{\partial y} + \frac{\partial w}{\partial z}\right) + 2\mu\frac{\partial w}{\partial z}
\end{aligned} \tag{2.2}$$

in which λ is the second viscosity coefficient, μ is the dynamic viscosity coefficient. Under the Stokes's hypothesis [65], then we can obtain,

$$\lambda + \frac{2}{3}\mu = 0 \tag{2.3}$$

Furthermore, the dynamic viscosity, μ, was defined by Sutherland's law [66, 67], the relation with the absolute temperature, T, can be written as follows,

$$\frac{\mu}{\mu_\infty} = \frac{T_\infty + S_1}{T + S_1}\left(\frac{T}{T_\infty}\right)^{\frac{3}{2}} \tag{2.4}$$

where S_1 refers to 110.4K, and T_∞ refers to 273K in this study. Other relations in the dimensionless form are as follows,
the total energy:

$$e = \frac{p}{\rho(\gamma - 1)} + \frac{1}{2}\left(u^2 + v^2 + w^2\right) \tag{2.5}$$

the thermal conductivity:

$$k = \frac{\mu}{(\gamma - 1)M_\infty^2 Pr} \tag{2.6}$$

where the ratio of the specific heats, γ refers to 1.4; the Prandtl number Pr is 0.72 for laminar flow [68] in this study.

2.2.2 Navier-Stokes Equations in Generalized Coordinate System

In order to perform the calculation using arbitrary body fitted grid, it is necessary to transform the Navier-Stokes equations in Cartesian coordinate system (x,y,z) to the generalized coordinate system (ξ, η, ζ). The basic principles of this transformation can

refer to Ref. [69] and Ref.[70]. The relationship between the two coordinate systems is written as follows.

$$x = x(\xi, \eta, \zeta), \qquad y = y(\xi, \eta, \zeta), \qquad z = z(\xi, \eta, \zeta) \tag{2.7}$$

A matrix form of Eq. 2.7 can be written as follows:

$$\begin{bmatrix} dx \\ dy \\ dz \end{bmatrix} = \begin{bmatrix} x_\xi & x_\eta & x_\zeta \\ y_\xi & y_\eta & y_\zeta \\ z_\xi & z_\eta & z_\zeta \end{bmatrix} \begin{bmatrix} d\xi \\ d\eta \\ d\zeta \end{bmatrix} \tag{2.8}$$

In the same manner, we can get the inverse transformation as Eq. 2.9.

$$\begin{bmatrix} d\xi \\ d\eta \\ d\zeta \end{bmatrix} = \begin{bmatrix} \xi_x & \xi_y & \xi_z \\ \eta_x & \eta_y & \eta_z \\ \zeta_x & \zeta_y & \zeta_z \end{bmatrix} \begin{bmatrix} dx \\ dy \\ dz \end{bmatrix} \tag{2.9}$$

From the relations between Eqs. 2.8 and 2.9, we can obtain Eq. 2.10

$$\begin{aligned} \begin{bmatrix} \xi_x & \xi_y & \xi_z \\ \eta_x & \eta_y & \eta_z \\ \zeta_x & \zeta_y & \zeta_z \end{bmatrix} &= \begin{bmatrix} x_\xi & x_\eta & x_\zeta \\ y_\xi & y_\eta & y_\zeta \\ z_\xi & z_\eta & z_\zeta \end{bmatrix}^{-1} \\ &= J \begin{bmatrix} y_\eta z_\zeta - y_\zeta z_\eta & z_\eta x_\zeta - z_\zeta x_\eta & x_\eta y_\zeta - x_\zeta y_\eta \\ y_\zeta z_\xi - y_\xi z_\zeta & z_\zeta x_\xi - z_\xi x_\zeta & x_\zeta y_\xi - x_\xi y_\zeta \\ y_\xi z_\eta - y_\eta z_\xi & z_\xi x_\eta - z_\eta x_\xi & x_\xi y_\eta - x_\eta y_\xi \end{bmatrix} \end{aligned} \tag{2.10}$$

So

$$\begin{array}{lll} \xi_x = J(y_\eta z_\zeta - y_\zeta z_\eta) & \xi_y = J(z_\eta x_\zeta - z_\zeta x_\eta) & \xi_z = J(x_\eta y_\zeta - x_\zeta y_\eta) \\ \eta_x = J(y_\zeta z_\xi - y_\xi z_\zeta) & \eta_y = J(z_\zeta x_\xi - z_\xi x_\zeta) & \eta_z = J(x_\zeta y_\xi - x_\xi y_\zeta) \\ \zeta_x = J(y_\xi z_\eta - y_\eta z_\xi) & \zeta_y = J(z_\xi x_\eta - z_\eta x_\xi) & \zeta_z = J(x_\xi y_\eta - x_\eta y_\xi) \end{array} \tag{2.11}$$

where "J" is the transformation Jacobian, it can be obtained from Eq. 2.10 (details of the derivation can refer to [61]).

$$\frac{1}{J} = x_\xi(y_\eta z_\zeta - y_\zeta z_\eta) + x_\eta(y_\zeta z_\xi - y_\xi z_\zeta) + x_\zeta(y_\xi z_\eta - y_\eta z_\xi) \tag{2.12}$$

Now, after using the chain rule, the partial derivative of flux vectors in Eq. 2.1 will become:

$$\frac{\partial}{\partial x} = \xi_x \frac{\partial E}{\partial \xi} + \eta_x \frac{\partial E}{\partial \eta} + \zeta_x \frac{\partial E}{\partial \zeta} \tag{2.13}$$

$$\frac{\partial}{\partial y} = \xi_y \frac{\partial F}{\partial \xi} + \eta_y \frac{\partial F}{\partial \eta} + \zeta_y \frac{\partial F}{\partial \zeta} \tag{2.14}$$

$$\frac{\partial}{\partial z} = \xi_z \frac{\partial G}{\partial \xi} + \eta_z \frac{\partial G}{\partial \eta} + \zeta_z \frac{\partial G}{\partial \zeta} \tag{2.15}$$

Then take the x direction for example, the following relation can be obtained as follows (refer to Ref. [61] and Ref.[71]).

$$\begin{aligned}\frac{\partial E}{\partial x} &= \xi_x\frac{\partial E}{\partial \xi}+\eta_x\frac{\partial E}{\partial \eta}+\zeta_x\frac{\partial E}{\partial \zeta} \\ &= J\left[\frac{\partial}{\partial \xi}\left(\frac{\xi_x E}{J}\right)+\frac{\partial}{\partial \eta}\left(\frac{\eta_x E}{J}\right)+\frac{\partial}{\partial \zeta}\left(\frac{\zeta_x E}{J}\right)\right] \\ &= J\left[\frac{\partial}{\partial \xi}(J^{-1}(\xi_x E))+\frac{\partial}{\partial \eta}(J^{-1}(\eta_x E))+\frac{\partial}{\partial \zeta}(J^{-1}(\zeta_x E))\right]\end{aligned} \tag{2.16}$$

Using the same manner, the Navier-Stokes equations in generalized coordinate system can be written as follows

$$\frac{\partial \hat{Q}}{\partial t}+\frac{\partial \hat{E}}{\partial \xi}+\frac{\partial \hat{F}}{\partial \eta}+\frac{\partial \hat{G}}{\partial \zeta}=Re^{-1}\left(\frac{\partial \hat{E}_v}{\partial \xi}+\frac{\partial \hat{F}_v}{\partial \eta}+\frac{\partial \hat{G}_v}{\partial \zeta}\right) \tag{2.17}$$

where $\hat{Q},\hat{E},\hat{G},\hat{E}_v,\hat{F}_v,\hat{G}_v$ are given by

$$\hat{Q}=J^{-1}\begin{bmatrix}\rho\\ \rho u\\ \rho v\\ \rho w\\ e\end{bmatrix},\quad \hat{E}=J^{-1}\begin{bmatrix}\rho U\\ \rho uU+\xi_x p\\ \rho vU+\xi_y p\\ \rho wU+\xi_z p\\ (e+p)U\end{bmatrix},\quad \hat{F}=J^{-1}\begin{bmatrix}\rho V\\ \rho uV+\eta_x p\\ \rho vV++\eta_y p\\ \rho wV+\eta_z p\\ (e+p)V\end{bmatrix},$$

$$\hat{G}=J^{-1}\begin{bmatrix}\rho W\\ \rho uW+\zeta_x p\\ \rho vW+\zeta_y p\\ \rho wW+\zeta_z p\\ (e+p)W\end{bmatrix},\qquad \hat{E}_v=J^{-1}\begin{bmatrix}0\\ \xi_x\tau_{xx}+\xi_y\tau_{xy}+\xi_z\tau_{xz}\\ \xi_x\tau_{yx}+\xi_y\tau_{yy}+\xi_z\tau_{yz}\\ \xi_x\tau_{zx}+\xi_y\tau_{zy}+\xi_z\tau_{zz}\\ \xi_x\beta_x+\xi_y\beta_y+\xi_z\beta_z\end{bmatrix},$$

$$\hat{F}_v=J^{-1}\begin{bmatrix}0\\ \eta_x\tau_{xx}+\eta_y\tau_{xy}+\eta_z\tau_{xz}\\ \eta_x\tau_{yx}+\eta_y\tau_{yy}+\eta_z\tau_{yz}\\ \eta_x\tau_{zx}+\eta_y\tau_{zy}+\eta_z\tau_{zz}\\ \eta_x\beta_x+\eta_y\beta_y+\eta_z\beta_z\end{bmatrix},\hat{G}_v=J^{-1}\begin{bmatrix}0\\ \zeta_x\tau_{xx}+\zeta_y\tau_{xy}+\zeta_z\tau_{xz}\\ \zeta_x\tau_{yx}+\zeta_y\tau_{yy}+\zeta_z\tau_{yz}\\ \zeta_x\tau_{zx}+\zeta_y\tau_{zy}+\zeta_z\tau_{zz}\\ \zeta_x\beta_x+\zeta_y\beta_y+\zeta_z\beta_z\end{bmatrix}$$

herein U, V, and W are the contravariant velocities in the ξ,η,and ζ directions as defined in Eq. 2.18. In addition, β_x,β_y,β_z are given by Eq. 2.19, and the components of the viscous stress tensor can refer to Eq. 2.2.

$$\begin{aligned}U&=\xi_x u+\xi_y v+\xi_z w\\ V&=\eta_x u+\eta_y v+\eta_z w\\ W&=\zeta_x u+\zeta_y v+\zeta_z w\end{aligned} \tag{2.18}$$

$$\begin{aligned}\beta_x&=\tau_{xx}u+\tau_{xy}v+\tau_{xz}w+kT_x\\ \beta_y&=\tau_{yx}u+\tau_{yy}v+\tau_{yz}w+kT_y\\ \beta_z&=\tau_{zx}u+\tau_{zy}v+\tau_{zz}w+kT_z\end{aligned} \tag{2.19}$$

2.2.3 Axisymmetric Navier-Stokes Equations

In this study, the two-dimensional axisymmetric Navier-Stokes equations are applied to model the flexible parachute problem, because the parachute model is assumed here to be axisymmetric around the longitudinal axis. In cylindrical coordinates, the axisymmetric form of the Navier-Stokes equations in conservation forms are as follows (refer to Ref. [72] and Ref.[73])

$$\frac{\partial Q}{\partial t} + \frac{\partial E}{\partial x} + \frac{\partial F}{\partial y} = \frac{\partial E_v}{\partial x} + \frac{\partial F_v}{\partial y} + Q^* \tag{2.20}$$

where x, y are the axial and radial coordinates, respectively. Q represents the vector of the conservative variables. E, F represent the inviscid fluxes in the axial and radial directions, respectively, and E_v, F_v represent viscous fluxes in the axial and radial direction, respectively. Q^* represents the source term. The Q, E, F, E_v, F_v, Q^* are given by:

$$Q = \begin{bmatrix} \rho \\ \rho u \\ \rho v \\ \rho e \end{bmatrix}, \quad E = \begin{bmatrix} \rho u \\ \rho u^2 + p \\ \rho uv \\ (\rho e + p)u \end{bmatrix}, \quad F = \begin{bmatrix} \rho v \\ \rho vu \\ \rho v^2 + p \\ (\rho e + p)v \end{bmatrix},$$

$$E_v = \begin{bmatrix} 0 \\ \tau_{xx} \\ \tau_{xy} \\ u\tau_{xx} + v\tau_{xy} + kT_x \end{bmatrix},$$

$$F_v = \begin{bmatrix} 0 \\ \tau_{yx} \\ \tau_{yy} \\ u\tau_{yx} + v\tau_{yy} + kT_y \end{bmatrix}, \quad Q^* = \begin{bmatrix} 0 \\ 0 \\ -\frac{\tau_{\theta\theta}}{r} \\ 0 \end{bmatrix}$$

where u, v is the velocity components in the axial and radial direction, respectively. e is the total energy. θ refers to the azimuthal coordinate.

In addition, the components of the viscous stress tensor are written as

$$\tau_{xx} = -\frac{2\mu}{3}\nabla\cdot V + 2\mu\frac{\partial u}{\partial x} \tag{2.21}$$

$$\tau_{yy} = -\frac{2\mu}{3}\nabla\cdot V + 2\mu\frac{\partial u}{\partial y} \tag{2.22}$$

$$\tau_{\theta\theta} = -\frac{2\mu}{3}\nabla\cdot V + 2\mu\frac{v}{y} \tag{2.23}$$

$$\tau_{xy} = \tau_{yx} = \mu\left(\frac{\partial u}{\partial y} + \frac{\partial v}{\partial x}\right) \tag{2.24}$$

where

$$\nabla\cdot V = \frac{\partial u}{\partial x} + \frac{\partial v}{\partial y} + \frac{v}{y} \tag{2.25}$$

2.2.4 Evaluation of Inviscid Flux

In this research, Simple High-resolution Upwind scheme (SHUS) [74] is widely used for evaluating the inviscid fluxes in the numerical simulation of supersonic flow over two-dimensional, three-dimensional parachute systems. The SHUS is one of AUSM type schemes [75], which are very simple, robust and accurate for modeling the shock wave and boundary layer, but has some weakness at shock front [74]. However, SHUS scheme can be more robust and have high resolution at the simulation of the such complex flows, exhibits strong shock wave and aerodynamic interaction [76].

Simple Low-dissipation AUSM (SLAU) [77] is applied to evaluate the numerical flux for the simulation of the axisymmetric parachute model. SLAU scheme is also from the AUSM type schemes [75], and also has the advantage of the robust against the shock instability and oscillation [77]. In addition, the accuracy of these schemes is improved by using the MUSCL scheme [78, 79] with the Van Albada flux limiter [80].

2.2.4.1 AUSM Scheme

The AUSM scheme is used to estimate the inviscid flux at the cell interface, in which the numerical flux is split into two parts: the convective term and the pressure term. This scheme can be written in generalized formulation as follows (more details see [74, 76, 81]),

$$E_{\frac{1}{2}} = \frac{m+|m|}{2}\psi_+ + \frac{m-|m|}{2}\psi_- + \hat{p}N \tag{2.26}$$

$$\psi = \begin{bmatrix} 1 \\ u \\ v \\ w \\ H \end{bmatrix}, \qquad N = \begin{bmatrix} 0 \\ n_x \\ n_y \\ n_z \\ 0 \end{bmatrix}, \tag{2.27}$$

$$m = \rho V_n, \quad V_n = n_x u + n_y v + n_z w \tag{2.28}$$

where H is total enthalpy, m is the mass flux. n_x, n_y, n_z represent the unit normal vector to the cell-interface in x, y, z directions, respectively. In addition, $\hat{p}$ is defined based on Mach number of left (+) and right (-) value, as shown in Eq. 2.29.

$$\hat{p} = \beta^+ p_L + \beta^- p_R + p^* \tag{2.29}$$

$$\beta^\pm = \begin{cases} \frac{1}{4}\left(2 \mp M_\pm\right)\left(M_\pm \pm 1\right)^2 & if\ |M_\pm| \leq 1 \\ \\ \frac{1}{2}\frac{(M_\pm |M|)}{M} & otherwise \end{cases} \tag{2.30}$$

where the subscript L and R mean physical value of left and right side of the interface, p^* is a pressure correction term, the details about this term can be found in Ref. [74].

2.2.4.2 SHUS Scheme

In SHUS scheme, the mass flux m is different from the other AUSM-family schemes, and comes from Roe scheme [74], its more details can refer to Ref. [74], Ref. [81] and Ref. [76]. it is given by

$$\begin{aligned} m &= \frac{1}{2}\{(\rho V_n)_+ + (\rho V_n)_- - \left|\bar{V_n}\right| \Delta\rho \\ &- \frac{\left|\bar{M}+1\right| - \left|\bar{M}-1\right|}{2}\bar{\rho}\Delta V_n \\ &- \frac{\left|\bar{M}+1\right| - \left|\bar{M}-1\right| - 2\left|\bar{M}\right|}{2}\frac{\Delta p}{\bar{c}}\} \end{aligned} \tag{2.31}$$

$$\Delta\rho = \rho_R - \rho_L, \quad \Delta p = p_R - p_L, \quad \Delta V_n = V_{nR} - V_{nL},$$

$$\bar{\rho} = \frac{\rho_L + \rho_R}{2}, \quad \bar{p} = \frac{p_L + p_R}{2}, \quad \bar{V_n} = \frac{V_{nL} + V_{nR}}{2}, \quad \bar{M} = \frac{\bar{V_n}}{\bar{c}}$$

The pressure flux is

$$\hat{p} = \beta^+ p_L + \beta^- p_R \tag{2.32}$$

where $\beta^\pm$ can refer to Eq. 2.30.

2.2.4.3 SLAU Scheme

Since the SLAU scheme [77] is used in axisymmetric case, Eq. 2.27 will be rewritten as follow,

$$\psi = \begin{bmatrix} 1 \\ u \\ v \\ H \end{bmatrix}, \qquad N = \begin{bmatrix} 0 \\ n_x \\ n_y \\ 0 \end{bmatrix}, \tag{2.33}$$

Moreover, the mass flux of SLAU is given by

$$m = \frac{1}{2}\{\rho_L(V_{nL} + |\bar{V_n}|^+) + \rho_R(V_{nR} - |\bar{V_n}|^-) - \frac{\chi}{\bar{c}}\Delta p\} \tag{2.34}$$

where

$$|\bar{V_n}| = \frac{\rho_L |V_{nL}| + \rho_R |V_{nR}|}{\rho_L + \rho_R}, \tag{2.35}$$

$$|\bar{V_n}|^+ = (1-g)|\bar{V_n}| + g|V_{nL}|, \tag{2.36}$$

$$|\bar{V_n}|^- = (1-g)|\bar{V_n}| + g|V_{nR}|, \tag{2.37}$$

$$g = -max[min(M_L, 0), -1] \cdot min[max(M_R, 0), 1] \in [0, 1] \tag{2.38}$$

The pressure flux is

$$\hat{p} = \frac{p_L + p_R}{2} + \frac{\beta^+ - \beta^-}{2}(p_L - p_R) + (1-\chi)(\beta^+ + \beta^- - 1)\frac{p_L + p_R}{2} \tag{2.39}$$

$$\chi = (1 - \hat{M})^2 \tag{2.40}$$

$$\hat{M} = min[1.0, \frac{1}{c_{\frac{1}{2}}}(\frac{{u_L}^2 + {v_L}^2 + {u_R}^2 + {v_R}^2}{2})^{\frac{1}{2}}] \tag{2.41}$$

$$M = \frac{V_n}{c_{\frac{1}{2}}} = \frac{un_x + vn_y}{c_{\frac{1}{2}}} \tag{2.42}$$

Here $\beta^{\pm}$ can refer to Eq. 2.30. The interface sound of speed $c_{\frac{1}{2}}$ is defined as follow:

$$c_{\frac{1}{2}} = min(c_L, c_R) \tag{2.43}$$

$$c_{L/R} = \frac{\hat{c}^2}{max(\hat{c}, \left|\bar{V}_n\right|^{\pm})} \tag{2.44}$$

$$\hat{c}^2 = \frac{2(\gamma - 1)H}{\gamma + 1} \tag{2.45}$$

More details about SLAU scheme can read Ref. [77] and Ref. [81].

2.2.5 Time Advancement

In this study, the 3rd-order total variation diminishing (TVD) Runge-Kutta scheme [82] is widely used to obtain time accurate results in unsteady calculations. In addition, the classical explicit 2nd order Runge-Kutta method (eg. [61]) is also applied for the axisymmetric flexible case and the canopy model calculation. The Runge-Kutta scheme with the TVD property, is a very simple and effective approach to solve the flow field with discontinuities, such as shock waves [83, 84].The governing equations of fluid flow can be reduced to

$$U_t = L(U) \tag{2.46}$$

The time advancement for Eq. 2.46 can be carried out by using the 3rd TVD Runge-Kutta scheme proposed by Shu and Osher [82], which can be written as follows,

$$U^{(1)} = U^n + \Delta t L(U^n) \tag{2.47}$$

$$U^{(2)} = \frac{3}{4}U^n + \frac{1}{4}U^{(1)} + \frac{1}{4}\Delta t L(U^{(1)}) \tag{2.48}$$

$$U^{n+1} = \frac{1}{3}U^n + \frac{2}{3}U^{(2)} + \frac{2}{3}\Delta t L(U^{(2)}) \tag{2.49}$$

More details about this scheme can be found in Ref. [82],Ref. [83],Ref. [84].

2.2.6 Boundary Conditions

At the inflow boundary, all conservative variables are decided by the freestream values. At the outer boundary, the conservative variables are solved from the solution inside the computational domain.

For the solid body, the no-slip and adiabatic conditions [69] are used to treat the boundary surfaces.

$$u = v = w = 0$$

$$(\frac{\partial T}{\partial n})_{wall} = 0$$

In addition, due to the axisymmetric configuration for the present problem, it is necessary to consider the periodic and symmetry boundary conditions, here the average conditions are used to treat them.

In the flexible cases, the immersed boundary method (IBM) [85, 86, 87] is applied to deal with the moving boundary of the flexible canopy. It will be introduced in the section 2.4 .

2.3 Structure Calculation

In this study the mass-spring-damper (MSD) model [88] was applied to solve the structural dynamics of the flexible canopy, which has been used to simulate many kinds of fluid-flexible body interaction problems such as the parachute system including the 2D and 3D models [88, 90] , fluid-membrane interaction [89]. This model treats a canopy as an assembly of mass nodes attached to springs and dampers.

The governing equations of mass-spring-damper (MSD) model are computed based on Newton's second law at each control node of canopy [88]. The force analysis of a mass node of the canopy surface are shown from Fig. 2.1 to Fig. 2.3. As we can see that these forces include the tangential spring and damper forces, the pressure difference between the inner and outer surface, the normal damper force, and the gravity force. In addition, from Fig. 2.2, it is found that the mass node of the edge canopy has a different force from the interior one, the tension of suspension line needs to be considered. The equation of motion for the canopy nodes [90] can be expressed as follows,

$$\begin{aligned} \frac{d^2 x_{i,j}}{dt^2} &= \frac{1}{m}\{\sum_{n=1}^{N}(k_m \Delta l_\kappa + c_m \frac{d(\Delta l_\kappa)}{dt})e_\kappa \\ &- c_n(V_{i,j} \cdot n_{i,j})n_{i,j} + \Delta P_{i,j} + G_{i,j} + T_{i,j}\} \end{aligned} \tag{2.50}$$

where m is mass of a canopy node, k_m, c_m, c_n represent the spring constant, damping coefficient in tangential direction, damping coefficient in normal direction, respectively.

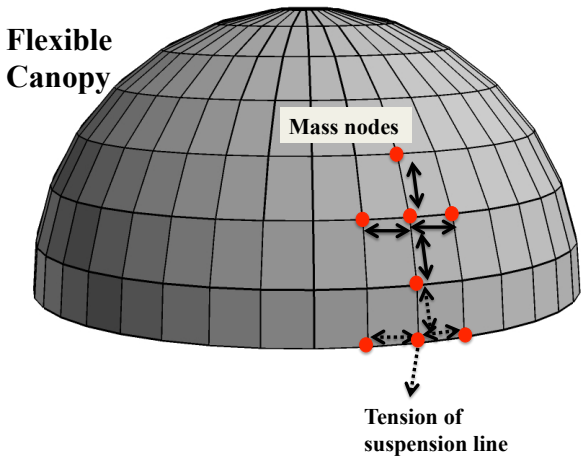

Figure 2.1: Overview of the tangential force acting on the mass nodes of flexible canopy surface, the red point is a mass node of canopy surface

Δl_k is the deformation value of the spring. e_κ represents the unit vector between two neighboring nodes. $V_{i,j}$ represents the velocity of a mass node, $n_{i,j}$ represents the normal vector to the canopy surface. $\Delta P_{i,j}, G_{i,j}, T_{i,j}$ represent the pressure difference between the inner and outer canopy surface, gravity force, the tension of suspension line respectively. It should be pointed out that N=4 for a typical interior node; N=3 for a mass node at the edge part of canopy, and the effect of tension of the suspension line is also considered.

In addition, in the canopy model calculation, the explicit 2nd-order Runge-Kutta scheme is used to obtain the time-variations of the canopy shape.

2.4 Fluid-Structure Coupling Method

Among several ways of modeling the fluid-structure interaction, the Arbitrary Lagrangian Eulerian (ALE) method [91] has been commonly used for FSI problems. Provided that the rotation, translation and/or deformation of a structure lie within certain limits, this method is very effective. However, when these limits change with time, ALE elements become ill-shaped, so that in this case the ALE method alone blows up [92].

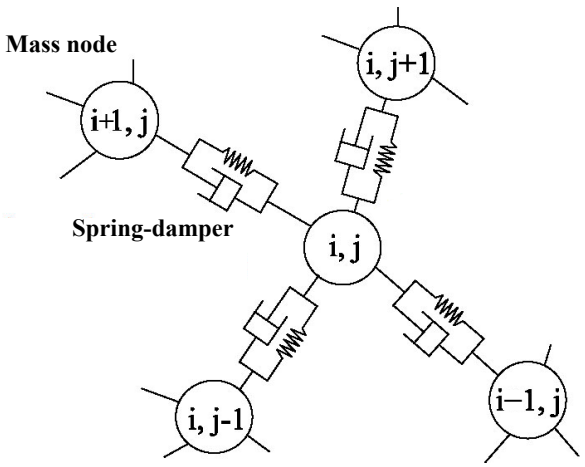

(a) a typical interior mass node [90]

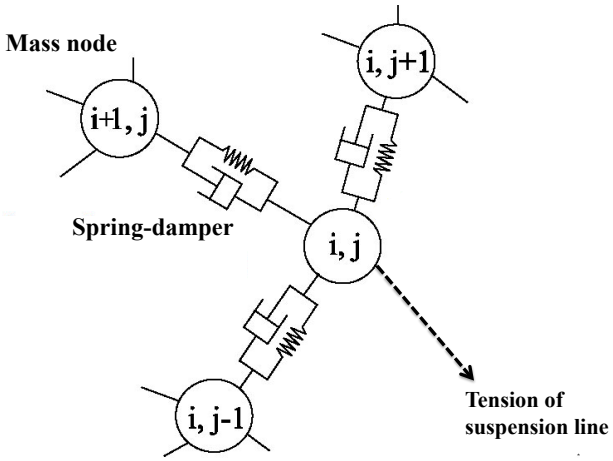

(b) a special MSD model at the edge of canopy

Figure 2.2: MSD model of the canopy from Fig. 2.1

In addition, numerical simulation of the fluid-structure interaction problems involving the flexible parachute models has attracted great attention for many years, some successful methods such as the DST/SST method [93], immersed boundary method [94, 95], front tracking method [96] were applied to solve the parachute model at low speeds, however, there are relatively few numerical methods on solving the supersonic parachute

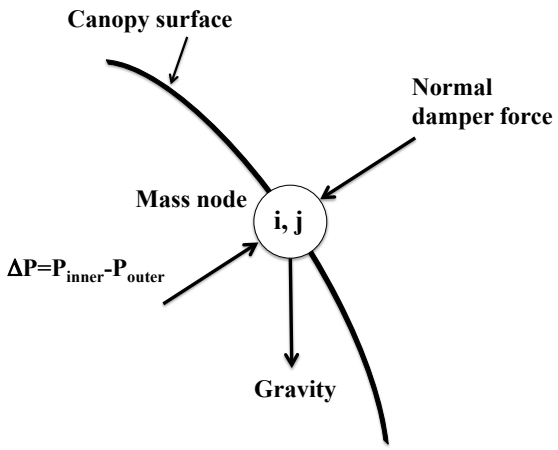

Figure 2.3: The normal force acting on the mass nodes of flexible canopy surface

problem. Here in the present study, we present a way to apply a simple immersed boundary method [85] to a fluid structure interaction problem involving supersonic flexible parachute models. This method has been employed for the numerical simulation of 2D and 3D flexible parachute systems at lower Mach number [85, 90], where the history of the canopy inflation in simulation was qualitative agreement with the experiment data; and for the 2D and axisymmetric flexible parachute system at supersonic conditions [86].

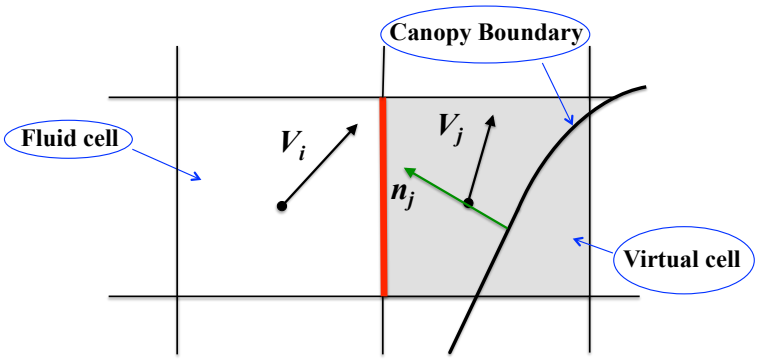

Figure 2.4: Velocity vectors in fluid and virtual cell [4]

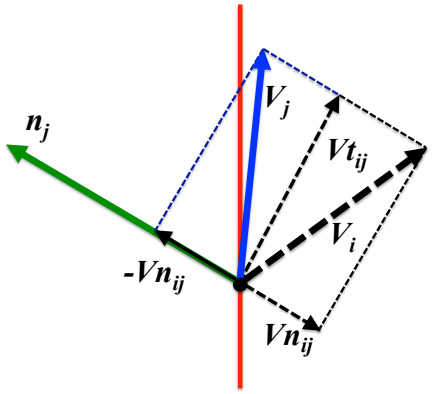

Figure 2.5: Relationship between the velocities of fluid and virtual cell [4]

2.4.1 Immersed Boundary Method

The immersed boundary method [85, 90] was applied to compute the moving boundary of a flexible canopy. The boundary conditions of the canopy surface were treated using the approach presented by Ochi et al. [4]. It can approximately give the velocity vectors of the virtual cells on the condition that this boundary is fixed. This method has been modified so as to deal with the moving boundary conditions of the flexible canopy surface. The velocity vectors in the virtual cells can obtain from the relation between fluid and virtual cells(see Figs. 2.4 and Fig. 2.5),which can be written as follow (see details in Ref. [4, 90]).

$$V_j = V_i - 2(V_i \cdot n_j)n_j + V_w \tag{2.51}$$

where V_i, V_j, V_w refer to the velocity vector in the fluid cell (i), virtual cell (j), canopy velocity , respectively; and n_j a unit vector normal to the canopy surface (see Figs. 2.4 and Fig. 2.5).

2.4.2 Fluid-Structure Coupling Scheme

In order to solve the coupling problem, it is first separated into the fluid and structure parts. Fig. 2.6 shows the fluid-structure coupling method used in the present study. The pressure distribution on the canopy surface as the fluid force is obtained from the

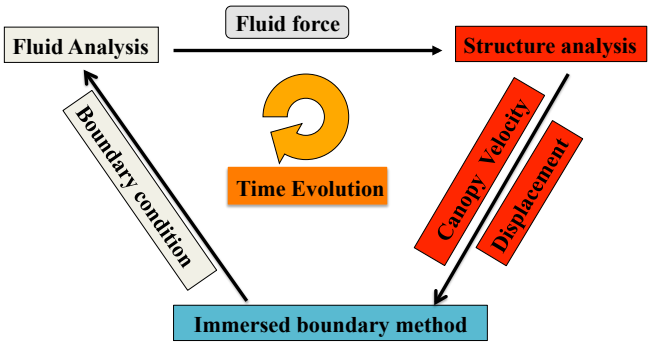

Figure 2.6: The fluid-structure coupling method used in this study [90]

result of flow simulation, which is used to calculate the displacement and velocity of each canopy node. Then, those data are provided to calculation by the immersed boundary method. The explicit 2nd-order Runge-Kutta scheme is used to obtain time-variations in the canopy model calculation.

The method to solve the fluid and structure equations can be classified into weak and strong coupling schemes; in the former the governing equations are solved separately in a time domain, while in the latter they are solved concurrently. It is known that the strong coupling method is more stable and robust, while the weak coupling method is more flexible [98]. In this study in order to solve the fluid and structure equations simultaneously, the method of strong coupling is employed for the two-dimensional case, while the method of weak coupling is employed to solve the axisymmetric case and three-dimensional case.

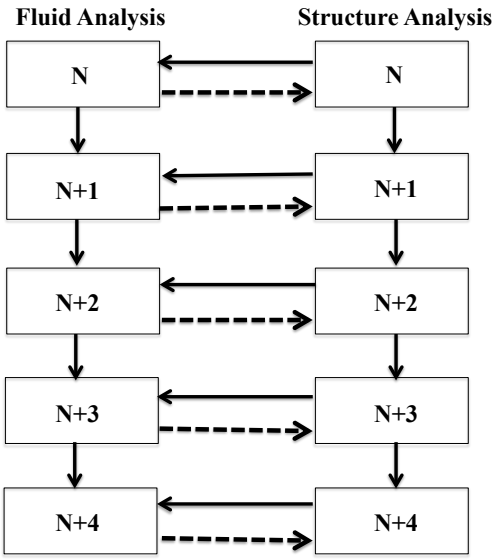

(a) The scheme of strong coupling [97]

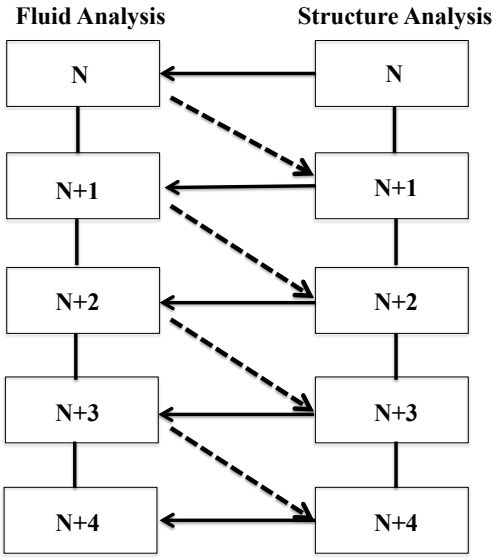

(b) The scheme of weak coupling

Figure 2.7: The fluid-structure coupling scheme

Chapter 3

Three-Dimensional Flow Around Axisymmetric Rigid Parachute

3.1 Introduction

Here in this study a rather small trailing distance is considered, the flow field around a parachute model shows complicated wake/shock and shock/shock interactions. In order to fully understand the flow field and investigate the effects of such wake/shock and shock/shock interactions on the flow instability, numerical simulation was carried out for three-dimensional rigid models at a freestream Mach number of 2.0. The parachute system employed here consists of a capsule and a canopy. Two models were considered: Model A and Model B. The computational results obtained for model A will be validated by comparing with experimental data measured at the ISAS/JAXA supersonic tunnel.

3.2 Rigid Parachute Models

The parachute system employed here consists of a capsule and a canopy. For comparing with experiment, a rigid parachute canopy is considered, and the suspension lines are not taken into account. Two models were employed: model A and model B, which are shown in Fig. 3.1. In model A the capsule and canopy are connected by a rod, all of which is supported at the top of the canopy by a thicker rod to the wind tunnel model support system; this configuration is the same as the model used in experiment. On the other hand, model B is basically close to model A except for having no rods. It should be noted that the capsule takes a conical form with a half-cone angle of 20 deg

and a front diameter of 0.20D (see Fig. 3.1), and X/d refers to the trailing distance between the capsule and canopy.

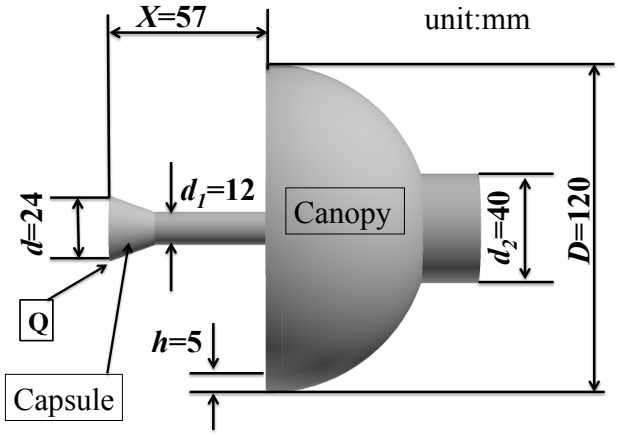

(a) Model A

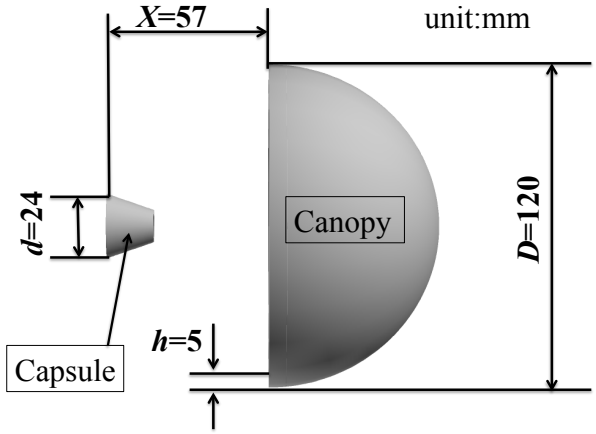

(b) Model B

Figure 3.1: Models used in the present computation

3.3 The Method of Simulation

3.3.1 Computational Conditions

The computational conditions for the freestream in computation are the same as those in experiment, which are listed in Table 3.1.

Table 3.1: Freestream conditions employed in the present study

M_∞	Re	P_0	P_∞	T_0
2.0	2.04×10^7	166kPa	21kPa	298K

3.3.2 Numerical Method

The three-dimensional compressible Navier-Stokes equations were solved to simulate the supersonic flow field around parachute models, the calculations were performed using a parallel in-house structured single-block code. To evaluate the inviscid fluxes, the Simple High-resolution Upwind scheme (SHUS) [74] was adopted; the accuracy of this scheme is improved by using the 3rd MUSCL scheme [78, 79] with the Van Albada flux limiter [80]. On the other hand, the viscous terms were calculated by the usual 2nd order central differencing scheme. The coefficient of viscosity was computed according to Sutherland's law [66, 67]. The numerical code is featured by the 3rd total variation diminishing Runge-Kutta scheme [82] to obtain time accurate results in unsteady calculations.

We do not use any turbulence models in the present study, because till now most of the algebraic turbulence models were quite unreliable for separation flows [99]. In addition, in terms of initial conditions, each variable initially takes its freestream value; in terms of boundary conditions, non-slip and adiabatic conditions were imposed at body surfaces.

3.3.3 Grid Generation and Grid Convergence

Owing to the axisymmetric configuration in the present problem, the single block structured grid was created by a meridional plane. Figure 3.2 shows the 3D view of these grids.

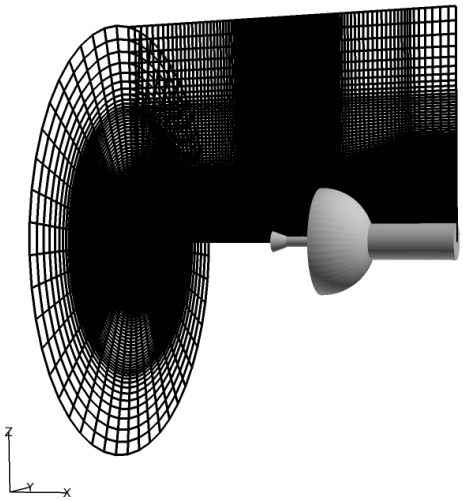

(a) Model A

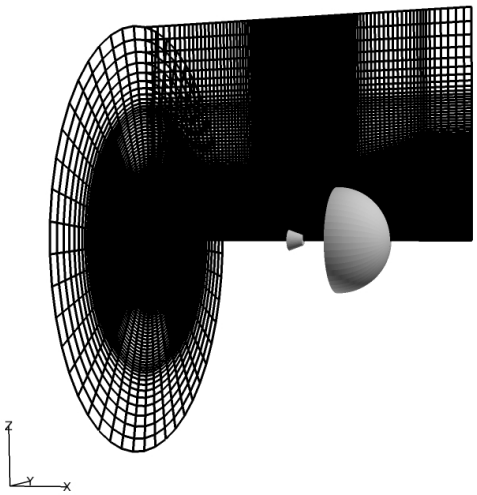

(b) Model B

Figure 3.2: Grids for parachute models

Three grids with different numbers of points listed in Table 3.2 were employed to examine the grid dependence. The pressure histories at freestream Mach 2.0 for point Q at the edge of capsule (see Fig. 3.1) were shown in Fig. 3.3. In this figure, the non-dimensional time is defined as $t_1 = t*V_\infty/D$ [100], t_1 is the non-dimensional time in this

study. By and large, the pressure time histories are almost identical in terms of both pressure amplitude and time period for the three grids. It is obvious that the resolution of the coarse grid is not enough to capture the appropriate unsteady flow. The pressure results of the medium and fine grids agree reasonably, providing comparable values in terms of pressure amplitude and time period. Therefore, henceforth, results by the medium grid will be shown in this study.

Table 3.2: Grid used for grid convergence

Type of grid	Grid number
Coarse	542, 640
Medium	3, 296, 720
Fine	5, 897, 028

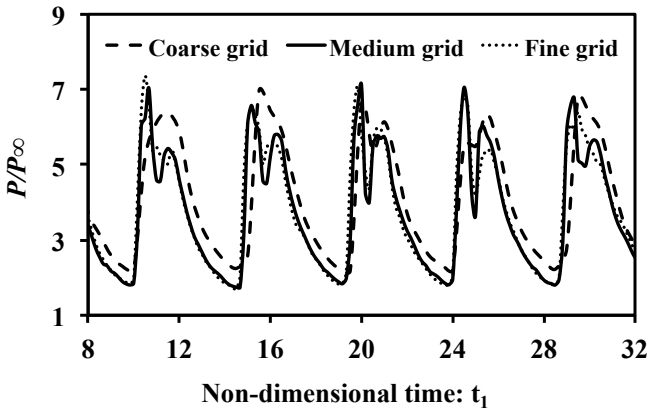

Figure 3.3: Pressure change due to grid

3.3.4 The Pressure Sensor in the Experiment

The pressure sensor used in this experiment is made by Kyowa Electronic Instruments Co., Ltd., its type is PA-2KB, which can precisely measure pressure fluctuations ranging from absolute zero (vacuum pressure) to 0.2MPa$_{abs}$, and exclusively designed for airborne measuring on supersonic vehicles. [5] It should be noted that its measurement accuracy is ±0.2 kPa [5], and the main specifications of this pressure sensor are shown in Table 3.3, and more details of the pressure sensor can refer to [5].

Table 3.3: The specification of pressure sensor used in this study [5]

Model	PA-2KB
Rated capacity	$200\text{kPa}_{\text{abs}}(2.039\text{kgf/cm}^2{}_{\text{abs}})$
Natural frequency (approx.)	5kHz
Non-linearity	±0.1%RO
Hysteresis	±0.1%RO
Rated output	$2\text{mV/V}(4000 \times 10^{-6}\text{strain})$ or higher

3.3.5 Validation of the Numerical Method

In both the experimental and CFD the shock wave envelope histories exhibit cycle-to-cycle variations, the oscillation frequency of the flow can be described by Strouhal number [101], which was adopted to make a quantitative comparison (see Table 3.4). The Strouhal number in simulation is close to that of the experiment.

In addition, as the frequency of the pressure sensor used in the experiment was rather low (see Table 3.3), it could not capture unsteadiness of the pressure. Then, as shown in Fig. 3.5, a dotted line was drawn for a reference value based on the experimental data, which seems to correspond to the average value of unsteady pressure at point A on the inner surface of the canopy (see Fig. 3.4). It can be seen from this figure that the calculated pressure data (at point A) oscillates around this line.

Table 3.4: Comparison of Strouhal numbers

Strouhal number	Experiment	CFD
$\frac{D}{T \times V_\infty}$	0.2117	0.2139

The four time locations of the CFD results (see A,B,C,D in Fig. 3.7) are defined on the pressure trace of point Q in Fig. 3.6. The four representative instantaneous flow fields in CFD in the case of model A are shown in Fig. 3.7 at a freestream Mach number of 2.0 along with the corresponding shadowgraph pictures in experiment. Comparing these left and right figures in Fig. 3.7, we can see that they are in reasonable agreement.

Averaged pressure distributions on the inner surface of the canopy and the front surface of the capsule are plotted in Fig. 3.8, along with the experimental data, where r

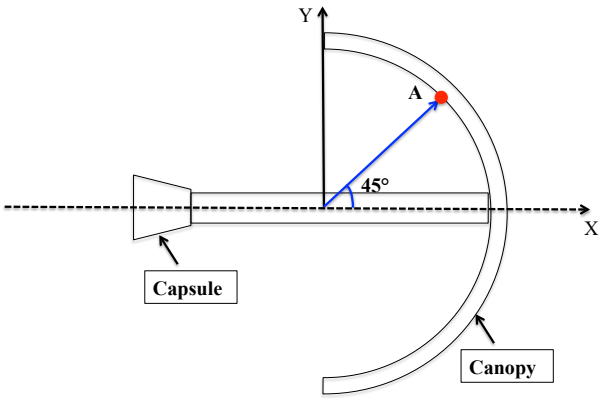

Figure 3.4: The location of point A inside the canopy

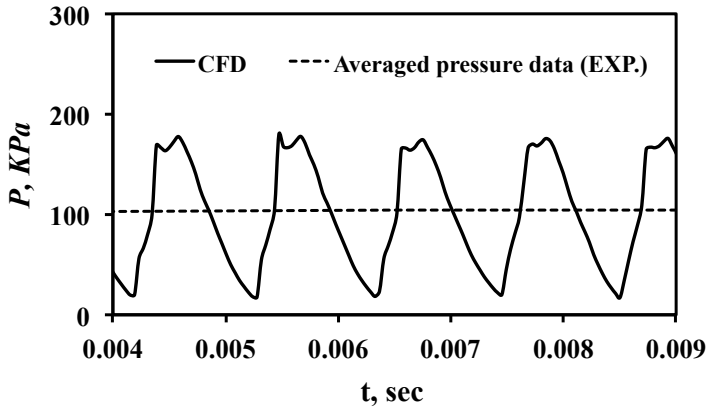

Figure 3.5: Comparison of the experimental averaged pressure data and CFD time-resolved data of point A (see Fig. 3.4)

represents the arc distance along the surface from the center, L the maximum arc length of the canopy, and d the diameter of the capsule. It is seen from the figure 3.8 that the computational results are in good quantitative agreement with the experimental data.

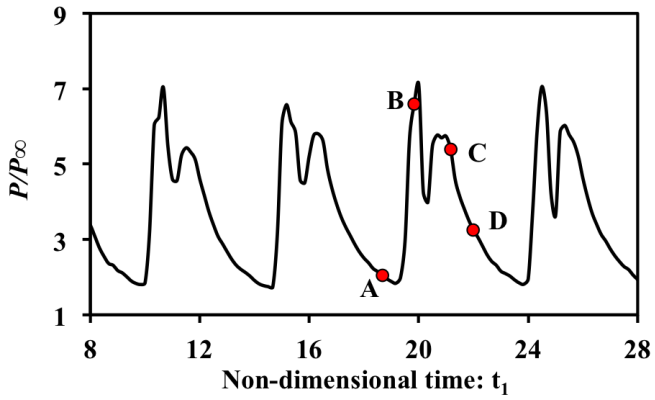

Figure 3.6: Numerical pressure histories at point Q (see Fig. 3.1), A, B, C and D correspond to the time locations shown in Fig. 3.7

3.4 Unsteady Aerodynamic Interactions

From Fig. 3.9, it is found that the bow shock (foreshock) formed ahead of the capsule inflates periodically and moves outward in the radial direction, thereafter including a hemisphere shape. This unsteady flow mode is called "*pulsation*" mode [102]. In order to investigate the mechanism of the pulsation mode for the parachute system, due to the complicated flow field, the typical number of frames per pulsation cycle can not be generally less than 10 [100, 103]. Following the method of analyzing this flow mode proposed by Feszty et al. [100], in this study 14 frames per period were chosen from CFD results to make two different types of flow visualization concurrently: Mach number contours and pressure contours. The former can demonstrate shear layer and boundary layer separation, while the latter enables us to identify shock wave and vortex. [100] Here it should be noted that this paper focuses on analysis of the unsteady flow field produced by interactions between the capsule and canopy.

Figure 3.9 shows the 14 instantaneous flow field frames, and the time interval (dimensionless) between two neighboring frames is 0.3. From the variation of the flow field during the pulsation cycle, it can be demonstrated using three processes; the process 1 corresponds to frames 1-3, the process 2 to frames 4-7, and the process 3 to frames 8-14.

Figure 3.10 shows the time variations of pressure at two different places of the parachute system, one is point Q at the edge of the capsule (see Fig. 3.11), another

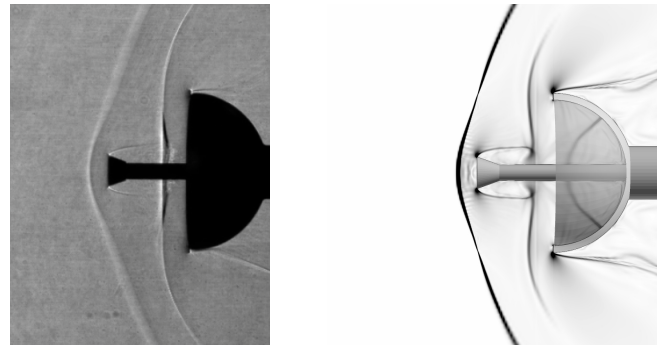

(A)

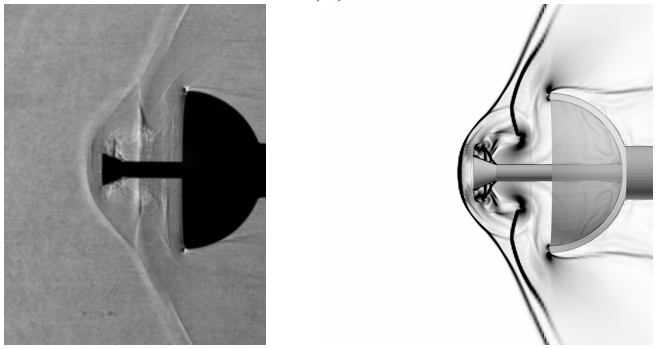

(B)

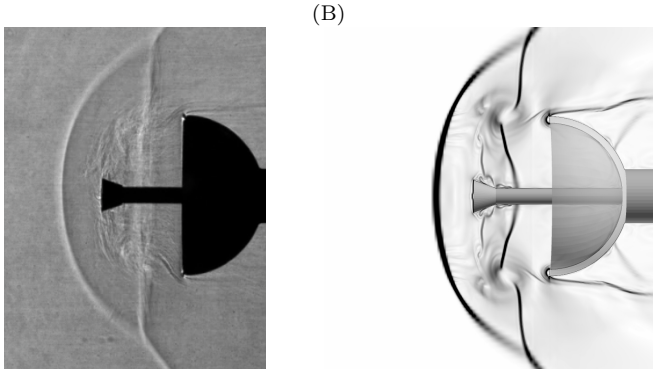

(C)

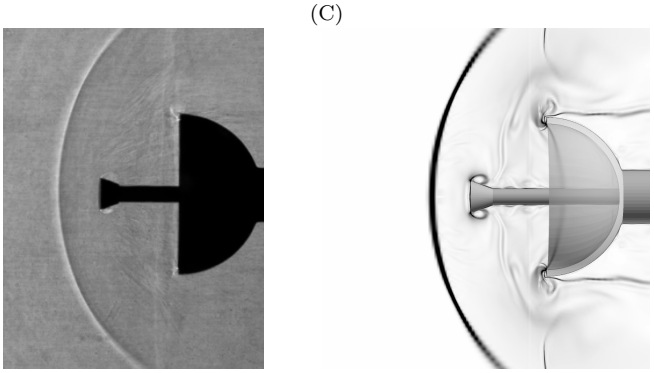

(D)

Figure 3.7: Shadowgraph pictures (left) and the corresponding density gradient contours in simulation (right)

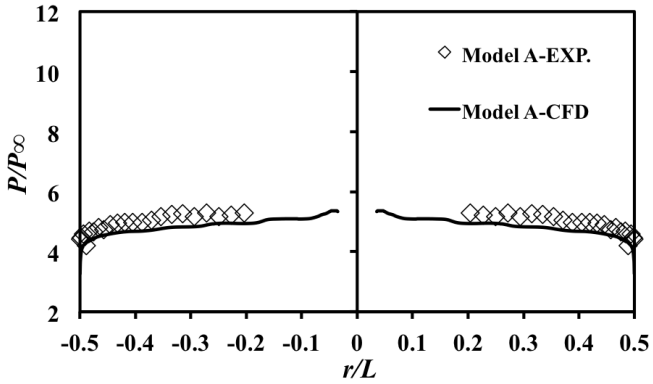

(a) Inner surface of canopy

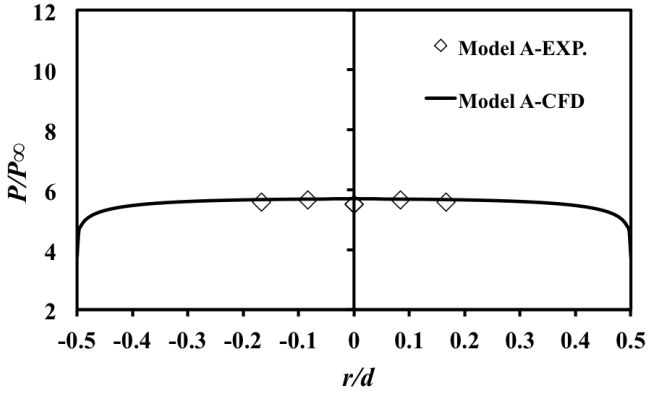

(b) Front surface of capsule

Figure 3.8: Averaged pressure distribution on surfaces of Model A

one is point O at the corner of canopy (see Fig. 3.11). These pressure traces can be used to define the time positions of the CFD results shown in Fig. 3.9. Moreover, the pressure difference between the canopy and the capsule can be properly identified from comparisons of these two pressure traces.

As shown from Fig. 3.11 to Fig. 3.16, schematic symbols and schematic diagrams are used to show and explain the various flow characteristics appearing throughout the pulsation cycle, where W refers to the shock wave, T the triple point, P the separated region, L the shear layer , and V the vortex region, and the number the order of its emergence. Because the geometry is axisymmetric and the flow fields are similar, those flow features were marked only once. It should be noted that for the schematic symbols appearing in the detailed explanation, please refer to the schematic diagrams shown from Fig. 3.11 to Fig. 3.16. In addition, in the following, the foreshock refers to the

shock wave ahead of the capsule, and the rear shock to the shock wave ahead of the canopy.

3.4.1 Flow Features of Process 1

This process corresponds to frames 1 to 3 in Fig. 3.9. The feature of this process is that no aerodynamic interference such as shock/shock or wake/shock interaction occur in the flow field, where the bow shock, or the fore shock, is nearly stable, and the capsule wake and the canopy shock are formed.

In frame 1 of Fig. 3.9, bow shock W1 (refers to Fig. 3.11,the symbols below are similar) has already expanded to its full extent and begins to go back toward the capsule; the boundary layer separates from the edge of capsule, so that shear layer L1 and vortex V1 generate in the wake zone.

From Fig. 3.10, we can see that during frames 1-3, the pressure inside the canopy decreases and takes almost minimum at frame 3 (see Fig. 3.10 (b)), while the pressure in front of the capsule becomes higher(see Fig. 3.10 (a)). This pressure difference makes shock W2 move toward the inside of canopy (see Figs. 3.9a and 3.9b). As it moves inward of the canopy, shock wave W2 interacts with the internal surface of canopy, the pressure there begins to rise, and another shock W3 is produced from there (see Fig. 3.9b and Fig. 3.11).

Moreover, as W2 goes downstream, it interacts with the boundary layer on the connecting rod and creates a separation region, P3; and P3 gradually grows and moves forward. At the same time a shear layer, L3, forms along the boundary of the separation zone P3 (see Figs. 3.9a, 3.9b and Fig. 3.11).

The flow characteristics of process 1 are that the gas inside the canopy is compressed by shock waves W2 and W3. When this compressed flow escapes from the edge of the canopy, it becomes supersonic (see Figs. 3.9b and 3.9c). As a result, the tip of canopy is exposed to this flow, so that a separation region, P2, forms. Following this, a shear layer, L2, forms in the wake region, leading to the development of a vortex region, V2 (see Fig. 3.11).

3.4.2 Flow Features of Process 2

This process corresponds to frames 4-7 in Fig. 3.9. The feature of this process is that aerodynamic interferences such as wake/shock interaction actually occur; specifically

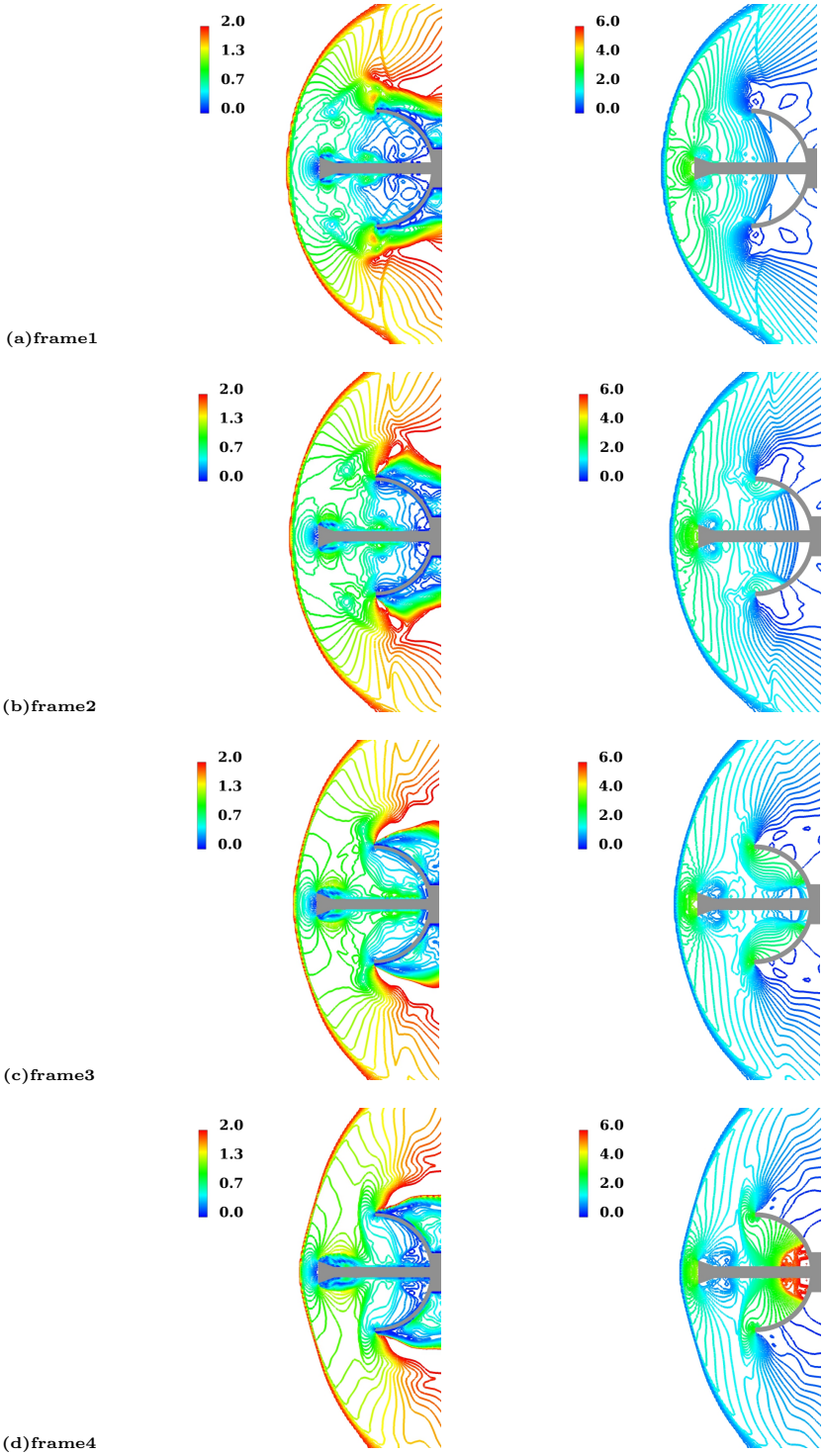

Figure 3.9: Pulsation mode for Mach of 2.0: Mach number contours(left) and pressure contours (right)(cont'd)

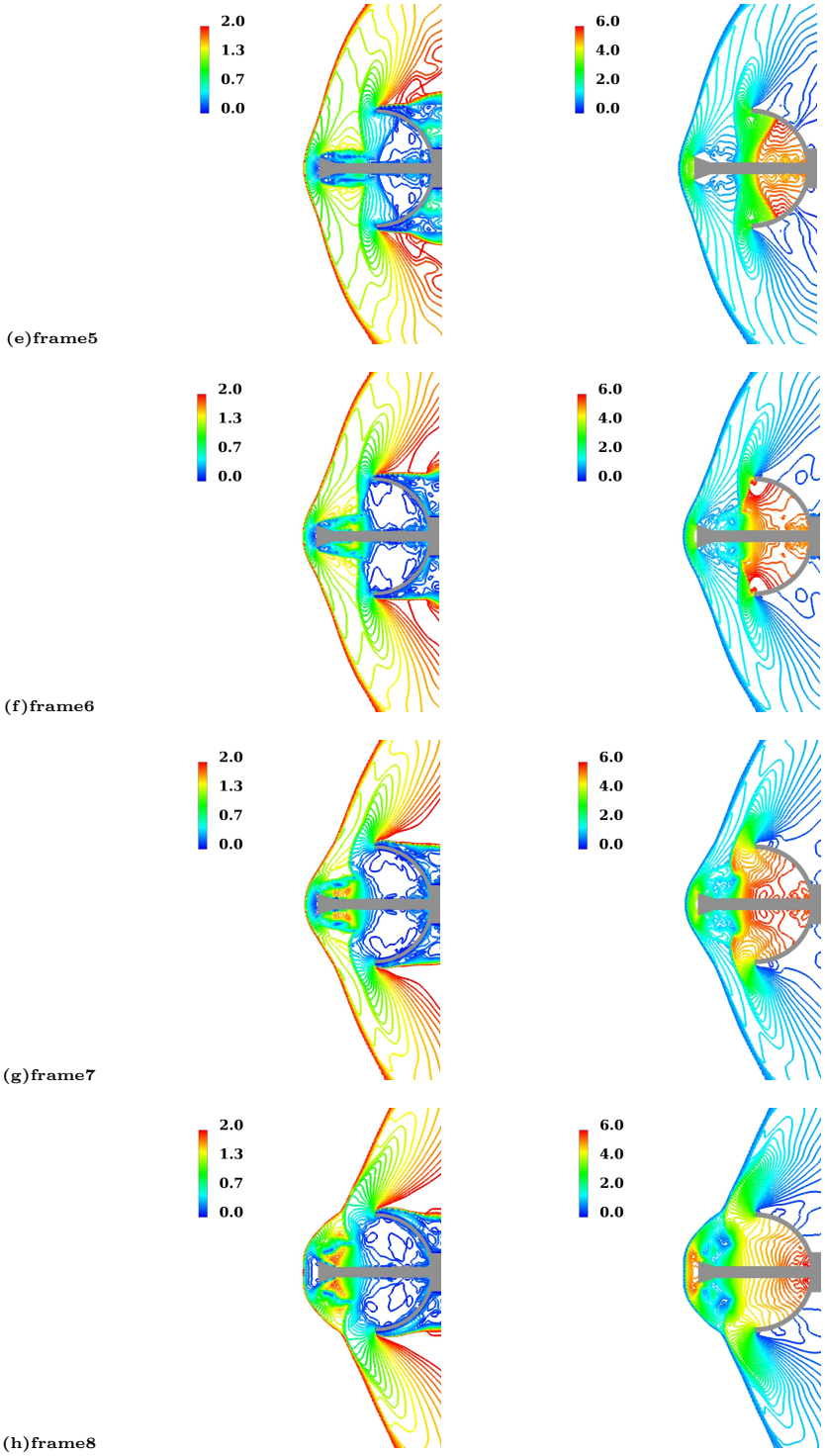

Figure 3.9: Pulsation mode for Mach of 2.0: Mach number contours(left) and pressure contours (right)(cont'd)

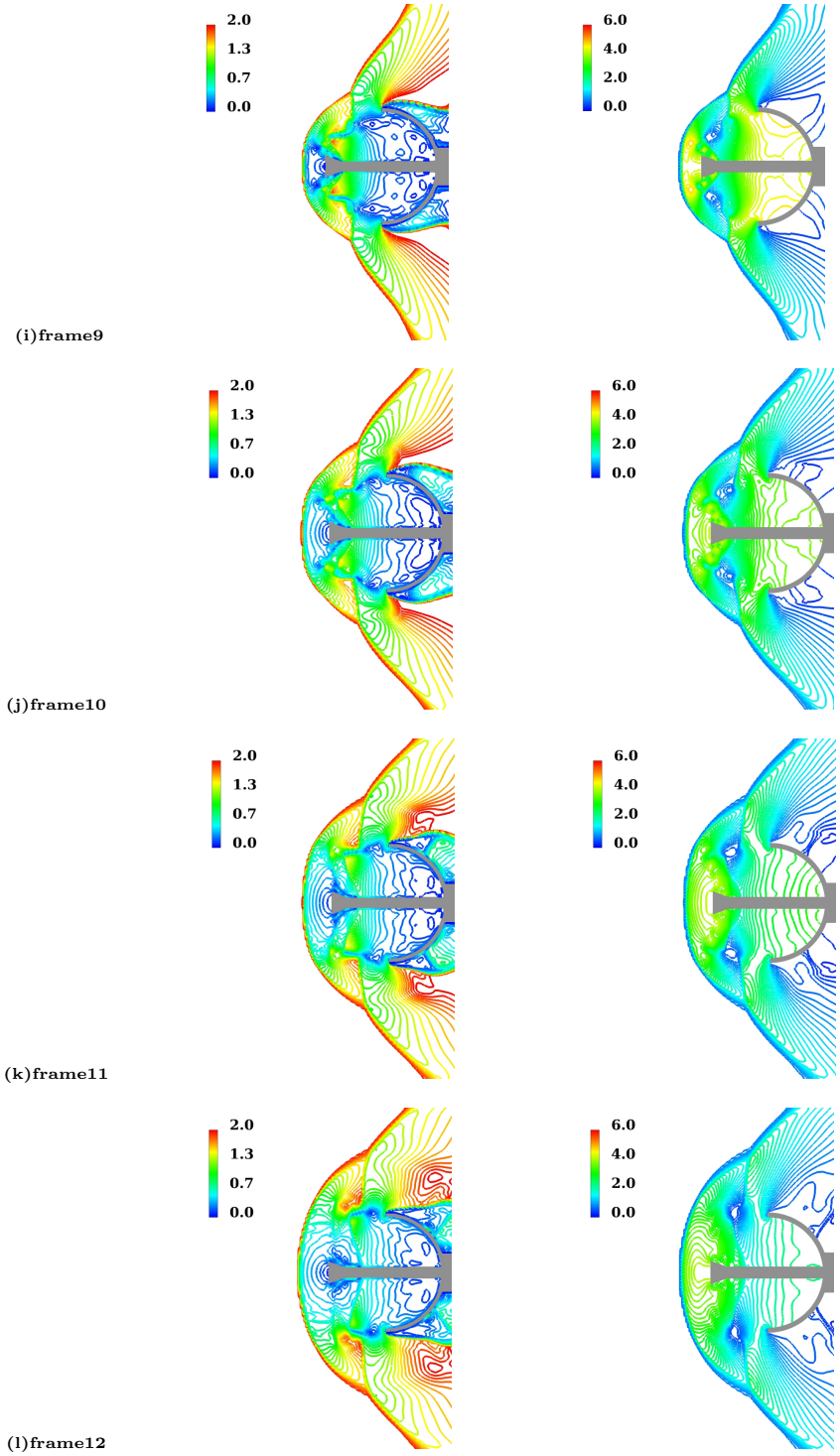

Figure 3.9: Pulsation mode for Mach of 2.0: Mach number contours(left) and pressure contours (right)(cont'd)

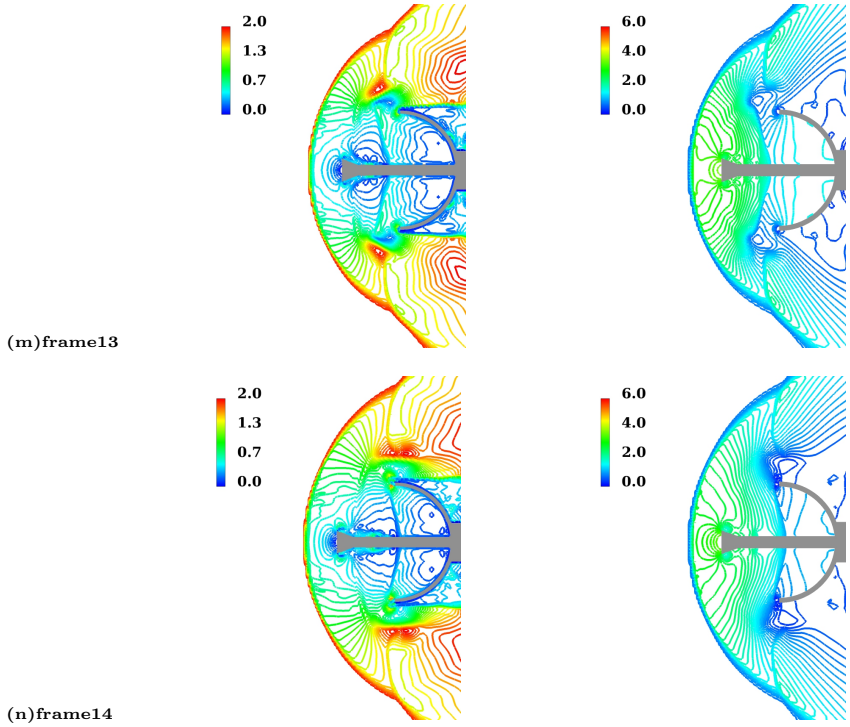

Figure 3.9: Pulsation mode for Mach of 2.0: Mach number contours(left) and pressure contours (right)

the capsule wake interacts with the canopy shock, and the intersections go upstream.

It is seen from Fig. 3.10(a) that during frames 4-6, the pressure around the capsule becomes smaller and reaches a minimum at the frame 6. Consequently, shock wave W1 moves closer to the capsule.

In frame 4 of Fig. 3.9, shock wave W2 almost reaches the corner, and then disappears. The pressure at the corner of the canopy becomes the first peak (see Fig. 3.10b), where shock wave W4 is produced (see Figs. 3.9d and 3.13). During this process, a definite vortex region, V3, can be observed at the corner of canopy, which forms behind the shock wave W4 (see Fig. 3.13). This is produced by virtue of the impact of a penetrating flow with a recirculation flow. This suggests that the approaching expansion of the trapped air in the corner is generated not only by a mass influx from upstream, but also by the inflation due to its high pressure. The vortex, V3, exits during almost the whole of process 2.

As shock wave W4 (see Fig. 3.12) expands toward upstream, another vortex region,

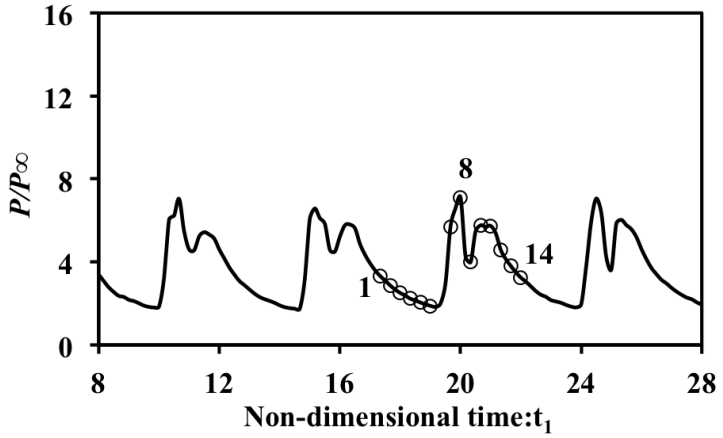

(a) Point Q at the edge of capsule (see Fig. 3.11)

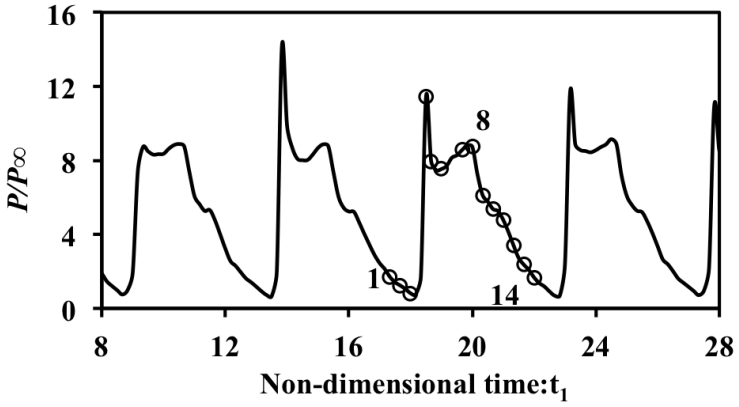

(b) Point O at the corner of canopy (see Fig. 3.11)

Figure 3.10: Time variations of pressure at two different places in Mach 2.0 pulsation case

V4, is generated by the interaction of W4 with the inner surface of the canopy, which moves with W4 and reaches the edge of the canopy, as shown in frame 6 of Fig. 3.9. This leads to the creation of a vortical region, V6 (see Fig. 3.9f and Fig. 3.12). In frame 5 of Fig. 3.9, shock wave W3 has already extended all over the entire canopy and has moved to the location of L1, interacting with it (see Fig. 3.9e).

In frame 6 of Fig. 3.9, shock wave W4 reaches the interference region of W3 and L1, and intersects them, so that a weak oblique shock, W5, is generated (see Figs. 3.9f and 3.12). As a result of the wake/shock interaction, the flow velocity in the wake region increases to become supersonic, so that the vortex region, V1, disappears (see

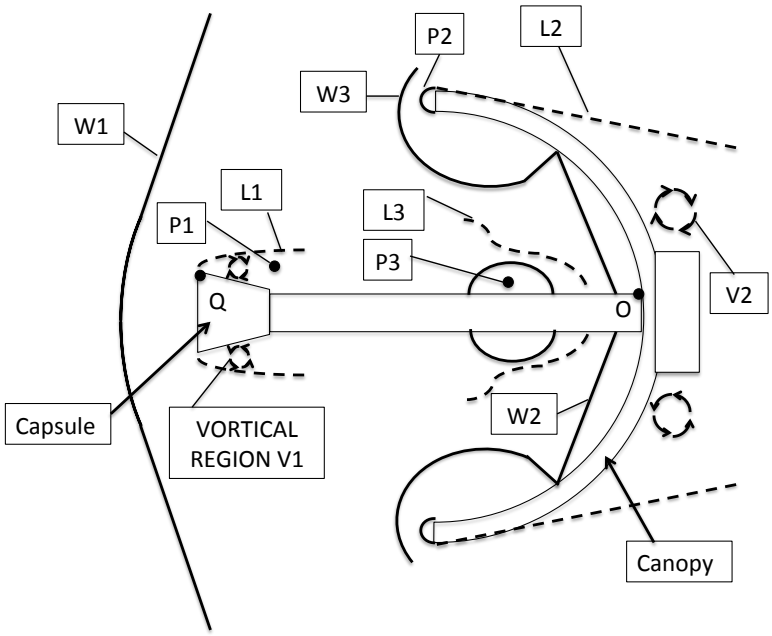

Figure 3.11: Schematic of the flow field in process 1, based on frame 2 of Fig. 3.9

Fig. 3.9f).

It is seen from Fig. 3.14 that the pressure behind shock wave W4 is higher than that in the wake region. Consequently, this pressure difference causes a strong pressure gradient, which induces a reverse flow; with the result that a definite vortex region, V5, develops at the foot of the shock wave W4, as clearly observed in Fig. 3.14. This vortex region was also observed in other pulsation phenomenon [100, 104]. The leading function of this flow phenomenon is a flow reversal [100]. The flow reverses and goes back to the wake region, through L1, W3 and W4 (see Fig. 3.14), which also causes the vortex V3 to disappear, due to the lack of mass influx.

Frame 7 of Fig. 3.9 shows that shock wave W4 merges with W3, and that vortex region V4 disappears. As a result of high pressure within the canopy, both shock wave W3 and shear layer L1 are forced to move upstream and begin to move outward, so that the vortex region V5 grows. At the same time, shock wave W5 rapidly extends toward upstream, and merges with W1 (see Fig. 3.9h).

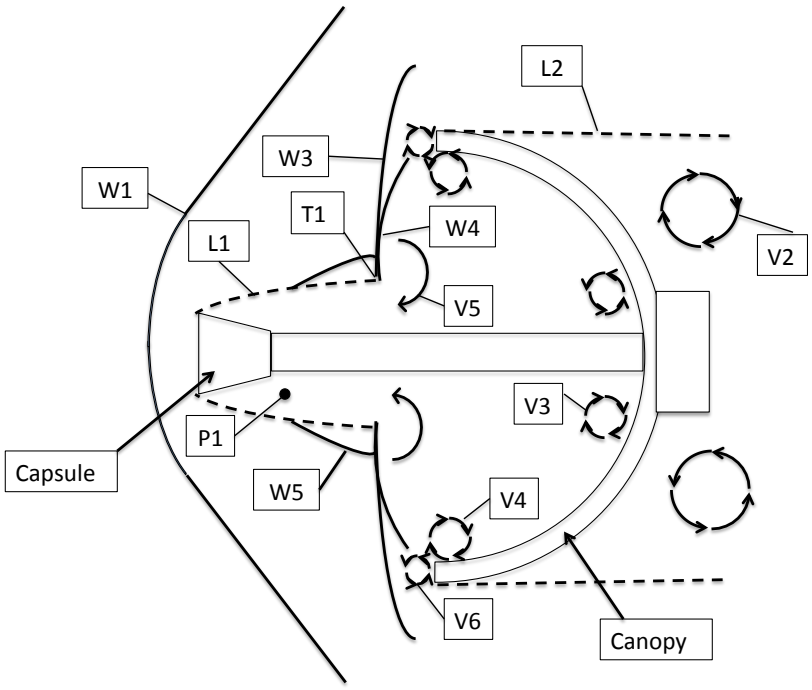

Figure 3.12: Schematic of the flow field in process 2, based on frame 6 of Fig. 3.9

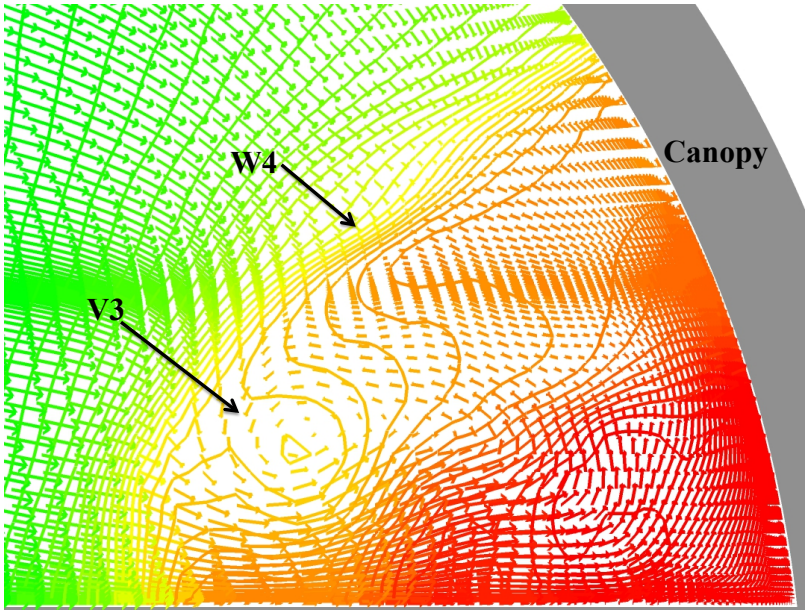

Figure 3.13: Velocity vectors and pressure contours near the corner of canopy in frame 4

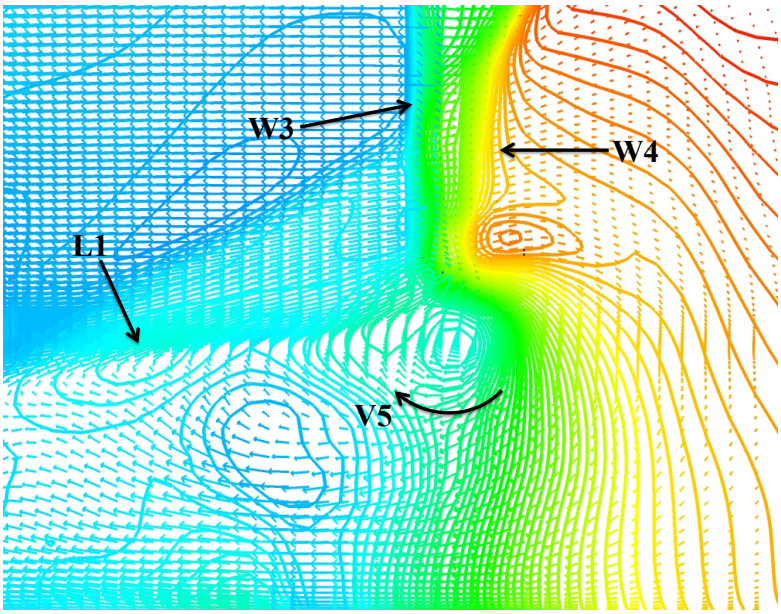

Figure 3.14: Velocity vectors and pressure contours in the interaction region, based on frame 6 of of Fig. 3.9

3.4.3 Flow Features of Process 3

Process 3 corresponds to frames 8-14 in Fig. 3.9. The feature of this process is that the triple shock systems inflate; i.e., the intersections of the fore and rear shocks move more outward in the radial direction, so that the foreshock takes a hemisphere shape.

In frames 8 and 9 of Fig. 3.9, shock wave W3 intersects W1, and generates a triple shock system consisting of W1, W3 and W6 (see Figs. 3.9h and Fig. 3.15), where the pressure inside the canopy reaches the second maximum (see Fig. 3.10b). It is seen from Fig. 3.9 that during process 3, the shock system of W1, W3 and W6 move outward in the radial direction all the time, where W1 takes a hemisphere shape. Due to this effect, the flow from separation region P1 (see Fig. 3.12) moves toward the bottom of the capsule, creating an oblique shock wave, W7 (see Figs. 3.9i and 3.15).

In frame 8 of Fig. 3.9, the pressure at the edge of capsule reaches a maximum (see Fig. 3.10a), leading to shear layer L1 becoming separated from the capsule (see Fig. 3.15). The movement of the shear layer can also be observed in another pulsation phenomenon [100] to respond to the expansion of the interference region. Here, as a consequence of this effect, the flow in separation region P1 (refers to the process 2) reaches the front of the capsule, and collides with the flow originating from the front

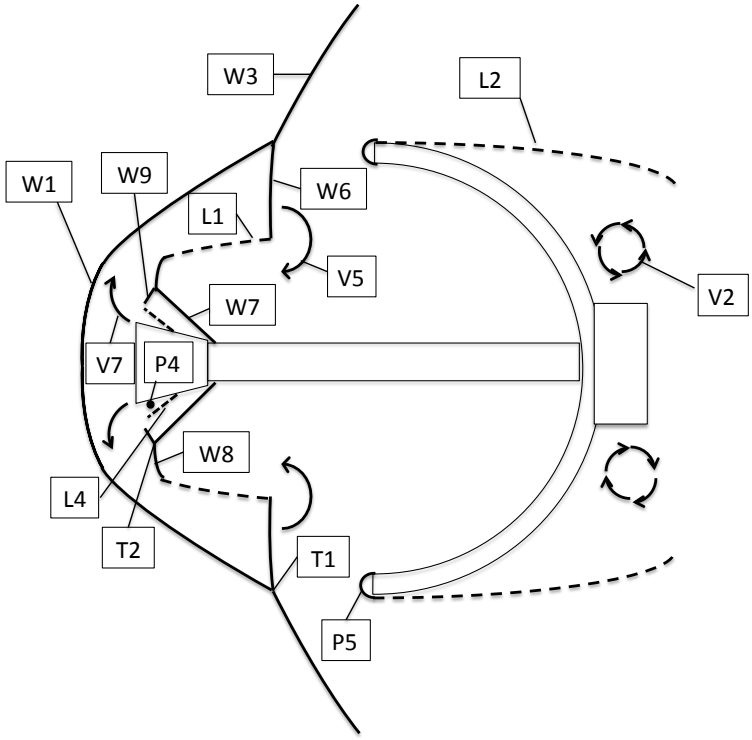

Figure 3.15: Schematic of the flow field in the early stage of process 3, based on frame 8 and 9 of Fig. 3.9

area of capsule, causing a vortex region, V7, to be generated. In this process, the supersonic flow from P1 (see Fig. 3.12) has to be decelerated before entering the vortex region V7. Hence, the internal normal bow shock W8 is created between shear layer L1 and the capsule. As it interacts with the boundary layer on the neck of the capsule, another separation region, P4, occurs, and shear layer L4 forms at the boundary of P4 (see Fig. 3.9h and Fig. 3.15).

In frame 9 of Fig. 3.9, shock wave W7 interacts with W8 and produces a new shock wave, W9, which constructs the second triple shock system (see Fig. 3.15).

In frames 10 and 11 of Fig. 3.9, as the pressure around the capsule remains high, the shock system with W7, W8 and W9 gradually strengthens and also move outward, which leads to the enlargement of shear layer L4 and separation region P4 as well as the lateral movement of vortex region V7. In frame 12, the shock waves W8 and W9 merge with W7, and the vortex region V7 gradually disappears.

From frames 13 and 14 of Fig. 3.9 and Fig. 3.16, it is seen that the shock system

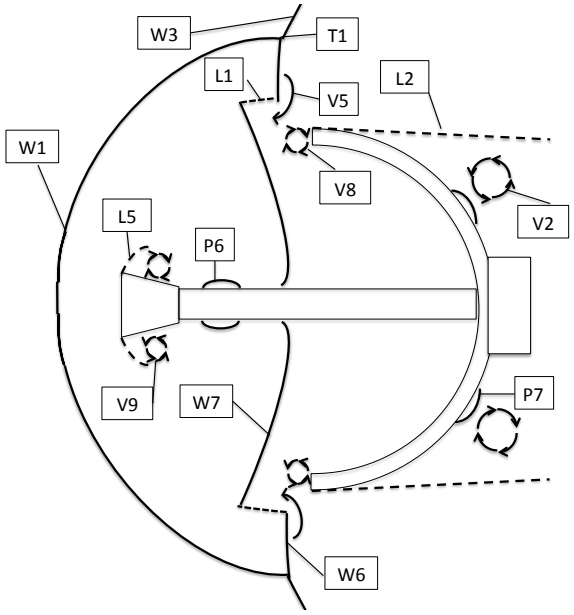

Figure 3.16: Schematic of the flow field in the late stage of process 3, based on frame 13 of Fig. 3.9

W1-W3-W6 has reached the periphery of the canopy and continues to move in the radial direction. However, this system has already been weakened, and will disappear before going to the frame 2 of next cycle, due to the low pressure within the canopy and around the capsule. As a result, shear layer L1 and vortex region V5 also vanish gradually. Moreover, we can see that shear layer L1 and vortex region V5 hold and develop during almost the whole interaction process. Thus, this is a key factor to drive the pulsation phenomenon considered here in this study [100].

As seen in frames 13 of Fig. 3.9, as shock wave W7 moves downstream due to the pressure difference, it interacts with the boundary layer on the connecting rod, so that a new separation region, P6, is created. At the same time the flow escapes from within the canopy, where the fluid is pressurized, and is accelerated in the vicinity of the canopy edge. Consequently, it collides with separated region P5 (see Fig. 3.15), and generates a vortex region, V8. In frame 14 of Fig. 3.9, shock wave W7 reaches to the canopy edge, and vortex region V8 disappears.

During process 3, the unsteady upstream flow has a relatively large effect on the flow behind the canopy. In the early stage (see Fig. 3.15), the high pressure fluid escapes from inside the canopy, and moves downstream at supersonic speed, where

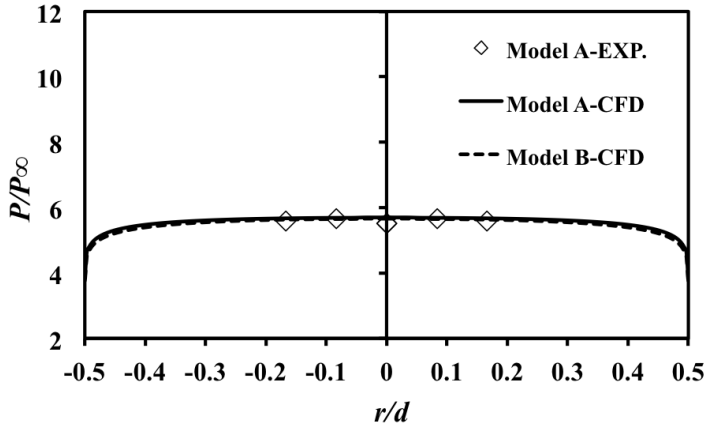

(a) Inner surface of canopy

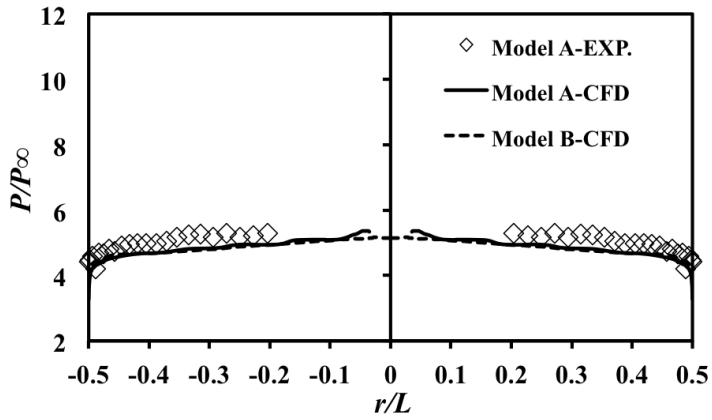

(b) Front surface of capsule

Figure 3.17: Comparison of averaged pressure distribution on typical surfaces between model A and model B

shear layer L2 and vortex region V2 are depressed; On the other hand, in the late stage (see Fig. 3.16), as the triple shock system T1 becomes weakened, the flow behind the canopy moves upstream, and collides with the outer surface of the canopy, causing a separation region, P7, to be generated.

3.5 Effect of Connecting Rod

Model A is used to compare with the experiment. In real conditions, the connecting rod is impossible. In order to examine the effect of the connecting rod on the aerodynamic interaction for the parachute, model B is employed. From Fig. 3.17, it is seen that the

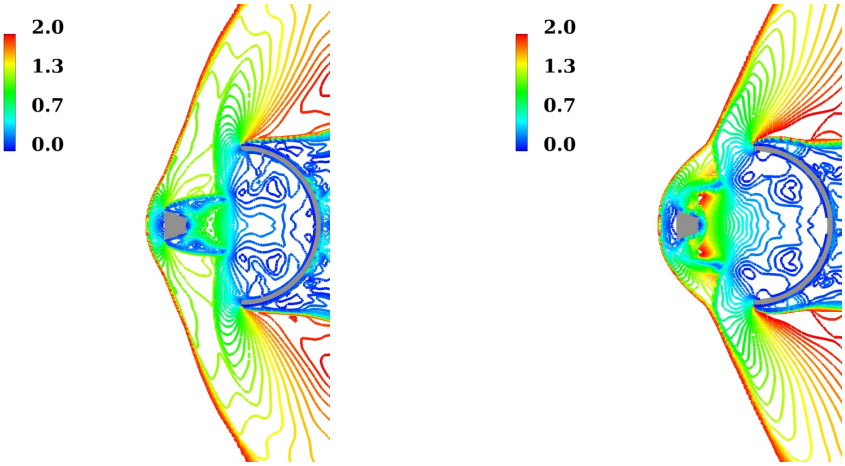

Figure 3.18: Mach number contours of model B in two instantaneous flow fields: frame 6 (left) and frame 8 (right)

averaged pressure distribution on the typical surfaces of model B are in fair agreement with the ones of model A.

Two representative instantaneous aerodynamic interaction flow fields of model B in Fig. 3.18. Comparing with the same frames of model A, one can see that they are in good agreement. Except for some differences in the shape of the shock wave envelope because of the connecting rod, the pulsation mechanism of model B is identical to model A. Therefore, model A is reasonable and meaningful.

3.6 Effect of Mach Number

In experiment, we can increase Reynolds number by increasing the flow speed. However, it is difficult to change Mach number while keeping Reynolds number constant. On the contrary, in CFD, this can be easily achieved by changing the model size [105]. Here based on this approach, computation was carried out for two cases: M=1.6 and M=2.2 under the same conditions as the case where M=2.0.

From Fig. 3.19 and 3.20, it can be seen that for other Mach numbers the unsteady flow mode is consistent with that for Mach of 2.0. As the freestream Mach number is different, the period of a pulsation cycle becomes different. Here two representative instantaneous flow fields with aerodynamic interactions similar to the frames 6 and 8 for Mach of 2.0 are shown in Figs. 3.19 and 3.20. Comparing these three cases,

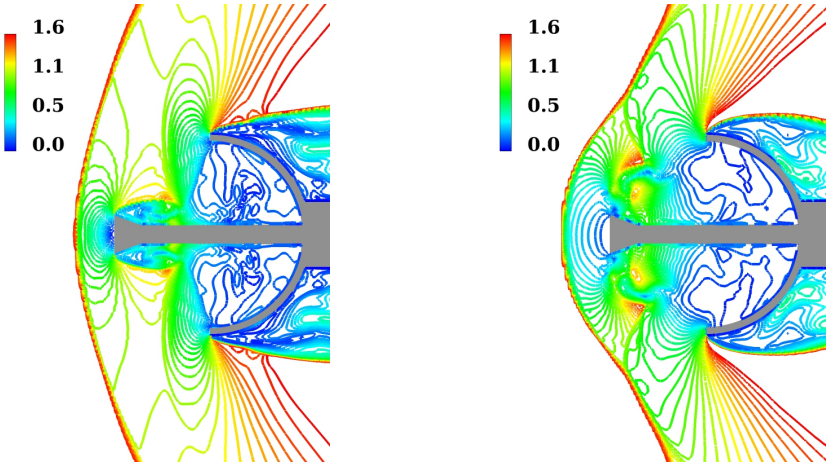

(A) (B)

Figure 3.19: Mach number contours of model A in two instantaneous flow fields for Mach 1.6 case

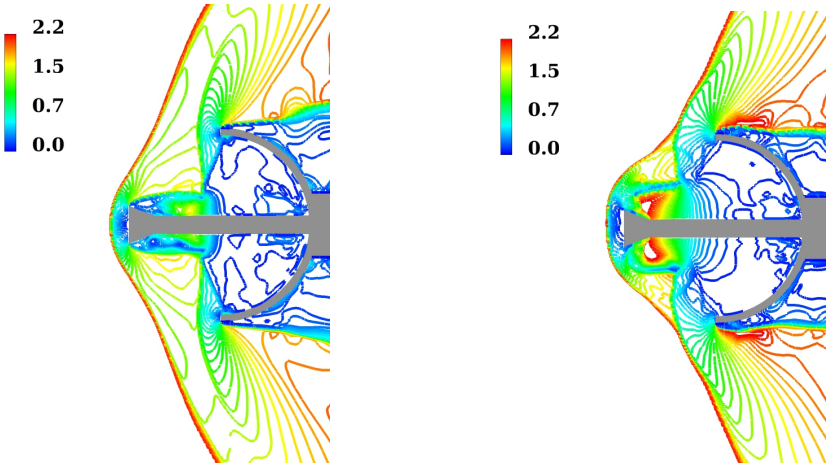

(A) (B)

Figure 3.20: Mach number contours of model A in two instantaneous flow fields for Mach 2.2 case

it can be seen that when Mach number is 2.2, the bow shock ahead of the capsule moves closer toward the capsule, and becomes more conical in shape, leading to a decrease in the distance between the capsule bow shock and the canopy bow shock (see Fig. 3.20A). Consequently, coupling of the capsule wake with the canopy bow shock becomes stronger, and the region with aerodynamic interaction comes closer to the

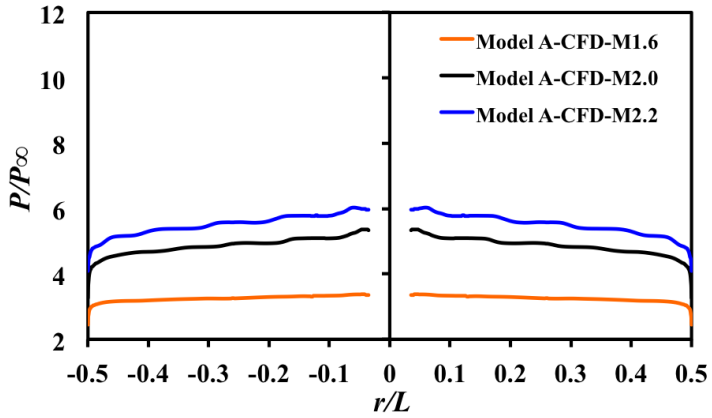

(a) Inner surface of canopy

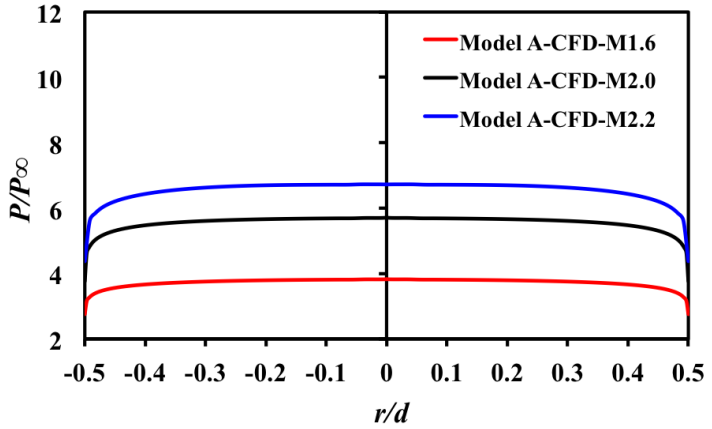

(b) Front surface of capsule

Figure 3.21: Effect of Mach number on averaged pressure distribution on parachute surfaces

edge of canopy at higher Mach number (see Fig. 3.20B), which causes the pressure on the parachute surfaces become larger, as shown in Fig. 3.21.

3.7 Summary

The unsteady flow field with pulsation phenomenon, which occurs in the flow over a parachute model placed in a freestream with a Mach number of 2.0, was numerically simulated. The results obtained in this study can be summarized as follows:

- The computational results of model A, which has a connecting rod between the capsule and canopy, agreed with experimental data.

- When reducing the trailing distance between the capsule and canopy, complicated wake/rear shock and foreshock/rear shock interactions were observed.
- There were two key factors for the present pulsation phenomenon; one was the pressure difference between the capsule and the canopy, and the other the shear layer and vortex region produced by the wake/rear shock and the foreshock/rear shock intersections.
- Judging from the results of models A and B, the effects of the connecting rod on the flow field and pressure distribution on the body surfaces were rather small; the pulsation mechanism for model B was identical to that for model A.
- The unsteady flow pulsation phenomenon examined in this study can be demonstrated using three processes during one cycle. 1) At process 1, the bow shock ahead of the capsule was nearly stable. 2) At process 2, the capsule wake interacted with the canopy shock, and the movement of the wake-rear shock interaction was predominant. 3) At process 3, intersections of the fore and the rear shocks moved more outward in the radial direction.
- In the unsteady flow pulsation mode, the bow shock formed ahead of the capsule periodically inflated and moved outward in the radial direction, which was caused by upstream propagation and lateral movement of the complicated wake/rear shock and foreshock/rear shock interaction systems.
- The mechanism for the unsteady flow mode was found to be consistent at supersonic speeds ranging from Mach 1.6 to 2.2. As the freestream Mach number increased, the bow shock ahead of the capsule moved closer toward the capsule, and the capsule wake interacted more strongly with canopy bow shock, and the aerodynamic interaction region came closer to the edge of the canopy, which led to the pressure on the parachute surfaces becoming larger.

Chapter 4

Two-Dimensional Flexible Parachute

4.1 Introduction

In this chapter, two-dimensional flexible parachute model are numerically simulated on Cartesian grids using the IBM as a coupling method at supersonic speeds ranging from M = 1.6 to M = 2.1. One of the features in the present method is a coupling scheme, where the fluid and structure are considered as a single part, and the equations that govern the both parts are solved simultaneously in a time domain. This is critical for the accuracy and efficiency of the method.

The objective of this study is to make sure whether that the IBM can be employed to solve the supersonic flexible parachute problems, and to analyze the effect of aerodynamic interference on the performance of the parachute system in detail. Moreover, the effect of Mach number on the flexible parachute system will be examined.

4.2 Computational Method and Conditions

The present calculation for this case was carried out using an in-house structured single block code, where the compressible Navier-Stokes equations were solved to simulate the supersonic flow field around the parachute models. To evaluate the inviscid fluxes, Simple High-resolution Upwind Scheme (SHUS) [74] was employed, and the accuracy of the scheme was improved by using the 3rd-order MUSCL scheme [78, 79] with the Van Albada flux limiter [80], while viscous terms were evaluated by the 2nd-order central

differencing scheme. As one of features in the present numerical method, the 3rd-order total variation diminishing Runge-Kutta scheme [82] is used to obtain time accurate results in unsteady calculations. The coefficient of viscosity was computed according to Sutherland's law [66, 67]. Initial conditions in the calculations were set to the free stream values. The freestream conditions used in the current study is the same with the rigid parachute case, as shown in table 3.1 of Chapter 3. Non-slip and adiabatic conditions were applied to the body surfaces.

In the present study, the immersed boundary method [85, 86] was employed to deal with the boundary of a flexible canopy. The IBM based on Cartesian grid has some advantages; however, it is limited in solving the complex turbulent flows [106]. Thus, here no turbulence models are used, which is also consistent with the rigid case and easy to compare with each other.

A mass-spring-damper (MSD) model [88] was applied to solve the structural dynamics of the parachute, where the parachute was treated as an assembly of mass nodes attached to springs and dampers. The explicit 2nd-order Runge-Kutta scheme is used to obtain time-variations in the canopy model calculation.

Here in order to solve the fluid and structure equations simultaneously, the method of strong coupling (see Fig. 2.7 of Chapter 2) is employed for the two-dimensional case.

4.3 Two-Dimensional Parachute Model

In this case, a two-dimensional flexible canopy is connected by suspension lines to a capsule, as shown in Fig. 4.1. The shape of canopy is a semicircle, and its radius is 55 mm. The capsule is fixed, and its size is shown on the right side of Fig. 4.1, where its base length, d, is 24mm. The axial distance from the capsule base to the inlet of the canopy, X, is 57mm, and the trailing distance, X/d, is 2.375. The canopy employed here is modeled by 1607 mass nodes connected by springs and dampers. The uniform flow is noted as U, and the gravity force is also considered ,which acts in the negative z direction. It should be pointed out that canopy nodes of the edge parts are compelled to just move along a circular path, with its center placed at the capsule location, since the radial components Xr and Zr of the forces in the x and z directions are equal to the tension force of suspension lines [85].

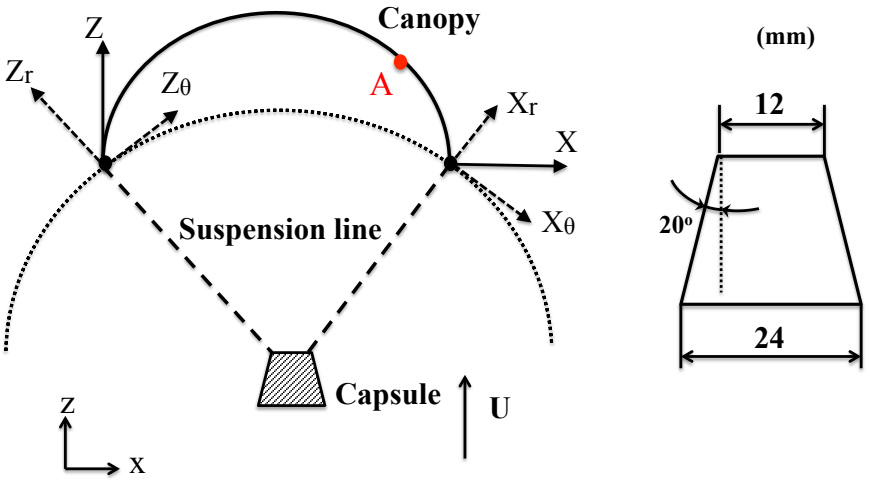

Figure 4.1: Two-dimensional parachute model

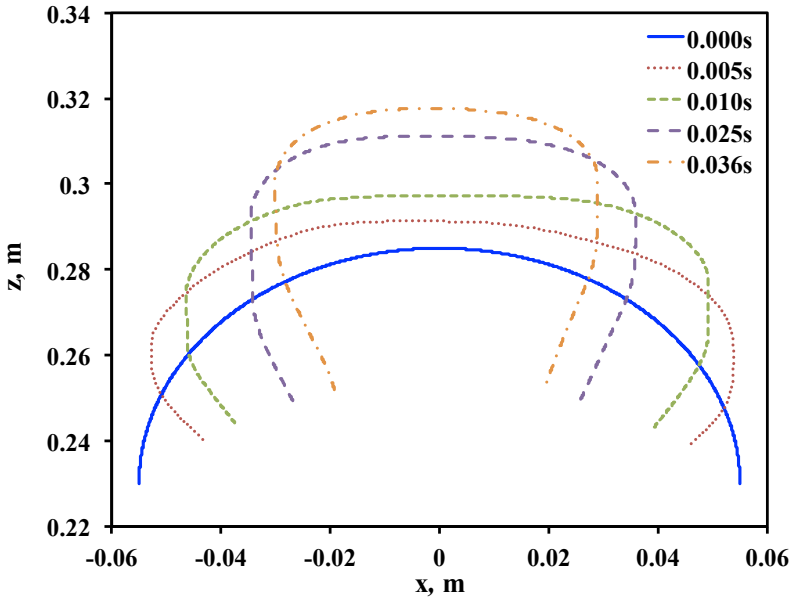

Figure 4.2: Time variations of canopy shape

4.4 Canopy Shape Variation

Fig. 4.2 shows the time variations of the canopy shape, where the initial canopy diameter is defined at z=0.23m as the distance between the two edges. Furthermore, it can be seen that the edge part of the canopy shrinks all the time. In addition, it moves in the z direction. This phenomenon will be interpreted in the next section.

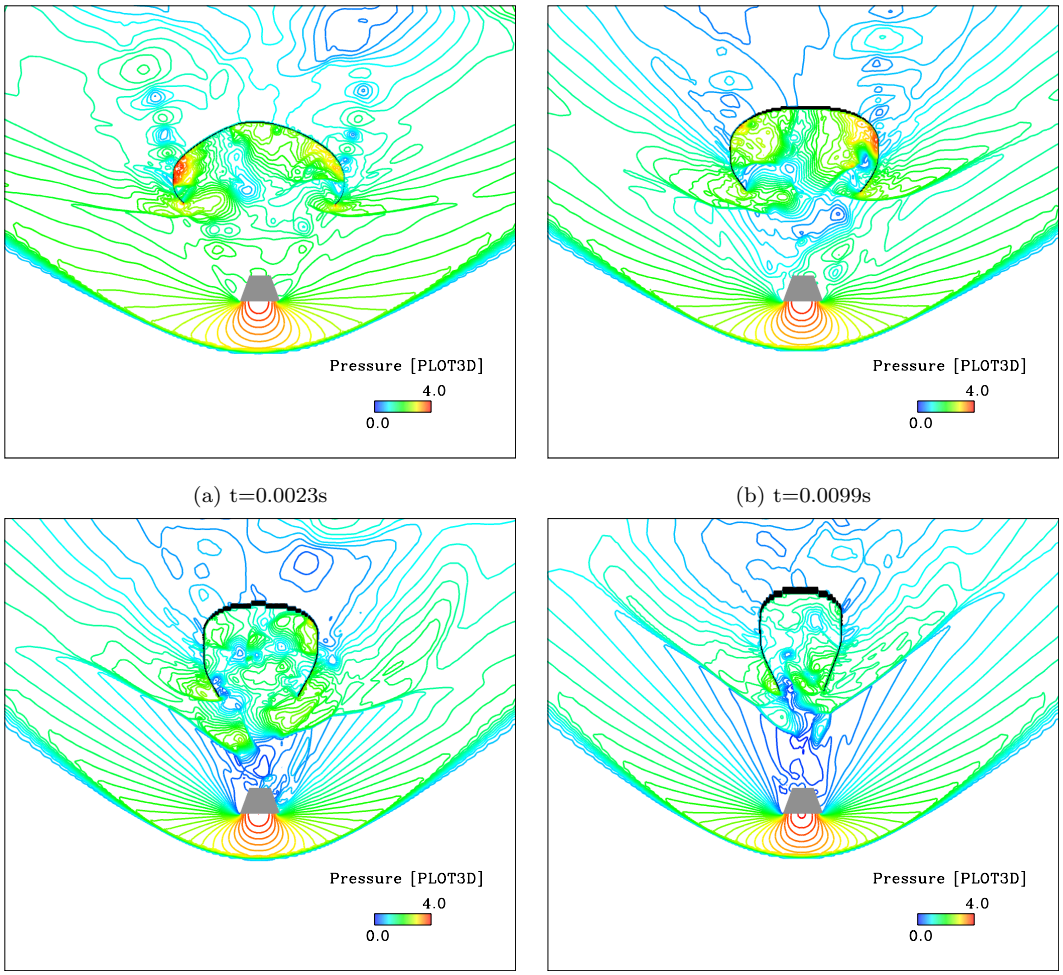

(a) t=0.0023s

(b) t=0.0099s

(c) t=0.0201s

(d) t=0.0353s

Figure 4.3: Pressure contours at four different times

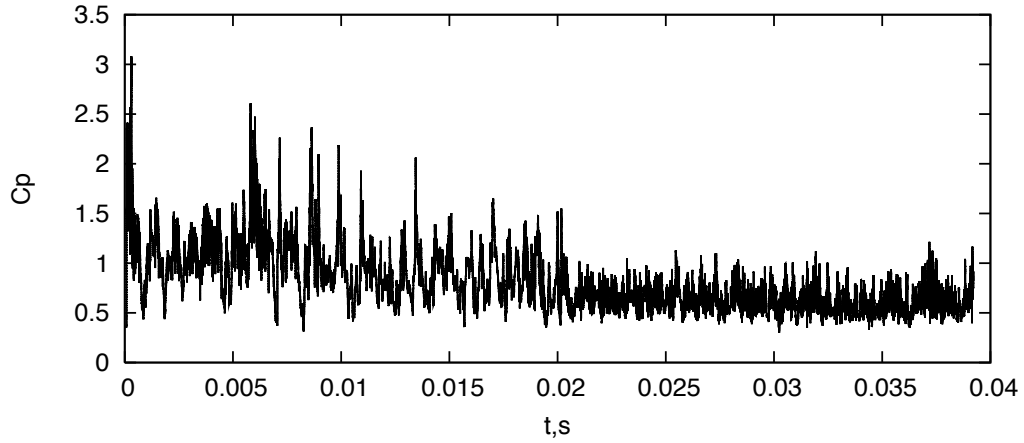

Figure 4.4: Time variations of pressure coefficient at point A (see Fig. 4.1)

4.5 Unsteady Aerodynamic Interaction

Four representative instantaneous pressure contours around the parachute are shown in Fig. 4.3. In Fig. 4.3(a), we can see that the shock wave is formed ahead of the canopy (rear shock), which forces the edge of canopy to shrink toward the center. In addition, separation vortices are formed on each side of the canopy, which lead to large pressure differences between the inner and outer surfaces of the canopy. Thus the canopy is inflated in the x direction and moves in the z direction. In Figs. 4.3(b)-(d), the separation vortices linger over the canopy top, and these pressure differences continue to cause the canopy to rise up. The shock waves ahead of the canopy continue to contract its edge parts. In Figs. 4.3(c) and 4.3(d), it can be seen that the aerodynamic interaction between capsule wake and canopy shock goes upstream due to the severe contraction of the canopy, which causes the pressure inside the canopy become smaller. It should be noted that the shock wave ahead of the capsule (foreshock) remains steady all the time.

The time history of the pressure coefficient, Cp , at point A (see Fig. 4.1) is shown in Fig. 4.4, which indicates the pressure inside the canopy has a cyclic change. Here the pressure coefficient, Cp, is defined as follows(see Ref. [107]):

$$C_p = \frac{2}{\gamma M_\infty^2}(\frac{P}{P_\infty} - 1) \tag{4.1}$$

After about 0.02s, its amplitude becomes smaller, because the canopy severely shrinks and the aerodynamic interaction goes upstream (see Fig. 4.3). The time history of

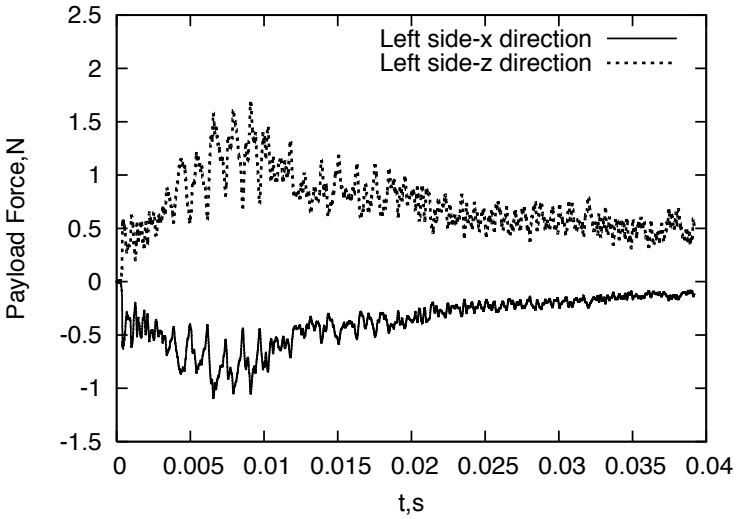

(a) Left side

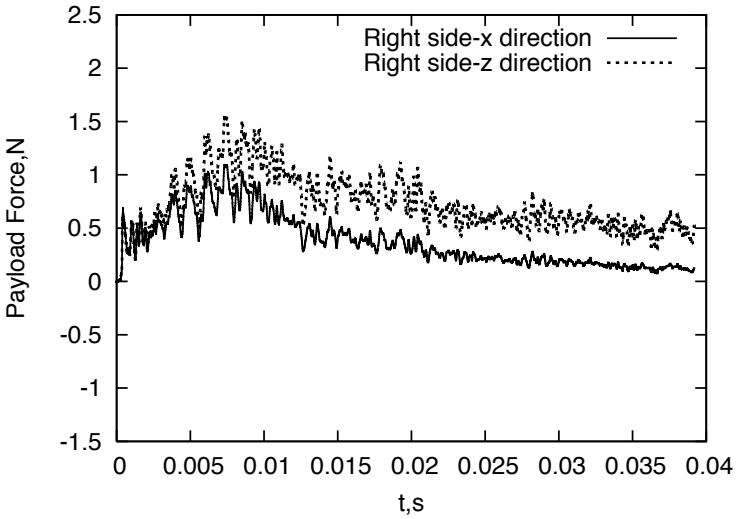

(b) Right side

Figure 4.5: Time variations of payload force on two sides

payload force exerted on the right and left edges are shown in Fig. 4.5, where the x and z directions are shown in Fig. 4.1. The x directional force on the left edge is negative due to a balance with the tension of suspension lines . From this figure we can see that the payload force also has a periodic change due to the cyclical variation of the flow field, and that the amplitude fluctuations gradually becomes smaller over time. It is noted that the payload force rises at first, in response to the larger pressure differences

between the inner and outer canopy surfaces by the separation vortices. After about 0.01s, the separation vortices linger over the top of the canopy, the pressure difference between both sides of the canopy becomes small, so that the payload force falls. In addition, the z directional force is always greater than the x directional one, which is associated with angles of the suspension lines.

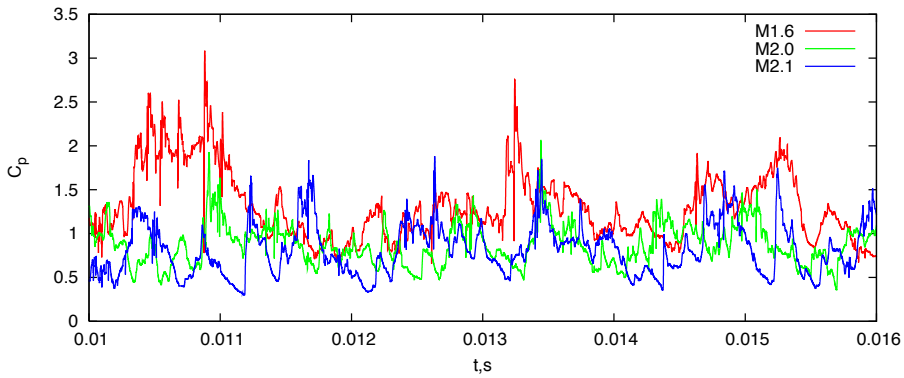

(a) Initial stage

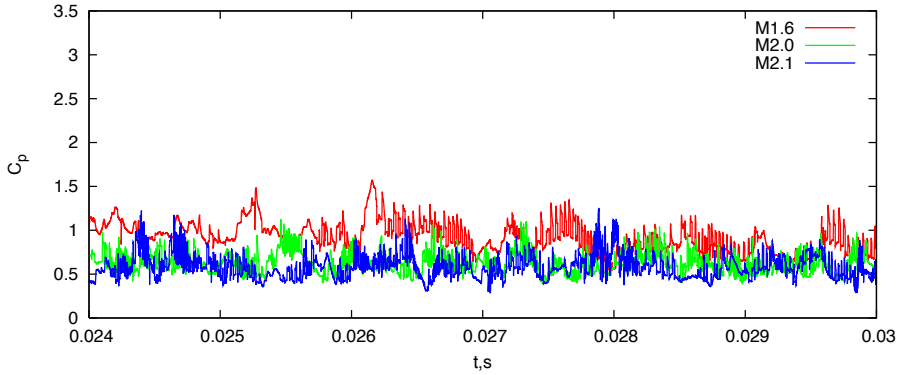

(b) Last stage

Figure 4.6: Time variations of pressure coefficient of point A inside the canopy (see Fig. 4.1) at three Mach number cases

4.6 Effect of Mach Number

In experiments, it is difficult to vary the Mach number while holding constant the Reynolds number, since increase in the speed leads to increase in the Reynolds number. In computational studies, this is easily realized; specifically we changes the model

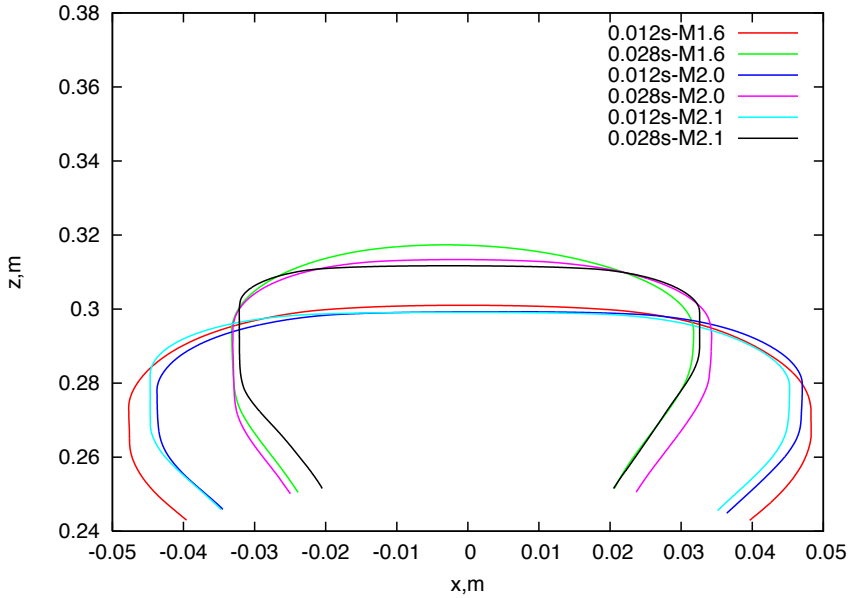

Figure 4.7: Comparison of canopy shape at two different times for the Mach number cases

size [105]. Here in this study, based on this approach, computation was carried out at M=1.6 and M=2.1 under the same computational conditions.

The comparison of time variations of pressure coefficient at point A (see Fig. 4.1) for three Mach number cases are shown in Fig. 4.6. From Fig. 4.6, we can see that the frequency of change in pressure coefficient at point A (see Fig. 4.1) is very high due to the unsteady flow field. Therefore, in order to see the differences more easily, we consider two stages: initial and last stages. From these figures, it is noticed that as Mach number decreases, the pressure coefficient at point A becomes larger. Moreover, in the last stage both the pressure coefficient and its vibration amplitude become smaller, which reveals that the flow inside the canopy turns to less unstable than that in the initial stage. Seeing Fig. 4.3(c) and Fig. 4.3(d), when the canopy shape becomes smaller, the canopy shock detaches from the edge, and then interacts with the wake in the region between the capsule and canopy. This interaction has no obvious vibrational motion in this stage, due to the stable foreshock. As a result, this aerodynamic interference pressures the canopy edge all the time, reduce the mass flow into the canopy, and cause the change of pressure become small.

The comparison of canopy shape for the three Mach number cases is shown in

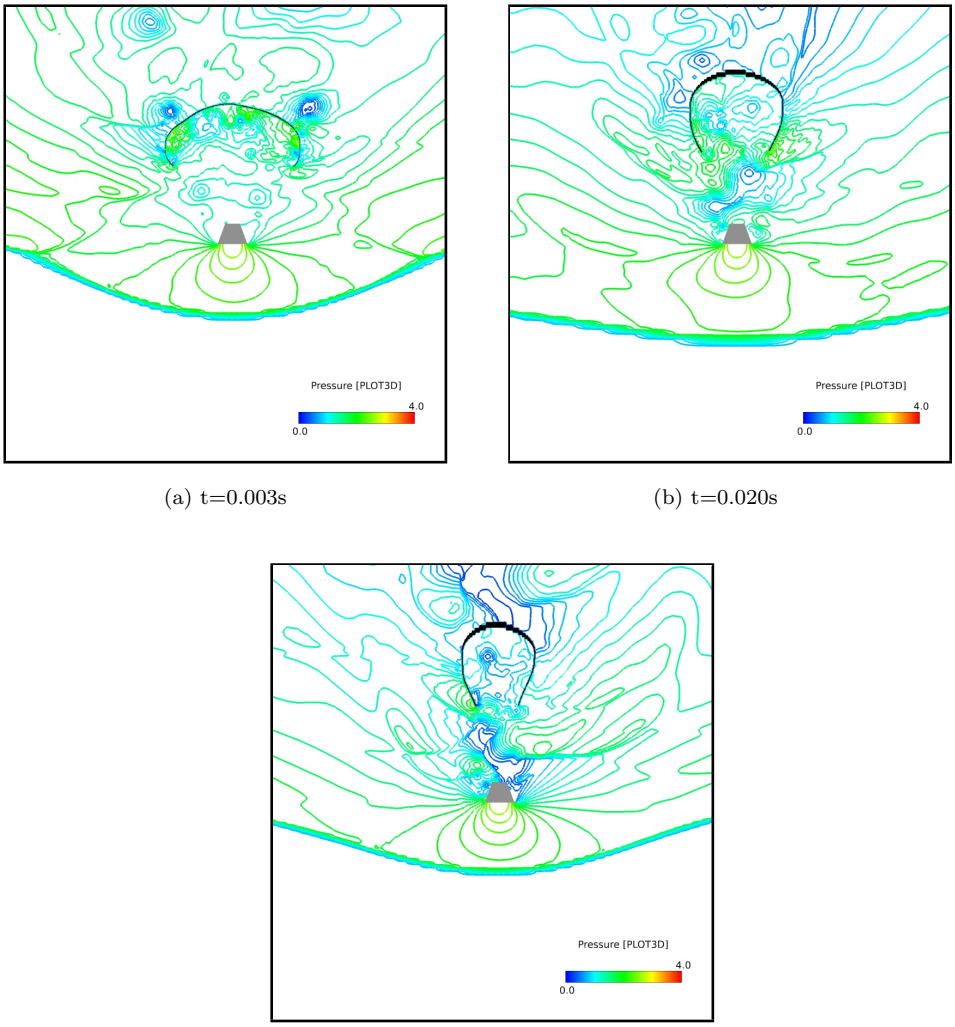

(a) t=0.003s

(b) t=0.020s

(c) t=0.028s

Figure 4.8: Pressure contours at three different times at Mach 1.6

Fig. 4.7. The computation was carried out by changing the model size, but the sizes of canopy at Mach 1.6 and 2.1 are converted to the original one for easy comparison. It can be seen that at t=0.012s the deformation of canopy shape has the same trend in the three cases, and that as Mach number increases, the shrinkage becomes larger, in particular the edge part. This is because the capsule wake always interacts with the canopy shock near the canopy edge at higher Mach number. However, at t=0.028s, in Mach 1.6 case, the foreshock moves downstream and the aerodynamic interaction between the capsule wake and canopy shock becomes stronger, so that the shape of

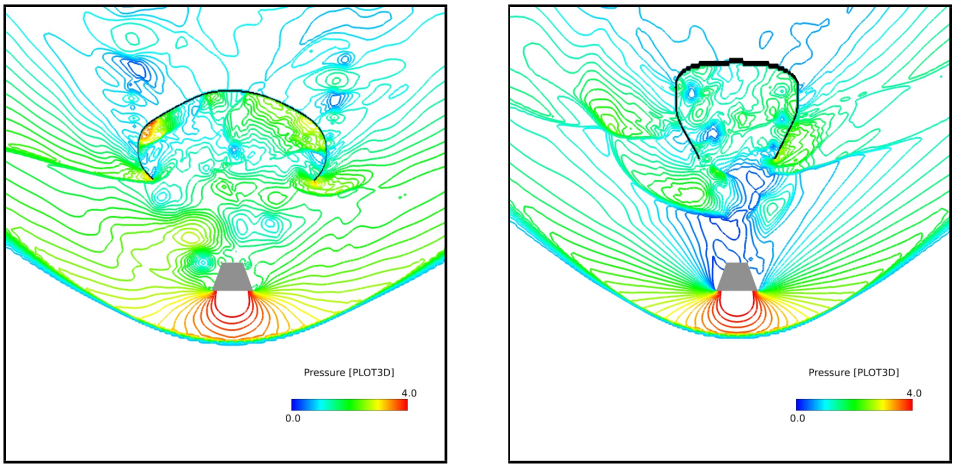

(a) t=0.003s (b) t=0.020s

Figure 4.9: Pressure contours at two different times at Mach 2.1

canopy has a larger shrinkage. On the other hand, the changes in canopy shape at Mach 2.0 and 2.1 keep the same trend as the initial stage.

Instantaneous pressure contours around the flexible parachute at Mach 1.6 and 2.1 are shown in Fig. 4.8 and Fig. 4.9, respectively. Comparison at the same time among the three Mach number cases, we can see that the case of Mach 1.6 is quite different from the other cases. This is because the shape of shock and the detachment distance depend on freestream Mach number [108]. In this case the shock wave ahead of the capsule is not conical and moves upstream due to the effect of periodically pressurizing the canopy. In this stage the wake from the capsule is weak. It is interesting to see that in Fig. 4.8(c), the canopy shape becomes much smaller, and that the shock wave ahead of the capsule moves downstream due to the low pressure region around the parachute. In this stage the wake becomes stronger and interacts with the shock wave ahead of the canopy. Pressure decreases inside the canopy (see Fig. 4.6), which accelerates the contraction of the canopy. In addition, the flow field characteristics and the change trends are the same by and large for the Mach 2.0 and 2.1 cases. This is the reason for the phenomena shown in Fig. 4.7.

4.7 Summary

In the chapter, two-dimensional flexible parachute models were simulated numerically at supersonic conditions. The results obtained are summarized as follows:

- Time variations of change in the canopy shape for two-dimensional parachute models were successfully simulated on Cartesian grids using the immersed boundary method as well as the strong coupling scheme at supersonic speeds ranging from M=1.6 to M=2.1.

- In the two-dimensional parachute case, only the steady foreshock and the wake/rear shock interaction were observed, due to the weak interference and severe deformation of the canopy.

- In the two-dimensional parachute case, as the shape of shock and the detachment distance depend on freestream Mach number, at Mach 1.6 the shock wave ahead of the capsule was not conical and moved upstream under the effect of the cyclic pressurization to canopy. When the canopy shape became much smaller, the foreshock moved downstream. On the other hand, as Mach number decreased, the pressure coefficient at point A on the canopy surface became larger. In addition, the flow field characteristics and the change trends were the same by and large for Mach 2.0 and 2.1 cases.

Chapter 5

Axisymmetric Flexible Parachute

5.1 Introduction

In this chapter, axisymmetric flexible parachute models are numerically simulated on Cartesian grids using the IBM together with the weak fluid-structure coupling method at supersonic speeds ranging from M = 1.6 to M = 2.1. In order to solve the coupling problem, the fluid and structure are considered as a single part, and the equations that govern the both parts are solved separately in a time domain.

The objective of this study is to predict the flow field and analyze the effects of aerodynamic interaction and Mach number on the flexible parachute system. In addition, it is necessary to do further validation that the IBM can be employed to solve the supersonic flow over the axisymmetric flexible parachute models.

5.2 Computational Method and Conditions

The axisymmetric compressible Navier-Stokes equations were solved to simulate a flexible parachute by using an in-house CFD code. For spatial discretization, inviscid numerical fluxes were evaluated by Simple Low-dissipation AUSM scheme (SLAU) [77], the accuracy of this scheme was improved by the 2nd-order MUSCL scheme [78, 79] with the Van Albada flux limiter [80]. The viscous terms were evaluated by the 2nd-order central differencing scheme. Regarding time integration, the 2nd-order Runge-Kutta scheme was used to obtain time accurate results in unsteady calculations. The coefficient of viscosity was computed according to Sutherland's law [66, 67]. Initial conditions in the calculations were set to the free stream values. The freestream conditions used

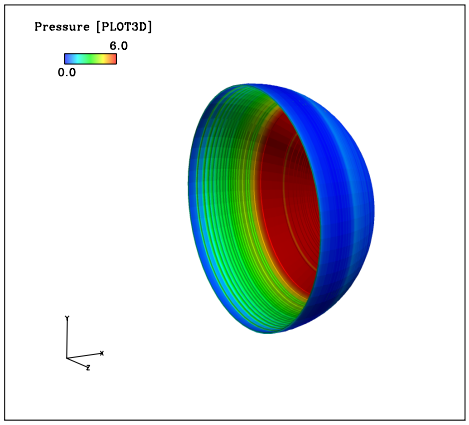

(a) t=0.00004s

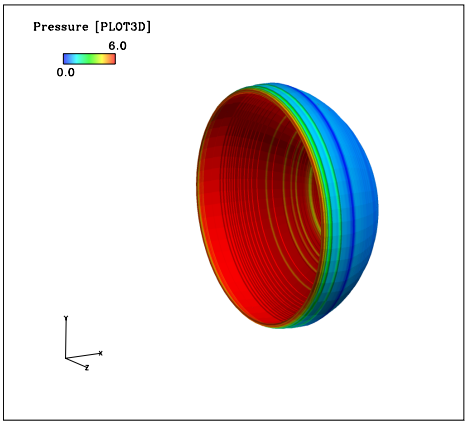

(b) t=0.00392s

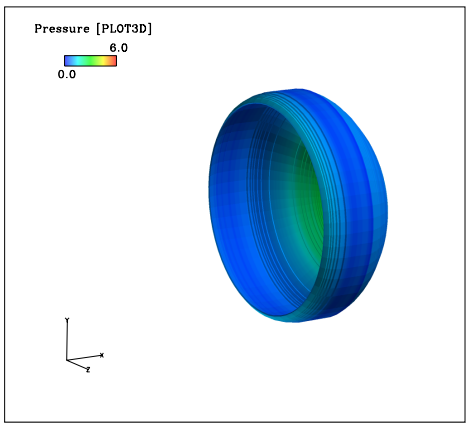

(c) t=0.01190s

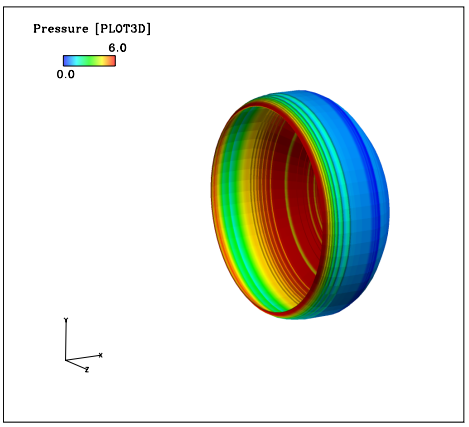

(d) t=0.01534s

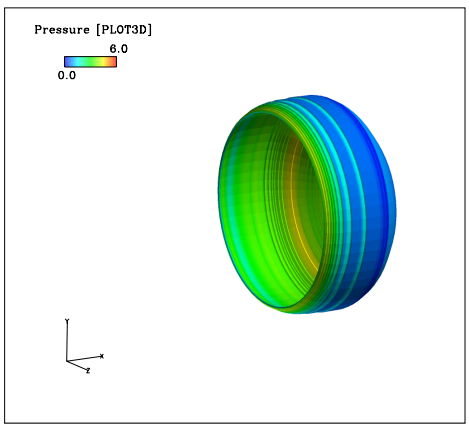

(e) t=0.02397s

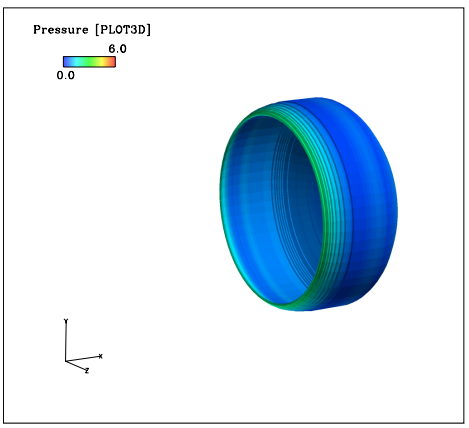

(f) t=0.02821s

Figure 5.1: Time variations of canopy shape

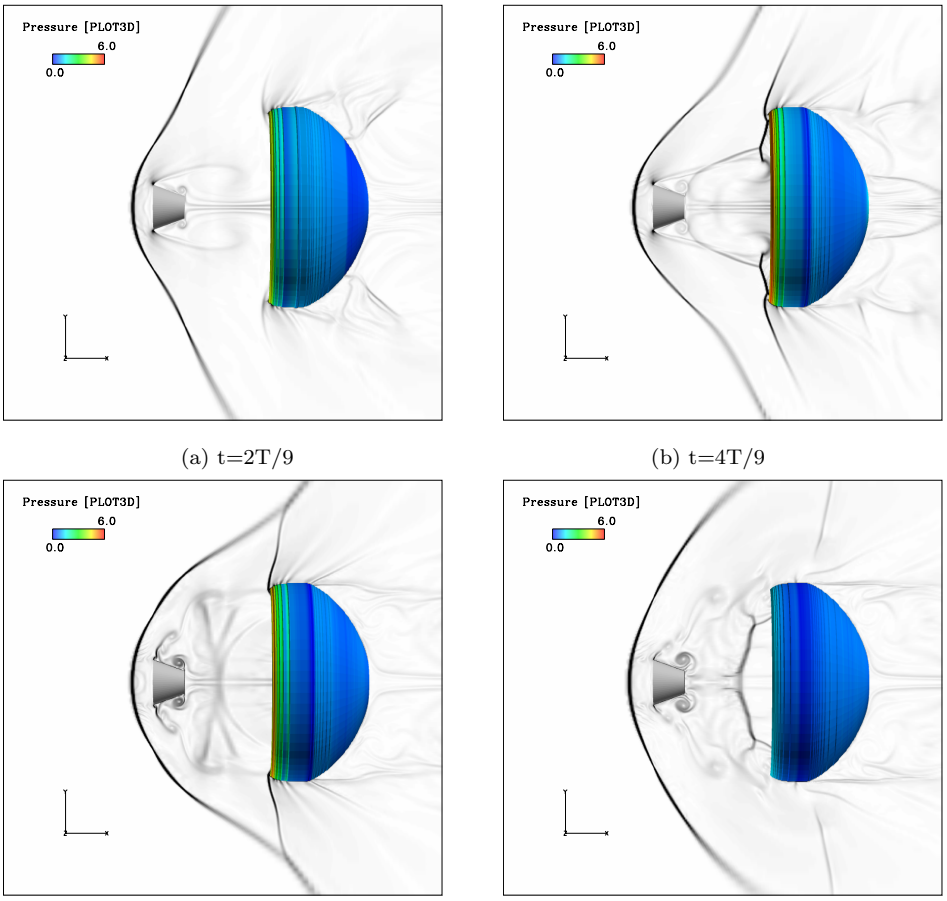

(a) t=2T/9 (b) t=4T/9

(c) t=6T/9 (d) t=8T/9

Figure 5.2: Density gradient contours around the flexible parachute at Mach 2.0; T is a period

in the current study is also consistent with the table 3.1 of Chapter 3. Non-slip and adiabatic conditions were applied to the body surfaces. No turbulence models were used because of the same reasons as the two-dimensional case.

In the present case, the immersed boundary method [85, 86] was also employed to deal with the boundary of a flexible canopy, the mass-spring-damper (MSD) model [88] was applied to solve the structural dynamics of the parachute. The explicit 2nd-order Runge-Kutta scheme was used to obtain time-variations in the canopy model calculation. In addition, the method of weak coupling (see Fig. 2.7 of Chapter 2) was employed for the axisymmetric flexible parachute case.

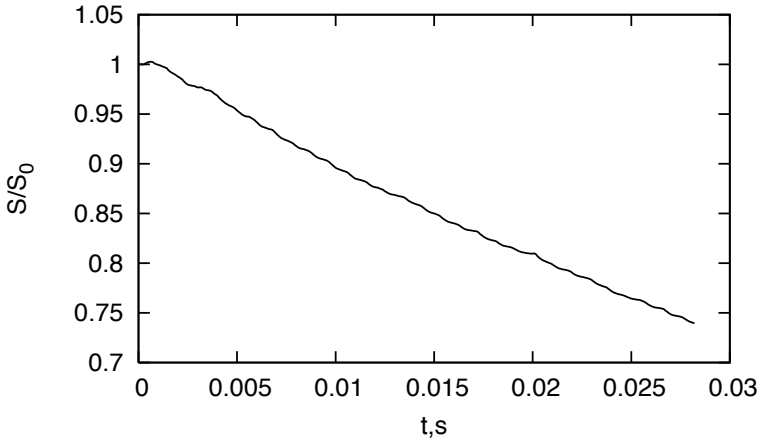

Figure 5.3: Time history of projected frontal area of canopy

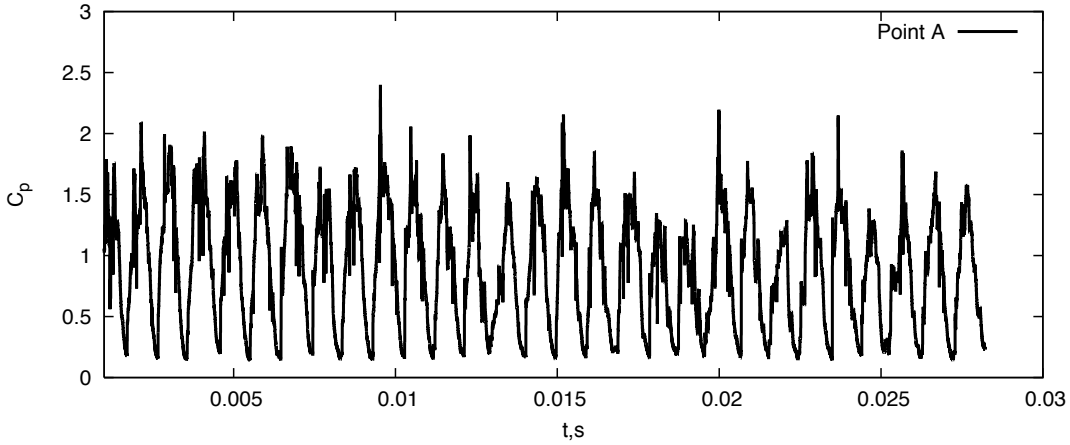

Figure 5.4: Pressure coefficient at point A (see Fig. 4.1 of Chapter 4) on the canopy surface

5.3 Axisymmetric Parachute Model

In this chapter, an axisymmetric model of a flexible parachute was employed to simulate the flow field and the deformation of canopy with aerodynamic interactions. The values of the model size are the same as those in two-dimensional case (see Fig. 4.1 of Chapter 4).

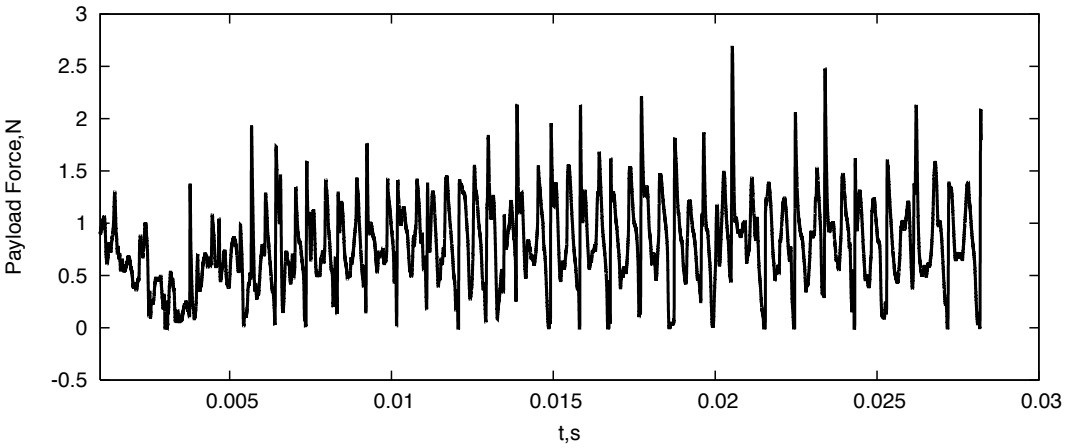

Figure 5.5: Time history of payload force

5.4 Canopy Shape Variation

The time variations of canopy shape are shown in Fig. 5.1, where the colors represent the pressure on the inner and outer canopy surfaces. From this figure, we can see that the edge of canopy contracts all the time, and that the pressure inside the canopy changes periodically, and the pressure at the edge of the outer canopy surface also has a large change.

5.5 Unsteady Aerodynamic Interaction

Four representative instantaneous flow fields are shown in Fig. 5.2, where the colors of the canopy represent the pressure on the inner and outer canopy surfaces, and wake/rear shock and foreshock/rear shock interactions are observed. During the interactions, the shock wave ahead of the canopy is always located near the edge part, which first interacts with the wake (see Fig. 5.2 (b)) and then foreshock (see Fig. 5.2 (c)). This produces high pressure force and causes the edge part to shrink. It is noted that the bow shock formed ahead of the capsule is periodically inflated and moves radially outward, including a hemispherical shape, this unsteady flow mode is called a "*pulsation*" mode [102], which is caused by the lateral expansion of the wake/rear shock and foreshock/rear shock interactions.

Figure 5.3 shows the time variations of the ratio of the projected frontal area of the canopy to its initial area S_0. This curve suggests a geometrical interpretation of the

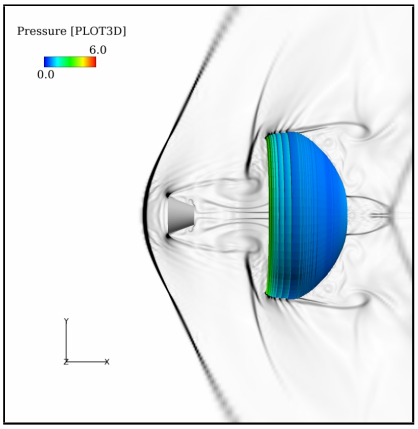

(a) t=4T/9

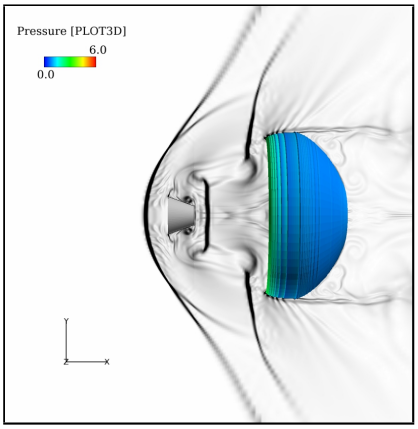

(b) t=6T/9

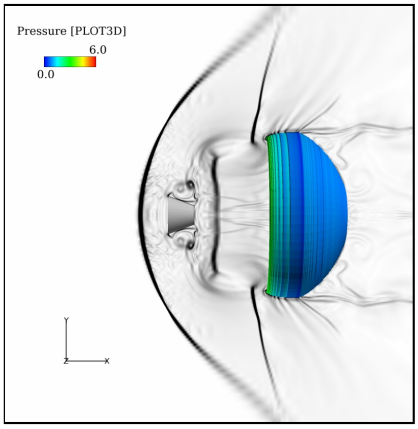

(c) t=8T/9

Figure 5.6: Density gradient contours around the flexible parachute at Mach 1.6; T is a period

canopy behavior, which is related with the drag [3]. From this figure, it can be seen that this curve looks like a wavy line, and the projected frontal area shows an almost linear decrease, because the shock ahead of the canopy is always located near the edge of the canopy during a pulsation cycle (see Fig. 5.2), which leads the edge part to shrink all the time. In addition, the time period of this pulsation cycle is rather small (about 0.00095s), so it seems that the canopy shape shrinks almost linearly in Fig. 5.3. This change causes the corresponding change in drag.

The time history of pressure coefficient at point A (see Fig. 4.1 of Chapter 4) on the canopy surface is shown in Fig. 5.4. This indicates that the pressure inside the

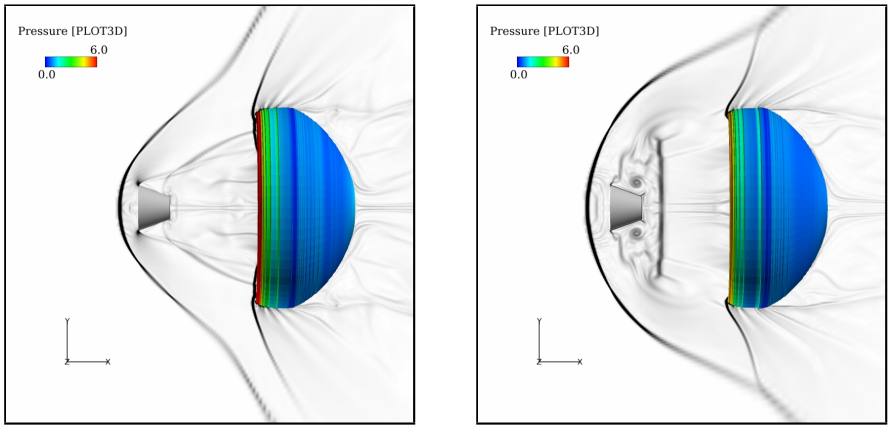

(a) t=4T/9 (b) t=6T/9

Figure 5.7: Density gradient contours around the flexible parachute at Mach 2.1; T is a period

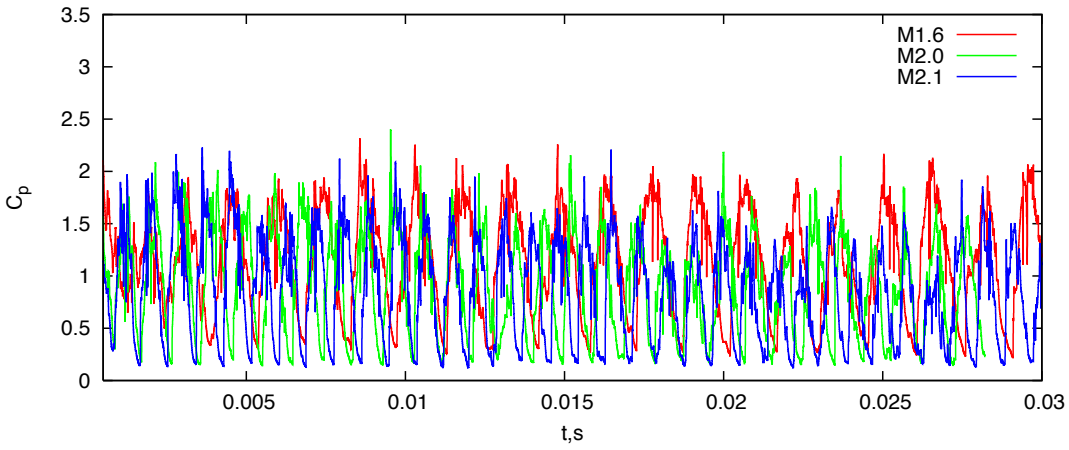

Figure 5.8: Comparison of pressure coefficient at point A (see Fig. 4.1 of Chapter 4) on the canopy surface for the effect of Mach number

canopy changes cyclically. The time history of payload force is shown in Fig. 5.5. From this figure, we can see that after about 0.005s the payload force changes cyclically due to cyclic pressurization in the canopy. In addition, since the aerodynamic interaction occurs far away from the canopy at first, the payload force becomes smaller.

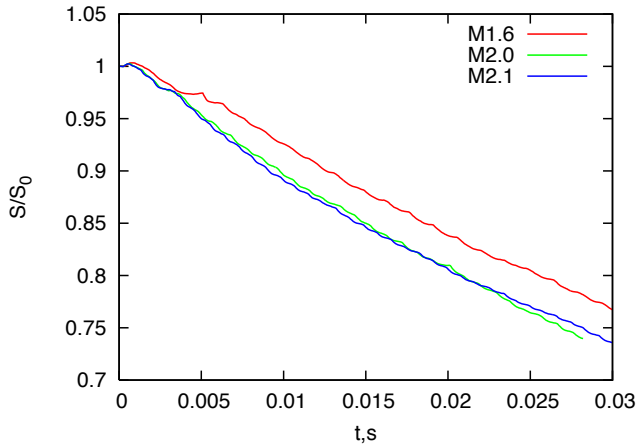

Figure 5.9: Comparison of time variations of projected frontal area of canopy for the effect of Mach number

5.6 Effect of Mach Number

Here in this axisymmetric case, based on the approach for evaluating the effect of Mach number [105] employed in the former cases, computation was carried out at M=1.6 and M=2.1 under the same computational conditions.

The instantaneous flow fields with aerodynamic interactions around the flexible parachute at Mach 1.6 and 2.1 are shown in Fig. 5.6 and Fig. 5.7, respectively. From comparison between the three Mach number cases, it is seen that the case of Mach 1.6 is quite different from the other case. Because the shape of shock and the detachment distance depend on freestream Mach number [108], until t=8T/9 the shock wave ahead of the capsule interacts with the shock wave ahead of the canopy weakly in Fig. 5.6. From Fig. 5.6 and Fig. 5.7, we can see that as Mach number is large, the shock wave ahead of the capsule is more conical, which causes stronger wake/rear shock and fore-shock/rear shock interactions, and that the interaction location is closer to the canopy, which also leads to more severe deformation of the canopy shape, especially in the edge part.

Comparison of the time variation of pressure coefficient at point A (see Fig. 4.1 of Chapter 4) between the three Mach number cases is shown in Fig. 5.8. From this figure, it is observed that the pressure coefficient exhibits the cyclic changes in all the cases. Moreover, at the initial stage (before about 0.005s), at Mach 1.6, its amplitude is

smallest because of the weaker aerodynamic interference; as Mach number is large, the vibration of pressure becomes more severe, which shows more unstable flow fields, due to the stronger aerodynamic interactions. However, after 0.005s, it can be seen that there is a greater vibration in pressure coefficient at Mach 1.6, which illustrates that the aerodynamic interactions becomes stronger, and that the pressure coefficient maintains higher, so that the canopy changes more slowly (see Fig. 5.9). On the other hand, at higher Mach number cases, the canopy shape contracts faster (see Fig. 5.9), which leads to a change in the location of the shock ahead of the canopy and the distance between the canopy and capsule, and weakens the aerodynamic interactions, and causes the pressure coefficient reducing. In addition, it can be seen that the canopy has a faster contraction at Mach 2.1 (than that at Mach 2.0, see Fig. 5.9), which correspondingly increases faster the distance between the canopy and the capsule, leading to a longer pulsation cycle. As a result, the canopy deformation at M2.1 slows down after about 0.02s as shown in Fig. 5.9. Moreover, as the canopy shape becomes smaller and smaller in all the cases (see Fig. 5.9), the pressure coefficient becomes gradually smaller (see Fig. 5.8), although there is a time difference.

5.7 Summary

In this chapter, the axisymmetric flexible parachute models were simulated numerically at supersonic conditions. The results obtained are summarized as follows:

- Time variations of change in the canopy shape for the axisymmetric parachute model were successfully simulated on Cartesian grids using the immersed boundary method together with the weak coupling scheme at supersonic speeds ranging from M=1.6 to M=2.1.

- When the trailing distance between the capsule and canopy was small, the complicated wake/rear shock and foreshock/rear shock interactions were observed in axisymmetric flexible cases. In the unsteady flow mode, the bow shock formed ahead of the capsule periodically inflated and moved radially outward. This was caused by the lateral expansions of complicated wake/rear shock and foreshock/rear shock interactions. However, in the 2D flexible case, only the steady

foreshock and the wake/rear shock interaction were observed because of the weak flow interference and severe deformation of the canopy.

- As Mach number increased, the shock wave ahead of the capsule was more conical, which led to stronger wake/rear shock and foreshock/rear shock interactions, and the interaction location was closer to the canopy. This caused more severe shrinkage deformation of the canopy shape.

- In the axisymmetric flexible case, at Mach 1.6, as the shape of shock was not conical, until t=8T/9 the shock wave ahead of the capsule interacted with the shock wave ahead of the canopy weakly. In the 2D flexible case, at Mach 1.6 the shock wave ahead of the capsule was also not conical and moved upstream under the effect of the cyclic pressurization to canopy. When the canopy shape became much smaller, the foreshock moved downstream.

- The pressure coefficient at Mach 1.6 underwent from weak to strong vibration, which illustrated that the weak aerodynamic interactions turned stronger, and the pressure coefficient maintained higher (than other Mach cases), so that the canopy changed more slowly. On the other hand, as Mach number increased, the vibration of pressure coefficient became from strong to weak, which showed that the strong aerodynamic interactions became weaker, due to the faster canopy shape shrinkage deformation. However, as the canopy shape became smaller and smaller in all the cases examined here, the pressure coefficient became gradually smaller, although there was a time difference.

Chapter 6

Three-Dimension Flexible Parachute

6.1 Introduction

In this chapter, three-dimensional flexible parachute models are numerically simulated at supersonic speeds ranging from M=1.6 to M=2.1. The parachute system adopted here consists of a capsule and a canopy, and the flow fields around the parachute models show strong aerodynamic interactions with complicated flow patterns. The objective of this study is to further confirm that the IBM can be properly applied to solve the supersonic flow over the flexible three-dimensional parachute models, and to further investigate the effect of aerodynamic interference on the performance of the flexible three-dimensional parachute system in detail. Moreover, the effects of Mach number, the trailing distance and canopy to capsule size on the flexible parachute system will be examined.

6.2 Computational Method and Conditions

The present calculation for this case was performed using the in-house structured single block code, where the three-dimensional compressible Navier-Stokes equations were solved to simulate the supersonic flow field around the parachute models. To evaluate the inviscid fluxes, Simple High-resolution Upwind Scheme (SHUS) [74] was employed, and its accuracy was improved by using the 3rd-order MUSCL scheme [78, 79] with

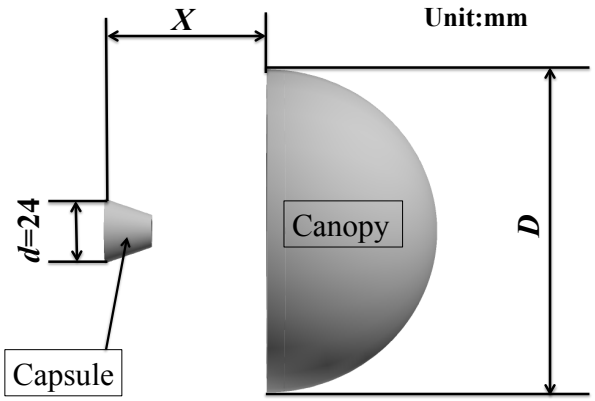

Figure 6.1: Parachute system in the present computation

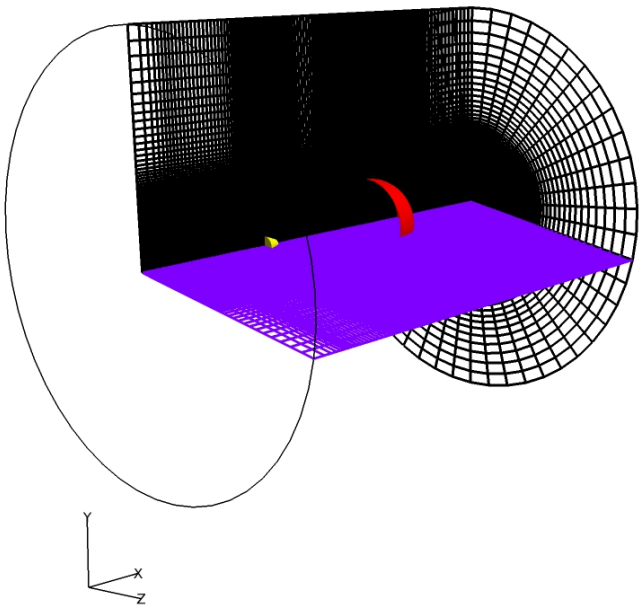

Figure 6.2: Grid for case C (see Table 6.1) in this study, the yellow region refers to the capsule body, and the red region the canopy surface.

the Van Albada flux limiter [80], while viscous terms were calculated by the 2nd-order central differencing scheme. One of features of the present numerical method is use of the 3rd-order total variation diminishing Runge-Kutta scheme [82] for accurate

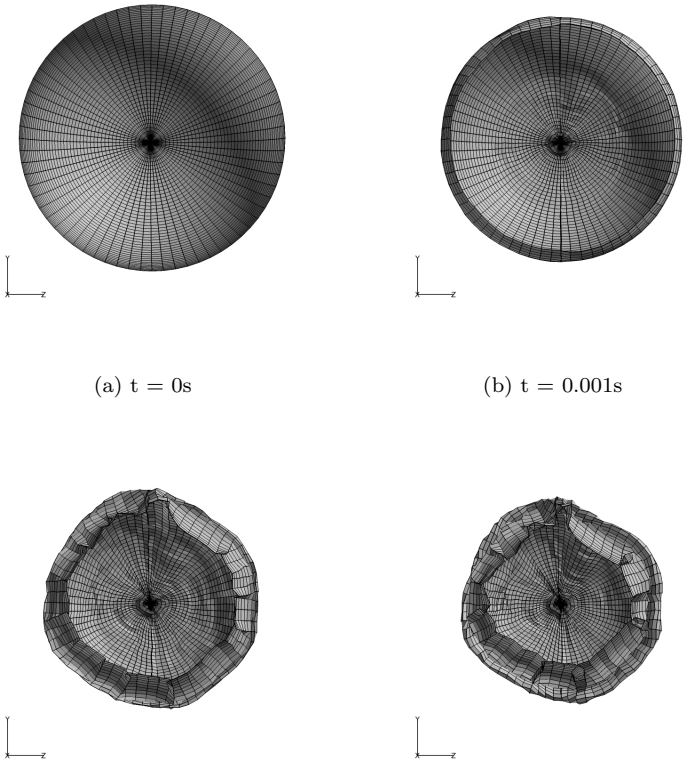

(a) t = 0s

(b) t = 0.001s

(c) t = 0.003s

(d) t = 0.004s

Figure 6.3: Time-variations of canopy shape for case A

unsteady calculation.

The coefficient of viscosity was computed from Sutherland's law [66, 67]. Moreover, initial conditions in the calculations were set to the free stream values, and non-slip and adiabatic conditions were applied to the body surfaces. The freestream conditions used in the current study refer to table 3.1 of Chapter 3.

No turbulence model was employed here to show the results for laminar flow. In the previous study for a rigid parachute (see Chapters 3), turbulence model was not used, the results of which were in good agreement with experimental data obtained at ISAS/JAXA. The flow calculation code for the rigid case was employed here. In addition, we are afraid that at this moment reliable turbulence models were not available for complicated separation flows [99].

In addition, the immersed boundary method [85, 86] was also applied to deal with

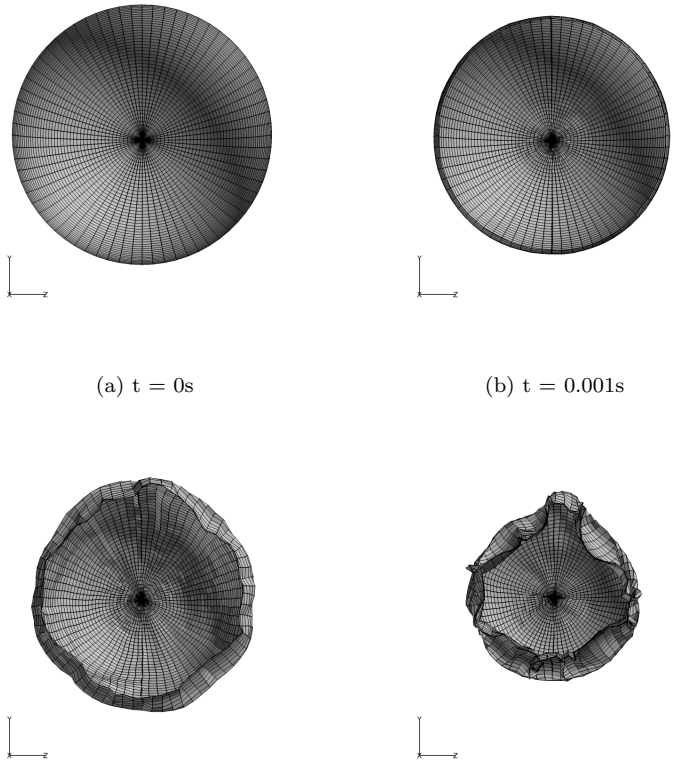

(a) t = 0s (b) t = 0.001s

(c) t = 0.003s (d) t = 0.007s

Figure 6.4: Time-variations of canopy shape for case B

the moving boundary of the three dimensional flexible canopy. The mass-spring-damper (MSD) model [88] was applied to solve the structural dynamics of the parachute. The explicit 2nd-order Runge-Kutta scheme was used to obtain time-variations in the canopy model calculation. Furthermore, the method of weak coupling(see Fig. 2.7 of Chapter 2) was used to compute the three-dimensional flexible parachute case.

6.3 Three-Dimensional Flexible Parachute Model

The three-dimensional parachute model employed here consists of a capsule and a canopy. The flexible canopy is connected by suspension lines to a capsule. The number of suspension lines is about 400, and the effect of these lines refers to section 2.3 of Chapter 2, but the effect on the flow field are not taken into account here. In

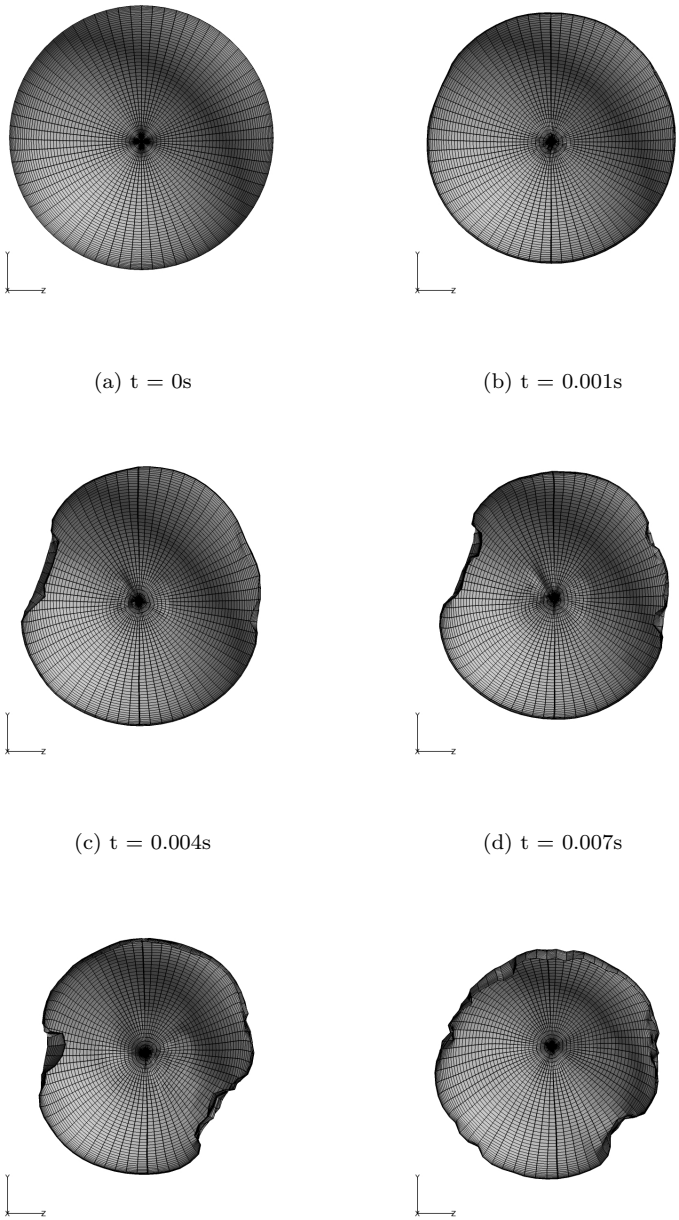

(a) t = 0s

(b) t = 0.001s

(c) t = 0.004s

(d) t = 0.007s

(e) t = 0.0156s

(f) t = 0.0223s

Figure 6.5: Time-variations of canopy shape for case C

addition, the radial reinforcement cables from the canopy apex to the skirt and the canopy porosity have not been considered for the present study, the configuration of

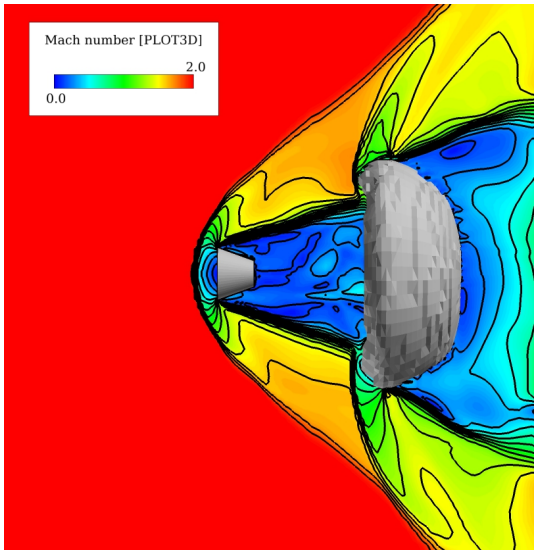

(a) Case A

Figure 6.6: General flow features around the parachute systems. Mach number contours for cases A , B and C at one instant in time(cont'd)

this parachute system is shown in Fig. 6.1, which is basically the same as that of the rigid parachute model employed in the previous rigid case, except the thickness of canopy here is zero in a geometrical sense.

Table 6.1: Specification for three cases A, B and C

Case	X	d	D	X/d	d/D	Grid number
A	57mm	24mm	110mm	2.375	0.218	759, 696
B	114mm	24mm	110mm	4.750	0.218	1, 059, 576
C	171mm	24mm	110mm	7.125	0.218	1, 059, 576

The original shape of canopy is a hemisphere with the diameter D. The capsule is fixed, and the diameter of its frontal surface, d=24mm. It should be noted that the capsule takes a conical form with a half-cone angle of 20 degree (see Fig. 6.1). X is the axial distance from the capsule base (the frontal surface) to the inlet of the canopy, and X/d refers to the parachute trailing distance between the capsule and the canopy. In this study, the trailing distance takes smaller values (from 2.375 to 7.125) than that one of NASA tests (about 10) [57], since under this condition of these values,

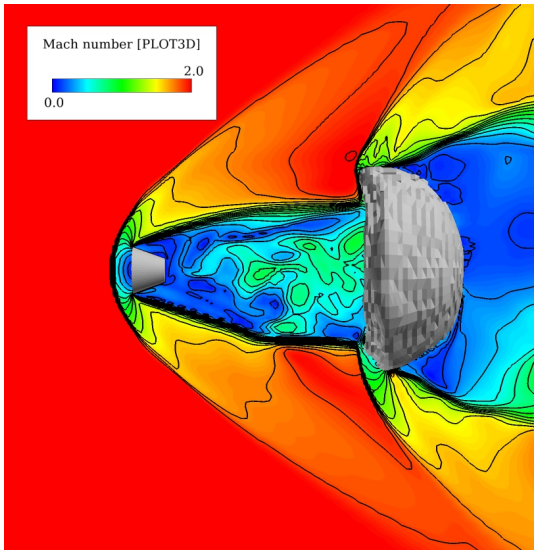

(b) Case B

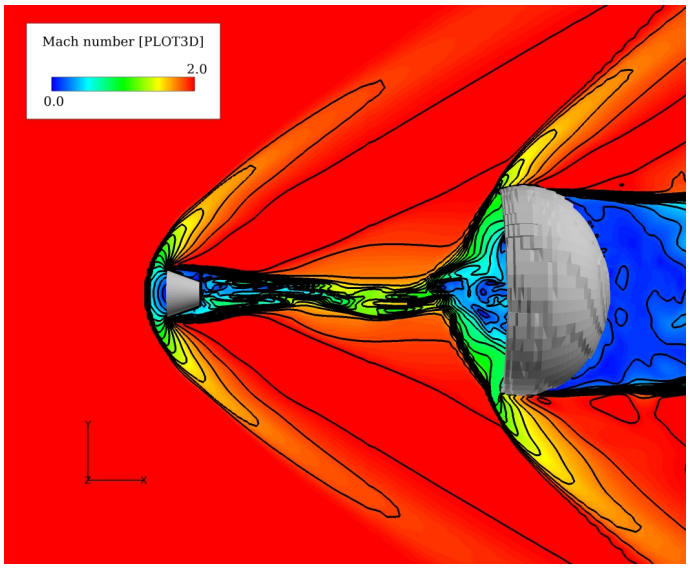

(c) Case C

Figure 6.6: General flow features around the parachute systems. Mach number contours for cases A, B and C at one instant in time

complicated aerodynamic interference was observed in the case of the rigid parachute system in our previous research [86]. Therefore, it seems to be worth examining whether such phenomena will also occur in the case of the three-dimensional flexible parachute

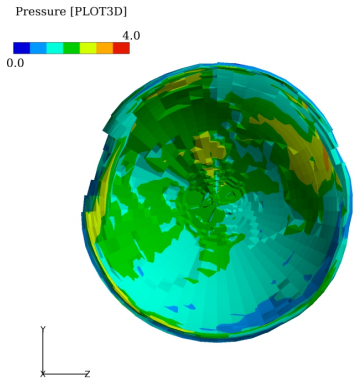

(a) t = 0.0025s

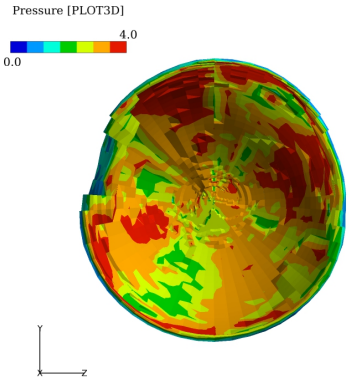

(b) t = 0.0037s

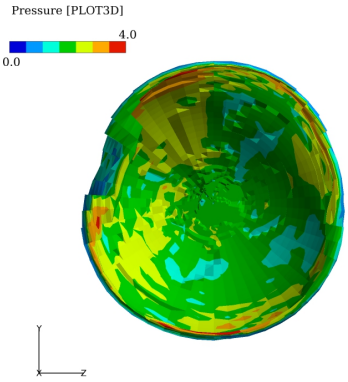

(c) t = 0.0045s

Figure 6.7: Pressure cycle on parachute canopy for case C

system.

6.4 The Effect of Parachute Trailing Distance

Three simulations were conducted to investigate the effect of trailing distance (X/d) on the dynamic behavior of canopy. The values of parachute parameters are listed in Table 6.1. It should be noted that the diameter of canopy was fixed to D=110mm in the three cases.

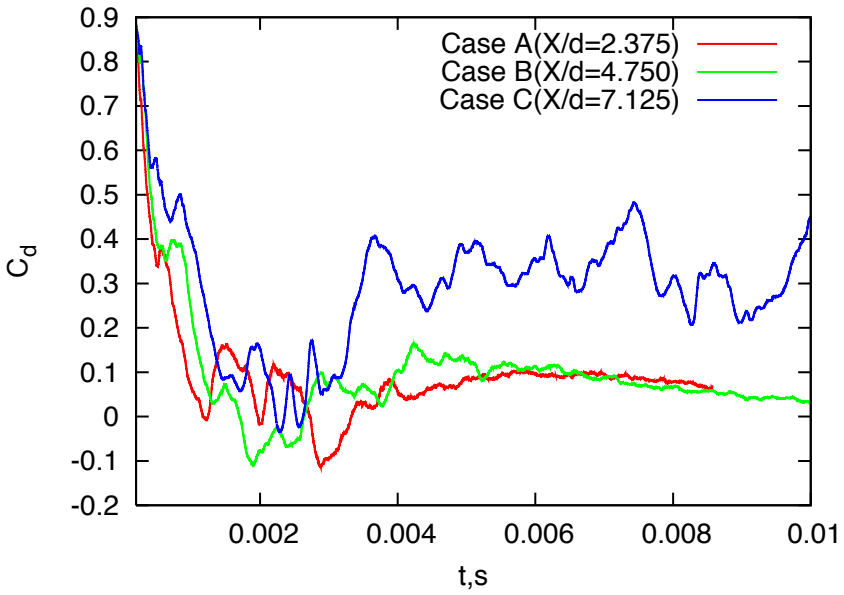

Figure 6.8: The comparison of drag coefficient for cases A, B and C

Because of the axisymmetric configuration for the parachute system, a structured grid with a single-block was generated by a meridional plane. To see grid convergence, we took up the case C as an example and results in two grid cases were compared; a fine case has 3,037,608 grid points, and the baseline case has 1,059,576. Consequently, results of the pressure distribution and flow field seem to show fair agreement between these two cases. To save the calculation time, the baseline grid was employed in this study, as shown in Fig. 6.2, where the grid density in the canopy region was intentionally made large. The control points of the canopy, whose number is 902×441, were searched within this region, and the canopy surface was created as shown in the red region of Fig. 6.2. It should be noted that the number of control points becomes 402×401, as the canopy size decreases in this study. Furthermore, the total number of grid points for the cases in this study take the similar grid densities, which are shown in next sections. It should be noted that in the calculation of examining the effect of Mach number, the grid is the same with that one in case C.

Time-variations of the canopy shape for the three cases are shown in Figs. 6.3-6.5, where we can see the change from the mesh of canopy. It can be found from this comparison that the canopy in the case A experiences severe deformation, and continues to shrink during this time period. The case B also has the similar deformation trend,

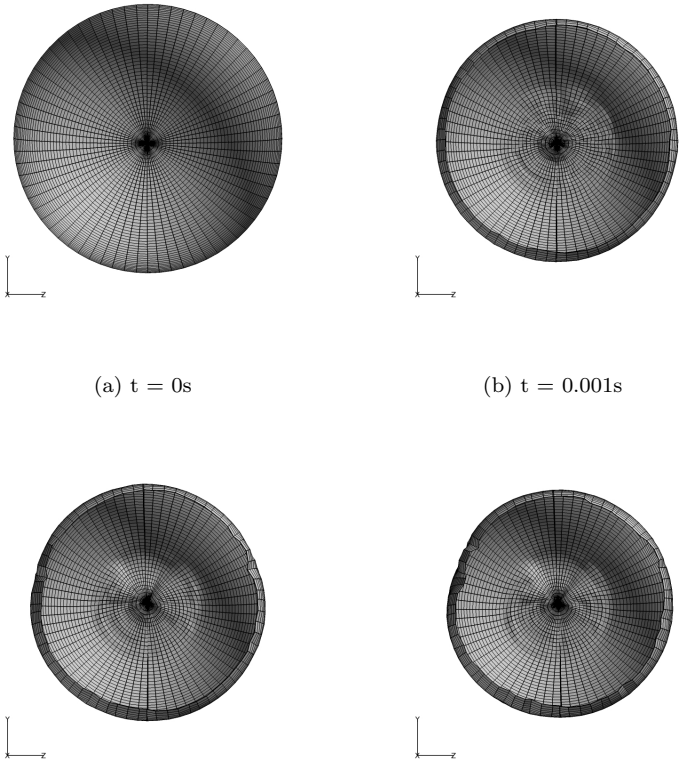

(a) t = 0s (b) t = 0.001s

(c) t = 0.004s (d) t = 0.006s

Figure 6.9: Time-variations of canopy shape for case D

however, the speed of deformation is slower than that in the case A. On the other hand, the phenomenon of the "area oscillation" [12] of the canopy can be observed in the case C, which is quite different from the cases A and B. The causes of these differences will be explained in the following.

For the parachute system located in a supersonic flow, the representative instantaneous flow fields for cases A, B and C are shown in Fig. 6.6. In the case C the canopy shock moves upstream of the parachute mouth, and interacts with the capsule wake, which is a main source of the unsteadiness in the flow field [3, 12]. This causes repetition of the pressure change inside the canopy, as seen in Fig. 6.7.

By contrast, in the cases B the capsule wake interacts with the canopy shock near the canopy edge, which produces a higher pressure outside the canopy, leading to the contraction of the canopy. However, in the initial period of the case B, the canopy shock

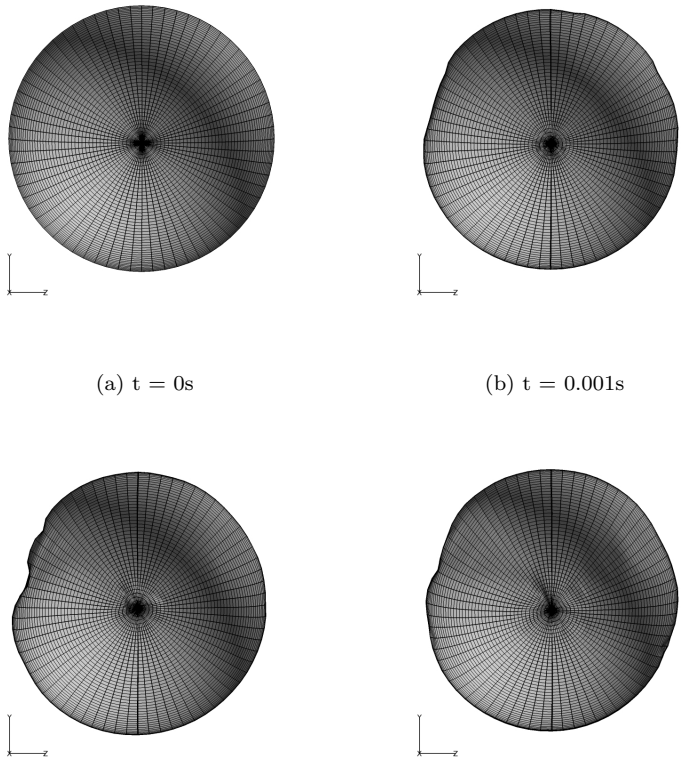

(a) t = 0s (b) t = 0.001s

(c) t = 0.005s (d) t = 0.0097s

Figure 6.10: Time-variations of canopy shape for case E

also moves upstream, and momently interferes with the wake from the capsule, due to the longer distance between the capsule and canopy, which produces the high pressure inside the canopy and slows down deformation of the canopy. After that, the capsule wake grows stronger, and the interference moves close to the parachute, as shown in Fig. 6.6(b). On the other hand, in the case A, it should be pointed out that both the aerodynamic interactions between the capsule wake and the canopy shock, the capsule shock and the canopy shock are simultaneously observed(see Fig. 6.6(a)), due to the shorter trailing distance, which causes that the canopy experiences the fastest severe contraction. This phenomenon of aerodynamic interference is different from the 3D rigid and axisymmetric flexible cases with the same trailing distance.

In all the cases, strong flow instability creates large unsteadiness in the drag force exerted on the canopy. This force acts in the freestream flow direction and was calculated

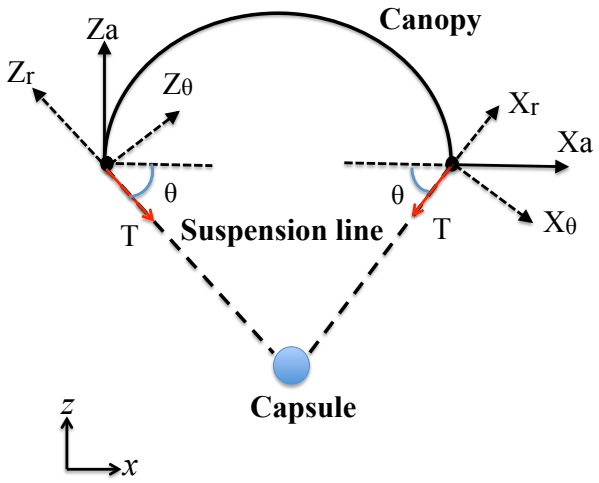

Figure 6.11: Force analysis of edge parts in the cross section (y=0) of the parachute system

from the differences in pressure between the inner and outer canopy surfaces elements. Here, instead of the drag force, the drag coefficient [58] of Eq. 6.1 was examined.

$$C_d = \frac{F_d}{q\frac{1}{4}\pi D^2} \tag{6.1}$$

Here the dynamic pressure q is obtained from the static pressure and Mach number [108], as shown in Eq. 6.2. This agrees with the method of Ref. [59] , where P refers to the freestream pressure, and M the freestream Mach number.

$$q = \frac{\gamma}{2} P M^2 \tag{6.2}$$

Figure 6.8 shows the comparison of the drag coefficient for the three cases. In the initial stages of all three cases, the canopy maintains almost the original, hemispherical shape and severely interacts with the capsule wake, which produces high pressure vibrations inside the canopy, and accordingly causes the change in the drag coefficient. As the pressure tends to the wave trough, the canopy drag coefficient becomes very small, and simultaneously the parachute starts to shrink. After about 0.003s the drag

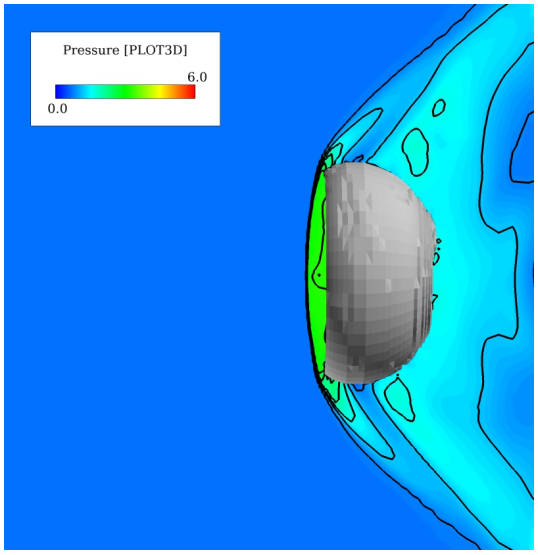

(a) Case D

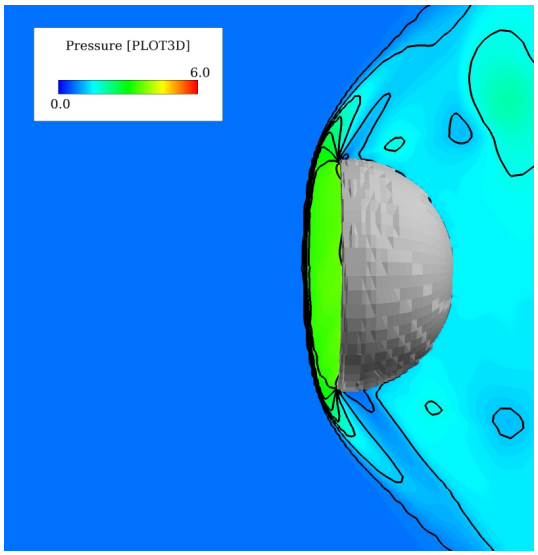

(b) Case E

Figure 6.12: Instantaneous pressure contours around canopy for cases D and E

coefficient of the case C becomes the highest within a periodic change due to the cyclical deformation in canopy shape. In addition, as the trailing distance becomes shorter, the drag coefficient becomes very small and tends to zero owing to the severe canopy deformation.

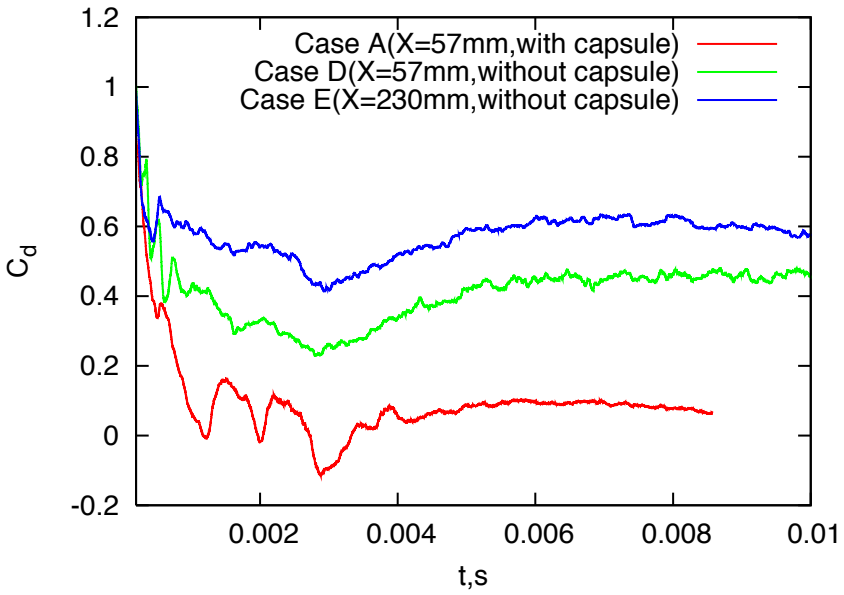

Figure 6.13: Time history of drag coefficient for cases A, D and E

Moreover, as the trailing distance is longer, the period of pressure vibration becomes larger. In the case B, the interaction location has moved from the upstream location to the canopy edge, just like from Fig. 6.6(c) to (b). Thus the change in canopy shape becomes slower, but at length it appears intense and fast, with a change in the resultant drag coefficient. On the other hand, in the case C, the canopy bow shock moves cyclically close to the parachute mouth and upstream of the parachute mouth, and interacts with the wake flow, This produces large pressure fluctuations in the canopy with corresponding variations of the drag coefficient. In short, reasonably increasing the value of trailing distance creates a higher value of the canopy drag coefficient, which agrees with the experimental finding obtained by Reichenau [109].

In addition, the maximum drag coefficient for a realistic supersonic parachute (Huygens, X/d=10, see Ref. [50]) at Mach 2.0 is about 0.46, and its nominal value is about 0.38. On the other hand, in the case C of the present study (X/d=7.125, M=2.0), in the stable phase (after about 0.003s in Fig. 6.8), the maximum drag coefficient is about 0.46, and the mean value is about 0.33. Moreover, as the trailing distance of the present case is smaller than 10, it is reasonable to assume that the drag coefficient of the case C is smaller than that of Huygens [50].

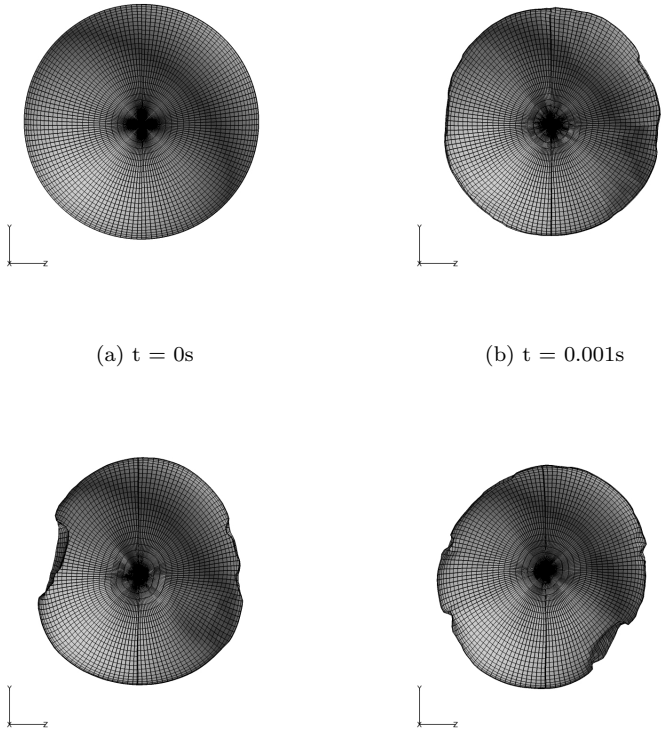

(a) t = 0s (b) t = 0.001s

(c) t = 0.007s (d) t = 0.0135s

Figure 6.14: Time-variations of canopy shape for case F

6.5 The Effect of the Capsule and Canopy Size

6.5.1 Capsule Size

In this section, we consider the case that the capsule has been reduced to a point, where the effect of capsule can be ignored. This model can be used to capture the canopy bow shock and get its drag. Two cases (D and E) are carried out in this study, which are listed in Table 6.2. Here X is the distance from the fixed point (capsule) to the canopy inlet.

Time-variations of the canopy shape for the cases D and E are shown in Figs. 6.9 and 6.10 , respectively. It can be seen from the comparison of the two cases that as X increases, the canopy shape has smaller deformation. In addition, as compared with the case A (X=57mm), the canopy has a very small change in shape in the case D. It is

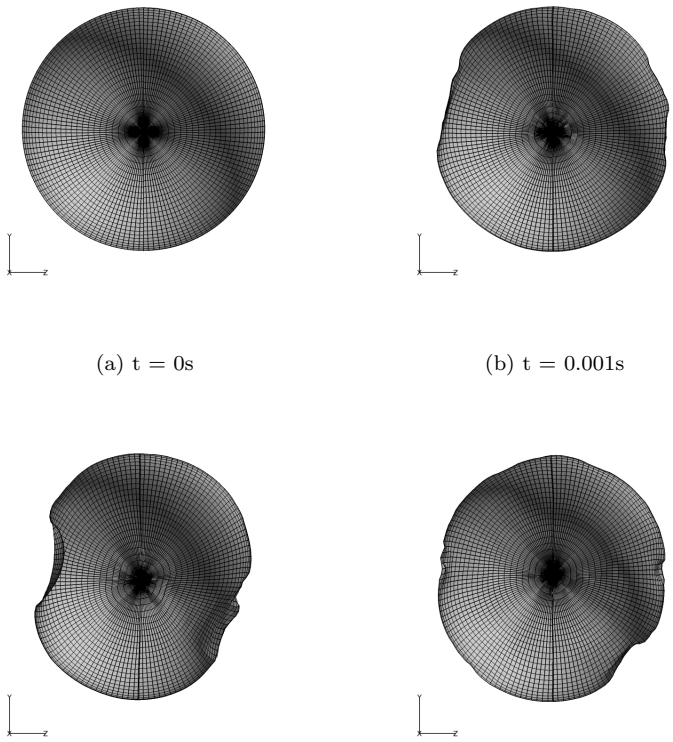

(a) t = 0s (b) t = 0.001s

(c) t = 0.007s (d) t = 0.0137s

Figure 6.15: Time-variations of canopy shape for case G

Table 6.2: Values of parameters for cases D and E

Case	X	d/D	Grid number
D	57mm	0	542,640
E	230mm	0	542,640

clear from this that the capsule wake has a large impact on the parachute performance.

Moreover, in order to more clearly understand the effect of distance X on the parachute performance, the force analysis of edge parts in the cross section (y=0) of the parachute system was made (see Fig. 6.11), where the relations of the forces acting on the control points on the canopy edges are described. They are expressed by Eqs. 6.3 - 6.6.

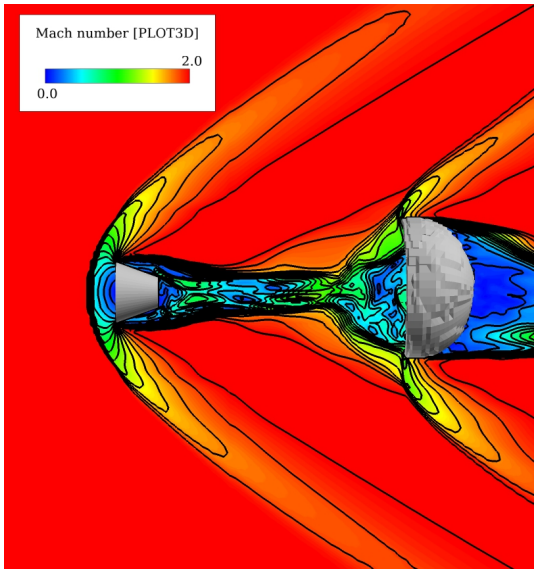

(a) Case F

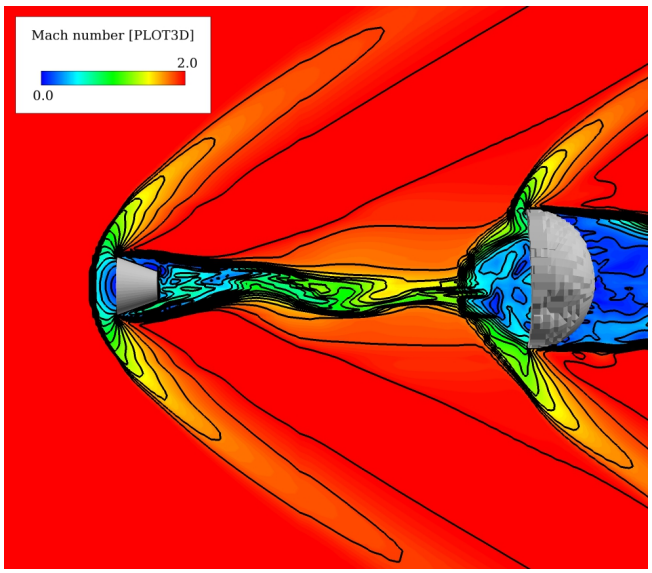

(b) Case G

Figure 6.16: Instantaneous pressure contours around canopy for cases F and G

$$X_a = X_r + X_\theta \tag{6.3}$$

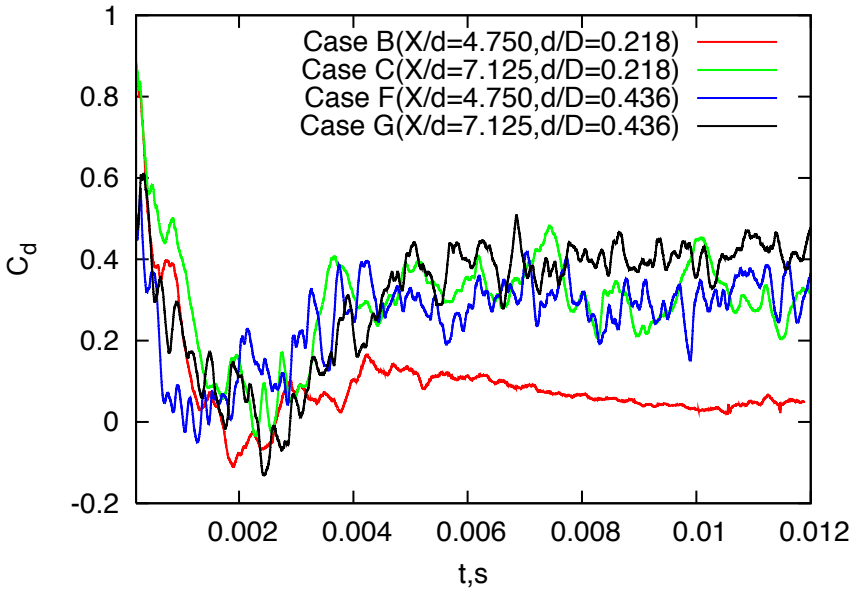

Figure 6.17: Time history of drag coefficient for cases B, C, F and G

$$X_\theta = X_a * sin\theta \tag{6.4}$$

$$Z_a = Z_r + Z_\theta \tag{6.5}$$

$$Z_\theta = Z_a * cos\theta \tag{6.6}$$

In Fig. 6.11, the mass nodes of the canopy edges are compelled to just move along a circular path, with its center placed at the capsule location, since the radial components Xr and Zr of the forces in the x and z directions are equal to the tension force of suspension lines, T. [85]

As the distance from the capsule to the canopy inlet, X, is increased, the angle between the suspension line and the x direction, θ , becomes larger, so that X_θ becomes larger, and Z_θ becomes smaller from Eqs. 6.4 and 6.6, respectively. Therefore, the canopy of the case E (X=230mm) shrinks less than that of the case D (X=57mm).

The representative instantaneous flow fields for the cases D and E are shown in Fig. 6.12, A stationary bow shock is predicted in front of canopy, but its location is different due to the difference in the trailing distance. The shock wave becomes closer

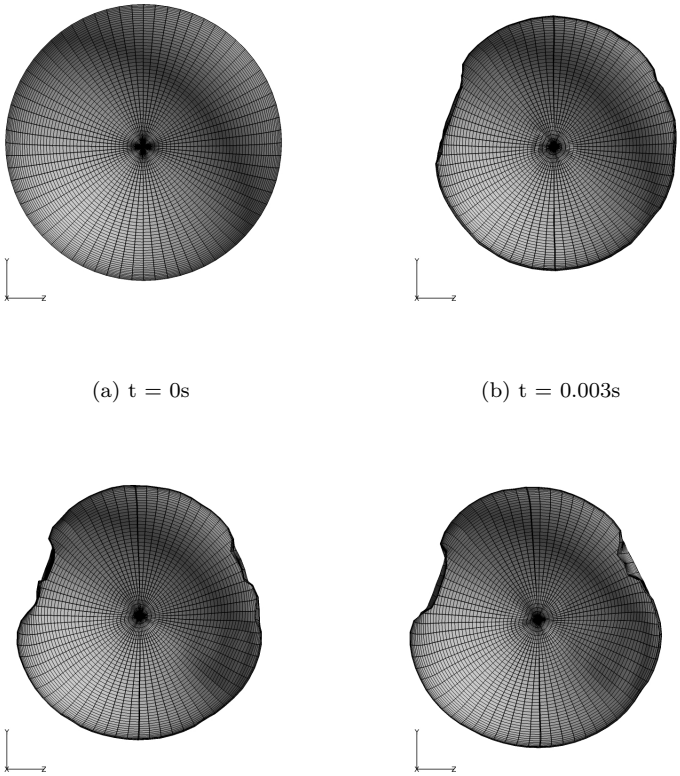

(a) t = 0s

(b) t = 0.003s

(c) t = 0.007s

(d) t = 0.0156s

Figure 6.18: Time-variations of canopy shape for case H

to the canopy edge in the case D, which causes the canopy edge to shrink toward the center. Consequently, the canopy of the case D has a larger contraction.

The time histories of drag coefficient for cases A, D and E are shown in Fig. 6.13. Since the pressure inside the canopy in the cases without capsule is higher than that in the cases with capsule, the drag force in the former becomes higher than that in the latter; the drag coefficients has the same trend, which agrees with the experimental finding in NASA test [12, 55]. In addition, as X increases, the canopy experiences smaller deformation, so that the drag force becomes larger, leading to larger drag coefficient because the reference area used to calculate C_d is a constant, nominal value.

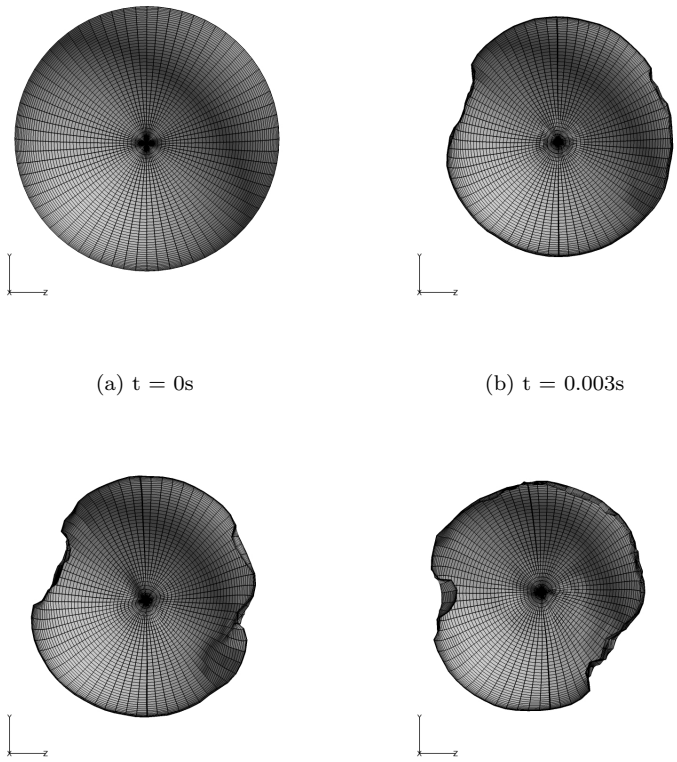

(a) t = 0s (b) t = 0.003s

(c) t = 0.007s (d) t = 0.0156s

Figure 6.19: Time-variations of canopy shape for case I

6.5.2 Canopy Size

In this section, we take into account the effect of canopy size on the canopy behavior. Two cases: F and G were calculated, which are listed in Table 6.3. These cases have a reduced value of the canopy diameter D, compared with the previous cases B and C (see Table 6.1).

Table 6.3: Values of parameters for cases F and G

Case	X	d	D	X/d	d/D	Grid number
F	114mm	24mm	55mm	4.750	0.436	$939,114$
G	171mm	24mm	55mm	7.125	0.436	$939,114$

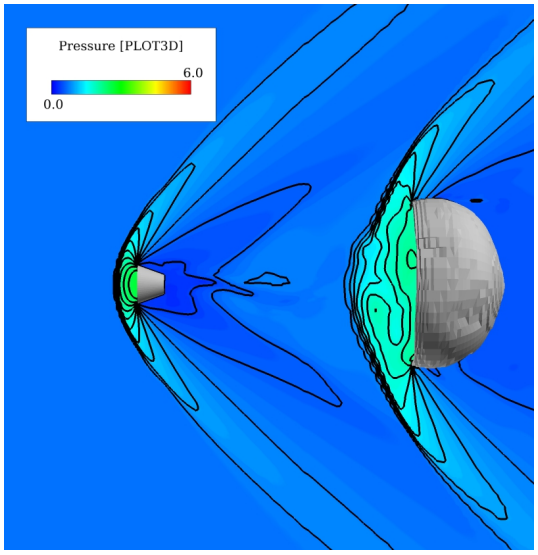

(a) Mach 1.6 (Case H)

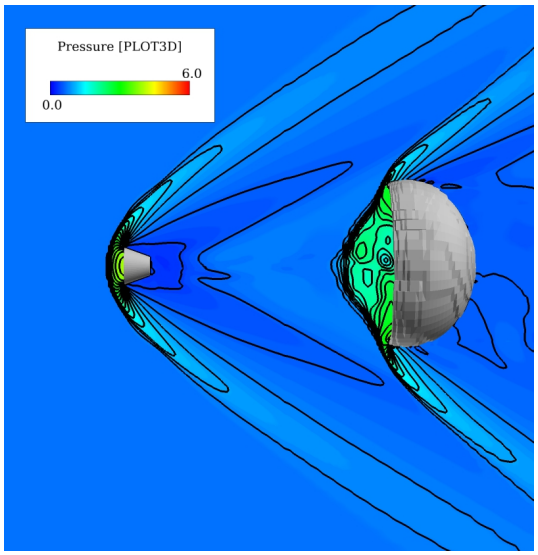

(b) Mach 2.0 (Case C)

Figure 6.20: Instantaneous pressure contours around canopy for cases C, H and I(cont'd)

The time-variations of canopy shape for cases F and G are shown in Figs. 6.14 and 6.15, respectively. Basically, the canopies of the cases F and G are less deformed compared with those of the cases B and C; in particular it is pronounced in the case F. However, the trend in change is similar in the small and large canopies, and the area

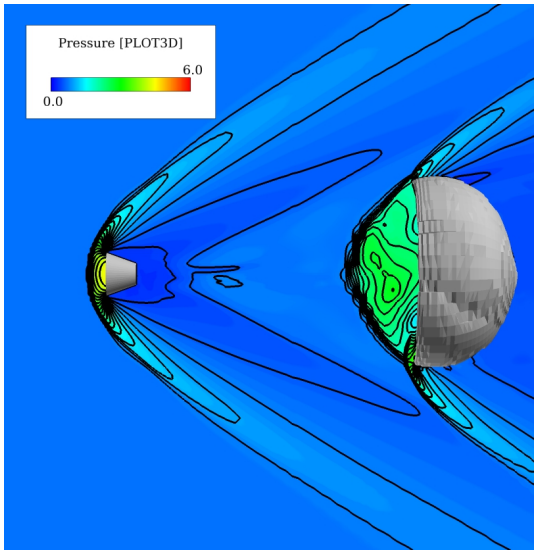

(c) Mach 2.1 (Case I)

Figure 6.20: Instantaneous pressure contours around canopy for cases C, H and I

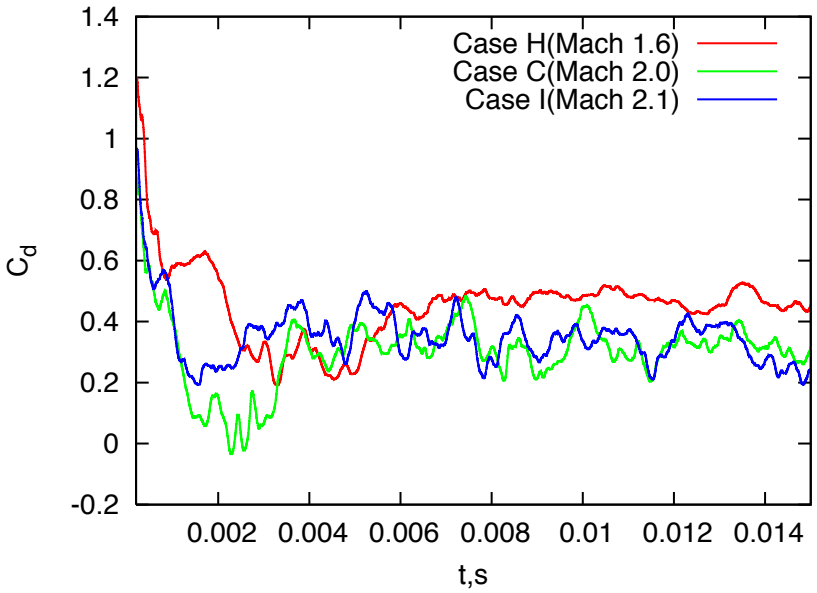

Figure 6.21: Time history of drag coefficient for cases C, H and I

oscillation can be observed in the both cases. Lingard et al. [50] has suggested that the trailing distance should be X/d > 6+D/d, which can avoid the phenomenon observed in cases A or B. Therefore, we need attention to the following. When reducing the canopy

size in the appropriate X/d condition, where for instance, the case B is modified to the case F, it can improve the unfavorable deformation, and prevent the strong coupling of the subsonic flow from the capsule wake with the flow inside the parachute, causing a decrease in pressure (see Fig. 6.6(a) and (b)).

The flow fields for the cases F and G around the parachute system are shown in Fig. 6.16, which suggests that the interaction between the capsule wake and the canopy shock wave is a main source of the unsteadiness in the flow field [3, 12], leading to large pressure fluctuations inside the canopy with a consequential shape change.

The time histories of drag coefficient for cases F and G are shown in Fig. 6.17. As the canopy size decreases, the drag coefficient increases, especially in the smaller trailing distance case. That is to say, they can provide higher values of the drag coefficient (not the drag force).

6.6 The Effect of Mach Number

In experiment, it is difficult to vary Mach number while keeping Reynolds number constant, since Reynolds number increases with the flow speed. However, in computation, this can be easily realized by changing the model size [105]. In this study, based on this approach, the computation was carried out at M=1.6 and M=2.1 under the same computational conditions as case C (see Table 6.1. Here we consider two cases listed in Table 6.4.

Table 6.4: Values of parameters for cases H and I

Case	Mach number	X/d	d/D	Grid number
H	1.6	7.125	0.218	$1,059,576$
I	2.1	7.125	0.218	$1,059,576$

The time-variations of canopy shape for cases H and I are shown in Figs. 6.18 and 6.19, respectively. Compared with the case C with Mach 2.0, we can see that at M=1.6, the canopy undergoes smaller deformation although the Mach 2.1 case has a slightly larger change in canopy shape than the Mach 2.0 case.

The representative, instantaneous flow fields for cases C, H and I are shown in Fig. 6.20. In the higher Mach number cases, the location of the interaction between

the capsule wake and the canopy shock becomes closer to the canopy, and the canopy shock continues to stay near the canopy edge, so that the canopy experiences a severe deformation with vibration.

The time history of drag coefficient for the three cases C, H and I are shown in Fig. 6.21. Mach 1.6 case has a larger drag coefficient, because the smaller change in canopy shape can maintain the higher pressure difference between the inner and outer of the canopy. In the Mach 2.1 case, since the flow has higher energy, the stronger interference causes higher pressure inside the canopy, leading to a higher drag coefficient. After about t=0.004s, there are small differences between the cases C and I with regard to the drag coefficient, since the strong interaction in the Mach 2.1 case causes larger deformation, which mitigates the effect of higher pressure inside the canopy. In conclusion, the parachute drag coefficient reduces with increasing Mach number, which is consistent with the bluff-body flow and Mach dependence in parachute performances in wind tunnel and flight tests [12, 50].

6.7 Summary

In the present study three-dimensional flexible parachute models were numerically simulated using the immersed boundary method at supersonic speeds. The results obtained in this study can be summarized as follows:

- Time-variations of change in canopy shape for three-dimensional flexible parachute models were successfully simulated using the immersed boundary method together with the weak coupling scheme between fluid flow and structure dynamics. The flow speed ranges from M=1.6 to M=2.1.

- In the case with a non-dimensional trailing distance of 7.125 and with a smaller ratio of capsule diameter to canopy diameter, the area oscillation of canopy shape was observed, due to the strong aerodynamic interaction of the capsule wake with the canopy shock, This causes a large drag coefficient. On the other hand, in a rather small trailing distance, the wake plays a more important role in the interference, which causes the canopy shock to continue to stay at the canopy edge part, leading to shrinking of the canopy.

- When we neglect the capsule size, the distance from the fixed point, at which the capsule lies, to the canopy inlet has a big impact on the canopy behavior. As this distance decreases, the canopy shock location moves closer to the canopy, which results in a bigger contraction of canopy shape as well as a smaller drag coefficient. In addition, from comparison between the cases with capsule and without capsule, it was found that the capsule leads to a negative effect on the parachute system.

- Reducing the canopy size under a rather small trailing distance can improve the canopy deformation due to strong aerodynamic interference, and increase the drag coefficient.

- Mach number seriously affects the dynamics of canopy behavior. At Mach 1.6, the canopy shape goes through a smaller deformation than a higher Mach number, because of the weaker interactions between the capsule wake and the canopy shock, which also produces a larger drag coefficient.

- Comparing all the cases in the 3D flexible calculation for the drag coefficient, it was found that two parameters: i.e., the capsule size and the trailing distance, have the largest impact on the drag coefficient of the parachute system. That is, the smaller the capsule size becomes, or the longer the trailing distance becomes, the larger the drag coefficient becomes. In addition, the canopy size has a large effect on the drag coefficient; that is, with a relatively small trailing distance, smaller canopy size can produce larger drag coefficient. On the other hand, in the longest trailing distance cases examined in this study, smaller Mach number can produce larger drag coefficient.

- There are two key factors for the dynamics of the flexible parachute system; one is the unsteady change in canopy shape, and the other the aerodynamic interference between the capsule wake and the canopy shock.

- The performance of the flexible parachute system depends on several factors: i.e., the trailing distance, Mach number, and the ratio of the capsule diameter to the canopy diameter.

- When the trailing distance is rather small, in the 2D flexible case only the steady foreshock and the wake/rear shock interaction were observed because of the weak flow interference and severe deformation of the canopy. In the axisymmetric flexible case the rear shock always stays near the edge part of the canopy, periodically interacting first with the wake and then with the foreshock, and the unsteady flow mode is pulsation. In the 3D flexible case the canopy shock interacts with the wake and foreshock concurrently near the edge part of the canopy during a time period, and the unsteady flow mode is not pulsation.

Chapter 7

Conclusion

The supersonic flow over rigid and flexible parachute models were studied by numerically solving the compressible Navier-Stokes equations. The parachute system employed in the present thesis consists of a capsule and a canopy. In this study the cases with a rather small trailing distance between the capsule and canopy were treated. As a result, the flow field around the parachute system showed complicated wake/shock and/or shock/shock interactions. Moreover, the effects of aerodynamic interference on the performance of the flexible parachute system were analyzed, and the effects of Mach number, the trailing distance, and the ratio of canopy diameter to capsule diameter on the flexible parachute system were also examined in detail. In the following, the wake refers to the capsule wake, the foreshock to the bow shock formed ahead of the capsule, and the rear shock to the bow shock formed ahead of the canopy. The results obtained in this study can be summarized as follows:

Table 7.1: Comparison between rigid and flexible parachute cases with respect to aerodynamic interference for Mach of 2.0 ("○" = occur, "×" = does not occur)

Case	Dimension	X/d	Wake/Shock	Shock/Shock	Pulsation
Rigid	3D	2.375	○	○	○
Flexible	2D	2.375	○	×	×
	Axisymmetric	2.375	○	○	○
	3D	2.375/4.750/7.125	○/ ○ /○	○/ × /×	×/ × /×

- Reducing the trailing distance, X/d, between the capsule and the canopy, the complicated capsule wake/rear shock and foreshock/rear shock interactions were

observed in the 3D rigid, axisymmetric flexible, and 3D flexible cases (see Table 7.1). However, in the 2D flexible case, only the steady foreshock and the wake/rear shock interaction were seen because of the weak flow interference and severe deformation of the canopy.

- The comparison in the 3D rigid parachute case between results of the model A, which has a rod, and the model B, which has no rod, shows that the effects of a connecting rod on the flow field and the pressure distribution on the body surfaces are rather small. The pulsation phenomenon for the model B is identical to that for the model A.

- In the 2D, axisymmetric and 3D cases with the flexible parachute models, time variations of change in the canopy shape as well as the complicated unsteady flow field with aerodynamic interferences were successfully captured at supersonic speeds ranging from M=1.6 to M=2.1. In this simulation the immersed boundary method was employed together with the fluid-structure coupling method. In the 2D, axisymmetric and 3D flexible cases, where the trailing distance was held constant, it was found that with a small trailing distance, the shock ahead of the canopy is always located near the edge part of the canopy, which causes the canopy to shrink all the time. Moreover, it was found that by calculating the 3D flexible canopy case the performance of the flexible parachute can be sufficiently analyzed in terms of the parameters that influence the aerodynamic interference, and that the phenomenon of area oscillation of the canopy can be successfully captured with a large trailing distance.

- Regarding aerodynamic interactions, there are some differences between the rigid (3D) case and the flexible case (axisymmetric and 3D), as shown in Table 7.1. In the rigid case, the rear shock periodically moves upstream and first interacts with the wake and then with the foreshock, where the unsteady flow mode is a pulsation mode. On the other hand, in the axisymmetric flexible case, due to a shrinkage deformation of the edge part of the canopy, the rear shock always stays near the edge part of the canopy, periodically interacting first with the wake and then with the foreshock. In addition, in the 3D flexible case, the capsule wake plays a more significant role in interference as well as a great contraction of the

canopy shape, so that the canopy shock interacts concurrently with the wake and the foreshock near the edge part of the canopy during a time period, where the unsteady flow mode is not a pulsation.

- The unsteady pulsation mode of flow was captured in the three-dimensional rigid case and the axisymmetric flexible case (see Table 7.1), where the bow shock formed ahead of the capsule inflates periodically and moves outward in the radial direction. This is caused by upstream propagation and/or lateral expansion of the complicated wake/rear shock and foreshock/rear shock interactions. There are two key factors for the pulsation phenomenon observed here; one is the pressure difference between the capsule and the canopy, and the other the shear layer and the vortex region produced by the wake/rear shock and the foreshock/rear shock intersections.

- The unsteady flow mode was found to be consistent at supersonic speeds ranging from Mach 1.6 to 2.2 in the 3D rigid case or to 2.1 in the axisymmetric flexible case. In the 3D rigid case, as the freestream Mach number increases, the bow shock formed in front of the capsule moves closer to the capsule, and the capsule wake more strongly interacts with the canopy bow shock. Accordingly, the aerodynamic interaction region comes closer to the center of the parachute system, so that the pressure on the parachute surfaces becomes larger. On the other hand, in the axisymmetric flexible case, as Mach number increases, the pressure inside the canopy undergoes a large change, which causes the canopy shape to deform more with a shrink.

- Reduction in Mach number has a large effect on the performance of the flexible parachute system. In the 2D parachute case, at Mach 1.6, the shock wave formed in front of the capsule is not conical in shape, and moves upstream with a cyclic change of pressure inside the canopy. When the canopy takes a rather small shape, the foreshock moves downstream. In addition, as Mach number decreases, the pressure coefficient on the canopy surface becomes larger. In the axisymmetric flexible case, the pressure coefficient itself oscillates with time and its amplitude changes from small to large at Mach 1.6, which illustrates that the weak aerodynamic interaction turns stronger with the pressure coefficient maintained at a higher value than in other Mach number cases. As a result, the canopy

shape changes more slowly. On the other hand, in the 3D flexible parachute case, the canopy has a smaller deformation than in higher Mach number cases, due to weaker interactions between the capsule wake and the canopy shock. Therefore, in this case the value of drag coefficient becomes higher.

- There are two key factors with respect to dynamics of the flexible parachute system; one is unsteady change in the canopy shape, and the other the aerodynamic interference between the capsule wake and the canopy shock.

- The performance of the flexible parachute system depends on several factors: i.e., the trailing distance, Mach number, and the ratio of the capsule diameter to the canopy diameter.

- From the comparison of all the cases treated in the 3D flexible calculation, it was found that two parameters: i.e., the capsule size and the trailing distance, have the largest impact on the drag coefficient of the parachute system. That is, the smaller the capsule size becomes, or the longer the trailing distance becomes, the larger the drag coefficient becomes. In addition, the canopy size has a large effect on the drag coefficient; that is, with a relatively small trailing distance, smaller canopy size can produce larger drag coefficient. On the other hand, in the longest trailing distance cases examined in this study, smaller Mach number can produce larger drag coefficient.

Bibliography

[1] **NASA-Curiosity Spotted on Parachute by Orbiter**. http://www.nasa.gov/mission_pages/msl/multimedia/pia15978b.html. vii, 2

[2] **NASA-Final Minutes of Curiosity's Arrival at Mars**. http://www.nasa.gov/mission_pages/msl/multimedia/gallery/pia13282.html. vii, 3

[3] K. Karagiozis, R. Kamakoti, F. Cirak, and C. Pantano. **A Computational Study of Supersonic Disk-Gap-Band Parachutes using Large-Eddy Simulation Coupled to a Structural Membrane**. *Journal of Fluids and Structures*, **27**:175–192, 2011. vii, 1, 5, 6, 68, 82, 95

[4] A. Ochi and Y. Nakamura. **A Development of Aerodynamics Analysis Tool using Cartesian System (first report)**. *The Japan Society of Fluid Mechanics 19th CFD symposium (in Japanese)*, 2005. vii, 22, 23

[5] Soltec. *Kyowa Pressure Transducers CAT.204C-U3*. xi, 30, 31

[6] **Mars Science Laboratory Overview**. http://mars.jpl.nasa.gov/msl/mission/overview/. 1

[7] MSL Mission Updates. **Curiosity is on the Surface of Mars and Alive**. http://www.spaceflight101.com/msl-mission-updates-3.html, August 6 2012. 1

[8] M. P. Wernet, R. J. Locke, A. Wroblewski, and A. Sengupta. **Application of Stereo PIV on a Supersonic Parachute Model**. *AIAA Paper 2009-0070*, 2009. 1, 5

[9] J.R. Cruz and J.S. Lingard. **Aerodynamic Decelerators for Planetary Exploration: Past, Present, and Future**. *AIAA Paper 2006-6792*, 2006. 1, 2, 4, 5

[10] B. Raiszadeh, P. Desai, and R. Michelltree. **Mars Exploration Rover Heat Shield Recontact Analysis**. *NF1676L-12664*, 2011. 1

[11] E.M. Queen, J.L. Prince, and P.N. Desai. **Multibody Modeling and Simulation for Mars Phoenix Entry, Descent, and Landing**. *Journal of Spacecraft and Rockets*, **48**(5):765–771, 2011. 1

[12] A. Sengupta. **Fluid Structure Interaction of Parachutes in Supersonic Planetary Entry**. *AIAA Paper 2011-2541*, 2011. 1, 2, 5, 6, 82, 91, 95, 96

[13] D. Dickinson, J. Schlemmer, F. Hicks, F. Michel, and R.D. Moog. **Balloon Launched Decelerator Test Program Post-Flight Test Report BLDT Vehicle AV-1**. *Martin Marietta Corporation TR-3720289*, 1972. 1

[14] R.D. Moog and F.C. Michel. **Balloon Launched Viking Decelerator Test Program Summary Report**. *Martin Marietta Corporation TR-372039*, 1973. 1

[15] D.W. Way, R.W. Powell, A. Chen, A.D. Steltzner, A.M. Martin, P.D. Burkhart, and G.F. Mendeck. **Mars Science Laboratory: Entry, Descent, and Landing System Performance**.

IEEE Aerospace Conference, (Paper Number: 1467), 2006. 2

[16] J.D. Maynard. **Aerodynamics of Decelerators at Supersonic Speeds**. *AIAA Proceedings of the Recovery of Space Vehicles Symposium*, pages 48–54, 1960. 2

[17] C. Johnson. **Investigation of the Characteristics of 6-Foot Drogue-Stabilization Ribbon Parachutes at High Altitudes and Low Supersonic Speeds**. *Technical Report X-448, NASA*, 1960. 2

[18] J.D. Maynard. **Aerodynamic Characteristics of Parachutes at Mach Numbers from 1.6 to 3**. *Technical Report D-752, NASA*, 1961. 2

[19] N. Charczenko. **Wind-Tunnel Investigation of Drag and Stability of Parachutes at Supersonic Speeds**. *Technical Report X-991, NASA*, 1964. 3

[20] N. Houtz. **Optimization of Inflatable Drag Devices by Isotensoid Design**. *First AIAA Annual Meeting*, pages 64–75, 1964. 3

[21] E.E. Davenport. **Static Longitudinal Aerodynamic Characteristics of Some Supersonic Decelerator Models at Mach Numbers of 2.30 and 4.63**. *Technical Report TN D-5219, NASA*, 1969. 3

[22] C. Eckstrom. **Development and Testing of the Disk-Gap-Band Parachute Used for Low Dynamic Pressure Applications at Ejection Altitudes at or Above 200,000 Feet**. *Technical Report CR-502, NASA*, 1966. 3

[23] C. Eckstrom. **Flight Test of a 40-Foot-Nominal-Diameter Disk-Gap-Band Parachute Deployed at a Mach Number of 3.31 and a Dynamic Pressure of 10.6 Pounds per Square Foot**. *Technical Report TM X-1924, NASA*, 1970. 3

[24] C. Eckstrom and J. Preisser. **Flight Test of a 30-Foot-Nominal-Diameter Disk-Gap-Band Parachute Deployed at a Mach Number of 1.56 and a Dynamic Pressure of 11.4 Pounds per Square Foot**. *Technical Report TM X-1451, NASA*, 1967. 3

[25] R. Mayhue and P. Bobbitt. **Drag Characteristics of a Disk-Gap-Band Parachute with a Nominal Diameter of 1.65 Meters at Mach Numbers from 2.0 to 3.0.** *Technical Report TN D-6894, NASA*, 1972. 3

[26] S. Steinberg, P. M. Siemers, and R. III; Slayman. **Development of the Viking Parachute Configuration by Wind-Tunnel Investigation**. *Journal of Spacecraft and Rockets*, **11**(2):101–107, 1974. 4

[27] R. Lundstrom, J. Raper, R. Bendura, and E. Shields. **Flight Tests of Viking Parachute System in Three Mach Number Regimes I: Vehicle Description, Test Operations, and Performance**. *Technical Report TN-D7692, NASA*, 1974. 4

[28] R. Lundstrom, J. Raper, R. Bendura, and E. Shields. **Flight Tests of Viking Parachutes System in Three Mach Number Regimes II: Parachute Test Results**. *Technical Report TN-D7734, NASA*, 1974. 4

[29] E. J. Fallon II. **System Design Overview of the Mars Pathfinder Parachute Decelerator Subsystem**. *AIAA Paper 97-1511*, 1997. 4

[30] A. Witkowski. **Mars Pathfinder Parachute System Performance**. *AIAA Paper 99-1701*, 1999. 4

[31] Y. Taeger and A. Witkowski. **A Summary of Dynamic Testing of the Mars Exploration Rover Parachute Decelerator System**. *AIAA Paper 2003- 2127*, 2003. 4

[32] D. Way, P. Desai, W. Engelung, J. Cruz, and S. Hughes. **Design and Analysis of the Drop Test Vehicle for the Mars Exploration Rover Parachute Structural Tests**. *AIAA Paper 2003- 2138*, 2003. 4

[33] P. Zell, J. Cruz, and A. Witkowski. **Structural Testing of Parachutes in the National Full-Scale Aerodynamics Complex 80- by 120-Foot Wind Tunnel at NASA Ames**. *AIAA Paper 2003- 2130*, 2003. 4

[34] J. Cruz, M. Kandis, and A. Witkowski. **Opening Loads Analyses for Various Disk-Gap-Band Parachutes**. *AIAA Paper 2003- 2131*, 2003. 4

[35] J. Cruz, R. Mineck, D. Keller, and M. Bobskill. **Wind Tunnel Testing of Various Disk-Gap-Band Parachutes**. *AIAA Paper 2003- 2129*, 2003. 4

[36] M. R. Grover, B. D. Cichy, and P. N. Desai. **Overview of the Phoenix Entry, Descent, and Landing System Architecture**. *AIAA Paper 2008-7218*, 2008. 4

[37] J. L. Prince, P. N. Desai, E. M. Queen, and M. R. Grover. **Mars Phoenix Entry, Descent, and Landing Simulation Design and Modeling Analysis**. *Journal of Spacecraft and Rockets*, **48**(5):756–764, 2011. 4

[38] P. N. Desai, J. L. Prince, E. M. Queen, J. R. Cruz, and M. R. Grover. **Entry, Descent, and Landing Performance of the Mars Phoenix Lander**. *AIAA-2008-7346*, 2008. 4

[39] E. M. Queen, J. L. Prince, and P. N. Desai. **Multibody Modeling and Simulation for Mars Phoenix Entry, Descent, and Landing**. *Journal of Spacecraft and Rockets*, **48**(5):765–771, 2011. 4

[40] P. C. Klimas. **Internal Parachute Flows**. *Journal of Aircraft*, **9**(4):313–314, 1972. 4

[41] P. C. Klimas. **Fluid Mass Associated With an Axisymmetric Parachute Canopy**. *Journal of Aircraft*, **14**(6):577–580, 1977. 4

[42] P. C. Klimas. **Inflating Parachute Differential Pressures**. *Journal of Aircraft*, **16**(12):861–862, 1979. 4

[43] L. Poole. **Effects of Suspension-Line Damping on LADT 3 and Supersonic BLDT Parachute Inflation Dynamics**. *Technical Report LWP-1050, NASA*, 1972. 4

[44] W. M. Mullins, D. T. Reynolds, K. G. Lindh, and M. R. Bottorff. **Investigation of Prediction Methods for the Loads and Stresses of Apollo Type Spacecraft Parachutes. Volume 2: Stresses**. *NASA-CR-134231*, 1970. 4

[45] S.K. Ibrahim and R.A. Engdahl. **Parachute Dynamics and Stability Analysis**. *NASA-CR-120326*, 1974. 4

[46] J. M. Nelsen. **Computational Fluid Dynamics Studies of Solid and Ribbon 12-Gore Parachute Canopies in Subsonic and Supersonic Flow**. *AIAA Paper 95-1558*, 1995. 4

[47] R. Lafarge, J. Nelsen, and K. Gwinn. **A Novel CFD/structural Analysis of a Cross Parachute**. *AIAA Paper 1994-752*, 1994. 5

[48] A. Taylor, B. Tutt, and J. Sanders. **On the Application of Explicit Finite Element Analysis and Coupled Fluid/Structure Simulations As They Apply to Escape and Recovery Systems**. *41st Annual survival and flight equipment association symposium, Jacksonville, Florida*, pages 78–87, 2003. 5

[49] J. Lingard and M. Darley. **Simulation of Parachute Fluid Structure Interaction in Supersonic Flow**. *AIAA Paper 2005-1607*, 2005. 5

[50] J. Lingard, M. Darley, and J. Underwood. **Simulation of Mars Supersonic Parachute Performance and Dynamics**. *AIAA Paper 2007-2507*, 2007. 5, 86, 94, 96

[51] M. Barnhardt, T. Drayna, I. Nompelis, G. Candler, and W. Garrard. **Detached Eddy Simulations of the MSL Parachute at Supersonic Conditions**. *AIAA Paper 2007-2529*, 2007. 5, 6

[52] V. Gidzak, M. Barnhardt, T. Drayna, I. Nompelis, G.V. Candler, and W. Garrard. **Simulation of Fluid-Structure Interaction of the Mars Science Laboratory Parachute**. *AIAA Paper 2008-6910*, 2008. 5

[53] V. Gidzak, M. Barnhardt, T. Drayna, I. Nompelis, G.V. Candler, and W. Garrard. **Comparison of Fluid-Structure Interaction Simulations of the MSL Parachute with Wind Tunnel Tests**. *AIAA Paper 2009-2971*, 2009. 5

[54] A. Sengupta, A. Steltzner, K. Comeaux, G. Candler, C. Pantano, and J. Bell. **Supersonic Delta Qualification by Analysis Program for the Mars Science Laboratory Parachute Decelerator System**. *AIAA-2007-2542*, 2007. 5

[55] A. Sengupta *et al*. **Results from the Mars Science Laboratory Parachute Decelerator System Supersonic Qualification Program**. *Aerospace Conference, 2008 IEEE*, 2008. 5, 91

[56] A. Sengupta, J. Roeder, R. Kelsch, M. Wernet, M. Kandis, and A. Witkowski. **Supersonic Disk Gap Band Parachute Performance in the Wake of a Viking-Type Entry Vehicle from Mach 2 to 2.5**. *AIAA Paper 2008-6217*, 2008. 5

[57] A. Sengupta, A. Steltzner, A. Witkowski, G. Candler, and C. Pantano. **Findings From the Supersonic Qualification Program of the Mars Science Laboratory Parachute System**. *AIAA Paper 2009-2900*, 2009. 5, 6, 78

[58] A. Sengupta, R. Kelsch, J. Roeder, M. Wernet, A. Witkowski, and M. Kandis. **Supersonic Performance of Disk-Gap-Band Parachutes Constrained to a 0-Degree Trim Angle**. *Journal of Spacecraft and Rockets*, **46**(6):1155–1163, 2009. 5, 6, 84

[59] A. Sengupta, M. Wernet, J. Roeder, R. Kelsch, A. Witkowski, and T. Jones. **Supersonic Testing of 0.8 m Disk Gap Band Parachutes in the Wake of a 70 deg Sphere Cone Entry Vehicle**. *AIAA Paper 2009-2974*, 2009. 5, 6, 84

[60] M.D. Barnhardt. *Modeling and Simulation of High-Speed Wake Flows*. Doctor thesis of the University of Minnesota, 2009. 6

[61] F. Kozo. *Numerical Methods for Computational Fluid Dynamics (in Japanese)*. University of Tokyo Press, 1994. 9, 12, 13, 18

[62] J. Anderson. *Introduction to Computational Fluid Dynamics*. McGraw Hill, N.Y., 1995. 9

[63] J. Blazek. *Computational Fluid Dynamics: Principles and Applications*. Elsevier Science, 2001. 10

[64] T. C. Papanastasiou, G. C. Georgiou, and A. N. Alexandrou. *Viscous Fluid Flow*. CRC Press, 2000. 10

[65] G.G. Stokes. **On the Theories of Internal Friction of Fluids in Motion**. *Transactions of the Cambridge Philosophical Society*, **8**:287–305, 1845. 11

[66] W. Sutherland. **The Viscosity of Gases and Molecular Force**. *Philosophical Magazine Series 5*, **36**:507–531, 1893. 11, 28, 53, 63, 75

[67] K. Kitamura. *Numerical Analysis on Hypersonic Shock Interacting Flow (in Japanese)*. Doctor thesis of Nagoya University, 2008. 11, 28, 53, 63, 75

[68] Mohamed El-Ghandour. *The Effect of Tip Clearance Geometry on the Leakage Flow in Axial Turbine Cascades*. Doctor thesis of Nagoya University, 2010. 11

[69] J. D. Anderson JR. *Computational Fluid Dynamics the Basic with Application*. McGraw Hill, 1995. 12, 19

[70] K. A. Hoffmann and S. T. Chiang. *Computational Fluid Dynamics*. Engineering Education System, 2000. 12

[71] Mahmoud Moustafa Mahmoud El-GENDI. *Effect of Trailing Edge Geometry on the Flow Behavior Through Rectilinear Turbine Cascades*. Doctor thesis of Nagoya University, 2010. 13

[72] B. Mohammadi. *Fluid Dynamics Computation with NSC2KE an User-Guide Release 1.0*. National Institute for Research in Computer Science and Control, 1994. 14

[73] P. C.E. Jorgenson and C.Y. Lon. **Computing Axisymmetric Jet Screech Tones Using Unstructured Grid**. *AIAA Paper 2002-3889*, 2002. 14

[74] E. Shima and T. Jounouchi. **"Role of CFD in Aeronautical Engineering (No.14) - AUSM Type Upwind Schemes-,"**. 1996. 15, 16, 28, 52, 73

[75] M.S. Liou and C.J. Steffen Jr. **A New Flux Splitting Scheme**. *Journal of Computational Physics*, **107**:23–39, 1993. 15

[76] S. Teramoto. *Computational Study on the Dynamic Stability of a Blunt Reentry Capsule at Transonic Speed*. Doctor thesis of The Institute of Space and Astronautical Science, 2000. 15, 16

[77] K. Kitamura and E. Shima. **A New Pressure Flux for AUSM-Family Schemes for Hypersonic Heating Computations**. *AIAA Paper 2011-3056*, 2011. 15, 17, 18, 63

[78] B. van Leer. **Toward the Ultimate Conservative Difference Scheme.IV. A New Approach to Numerical Convection**. *Journal of Computational Physics*, **23**:276–299, 1977. 15, 28, 52, 63, 73

[79] B. van Leer. **Toward the Ultimate Conservative Difference Scheme.V. A Second-Order Sequel to Godunovs**

Method. *Journal of Computational Physics*, **32**:101–136, 1979. 15, 28, 52, 63, 73

[80] W. K. Anderson, J. L. Thomas, and B. van Leer. **Comparison of Finite Volume Flux Vector Splitting for the Euler Equations**. *AIAA Journal*, **24**:1453–1460, 1986. 15, 28, 52, 63, 74

[81] K. Kitamura, K. Fujimoto, and E. Shima. **Performance of Low-Dissipation Euler Fluxes and Preconditioned Implicit Schemes in Low Speeds**. *AIAA Paper 2010-1272*, 2010. 15, 16, 18

[82] C.-W. Shu and S. Osher. **Efficient Implementation of Essentially Non-Oscillatory Shock-Capturing Schemes**. *Journal of Computational Physics*, **77**:439–471, 1988. 18, 28, 53, 74

[83] C. Tenaud, E. Garnier, and P. Sagaut. **Evaluation of Some High-Order Shock Capturing Schemes for Direct Numerical Simulation of Unsteady Two-Dimensional Free Flows**. *International Journal for Numerical Methods in Fluids*, **33**:249–278, 2000. 18

[84] S. C. Lo, G. A. Blaisdell, and A.S. Lyrintzis. **High-Order Shock Capturing Schemes for Turbulence Calculations**. *AIAA Paper 2007-827*, 2007. 18

[85] M. Miyoshi, T. Ishii, A. Hashimoto, K. Mori, and Y. Nakamura. **Computational Analysis of Parachute Motion using the Immersed Boundary Method**. *AIAA Paper 2008-311*, 2008. 19, 22, 23, 53, 65, 75, 90

[86] X. Xue, H. Koyama, and Y. Nakamura. **Numerical Simulation on Supersonic Aerodynamic Interference for Rigid and Flexible Parachutes**. *AIAA Paper 2012-3269*, 2012. 19, 22, 53, 65, 75, 79

[87] X. Xue and Y. Nakamura. **Computational Analysis of Supersonic Flexible Parachute using Immersed Boundary Method**. *International Journal of Aerospace and Lightweight Structures*, **1**(2):283–299, 2011. 19

[88] R.J. Benney and K.R. Stein. **Computation Fluid-Structure Interaction Model for Parachute Inflation**. *Journal of Aircraft*, **33**:730–736, 1996. 19, 53, 65, 76

[89] W. Huang, C. B. Chang, and H. J. Sung. **An Improved Penalty Immersed Boundary Method for Fluid-Flexible Body Interaction**. *Journal of Computational Physics*, **230**:5061–5079, 2011. 19

[90] M. Miyoshi, K. Mori, and Y. Nakamura. **Numerical Simulation of Parachute Inflation Process by IB Method (in Japanese)**. *Transactions of JSASS*, **57**(670):419–425, 2009. vii, 19, 21, 22, 23, 24

[91] C. W. Hirt, A.A. Amsden, and J.L. Cook. **An Arbitrary Lagrangian-Eulerian Computing Method for All Speeds**. *Journal of Computational Physics*, **14**:227–253, 1974. 20

[92] R. V. Loon, P.D. Anderson, and F.N. Vosse. **A Fluid-Structure Interaction Method with Solid-Rigid Contact for Heart Valve Dynamics**. *Journal of Computational Physics*, **217**:806–823, 2006. 20

[93] T.E. Tezduyar, M. Behr, and J. Liou. **A New Strategy for Finite Element Computations Involving Moving Boundaries and Interfaces–The**

Deforming-Spatial-Domain/Space-Time Procedure: I. the Concept and the Preliminary Numerical Tests. *Computer Methods in Applied Mechanics and Engineering*, **94**:339–351, 1992. 21

[94] Y. Kim and C.S. Peskin. **2-D Parachute Simulations by the Immersed Boundary Method**. *SIAM Journal on Scientific Computing*, **28**(6):2294–2312, 2006. 21

[95] Y. Kim and C.S. Peskin. **3-D Parachute Simulation by the Immersed Boundary Method**. *Computers & Fluids*, **38**:1080–1090, 2009. 21

[96] J. Kim and X. Li. **Simulation of Parachute FSI using the Front Tracking Method**. *Journal of Fluid and Structures*, **37**:100–119, 2013. 21

[97] A. Hashimoto. *Numerical Simulation of Panel Flutter with a Fluid-Structure Coupled Scheme*. Doctor thesis of Nagoya University, 2007. 25

[98] M. Razzaq. *Finite Element Simulation Techniques for Nonlinear Incompressible Fluid-Structure Interaction with Application to Bio-Engineering and Optimization*. Doctor thesis of University of Dortmund, 2011. 24

[99] M. Rahman and C.A. Brebbia. *Advances in Fluid Mechanics VIII*. WIT Press, 2010. 28, 75

[100] D. Feszty, K.J. Badcock, and B.E. Richards. **Driving Mechanisms of High-Speed Unsteady Spiked Body Flows, Part 1: Pulsation Mode**. *AIAA Journal*, **42**:95–106, 2004. 29, 33, 42, 44, 46

[101] F. M. White. *Fluid Mechanics (4th ed.)*. McGraw Hill, 1999. 31

[102] A.G. Panaras and D. Drikakis. **High-Speed Unsteady Flows Around Spiked-Blunt Bodies**. *Journal of Fluid Mechanics*, **632**:69–96, 2009. 33, 67

[103] M. Kenworthy. *A Study of Unstable Axisymmetric Separation in High Speed Flows*. Ph.D. Dissertation, Dept. of Aerospace and Ocean Engineering, Virginia Polytechnic Inst. and State Univ., Blacksburg, VA., 1978. 33

[104] V.I. Zapryagaev and I.N. Kavun. **Experimental Study of the Reverse Flow in the Forward Separation Region in a Pulsation Flow Around a Spiked Body**. *Journal of Applied Mechanics and Technical Physics*, **48**:492–500, 2007. 42

[105] T. Nonomura, H. Muranaka, and K. Fujii. **Computational Analysis of Mach Number Effects on the Edgetone Phenomenon**. *AIAA Journal*, **48**(6):1248–1251, 2010. 48, 59, 70, 95

[106] S.W. Kang. *An Improved Immersed Boundary Method for Computation of Turbulent Flows with Heat Transfer*. Ph.D. thesis, Department of Mechanical Engineering, Stanford University, Stanford, 2008. 53

[107] Jr John D. Anderson. *Modern Compressible Flow: With Historical Perspective (2nd Edition)*. McGraw-Hill, 1990. 56

[108] H.W. Liepmann and A. Roshko. *Elements of Gasdynamics*. Dover Publications Inc. First South Asian Edition, New Delhi, 2007. 61, 70, 84

[109] D.E. Reichenau. **Aerodynamic Characteristics of Disk-Gap-Band Parachutes in the Wake of Viking Entry Forebodies at Mach Numbers from 0.2 to 2.6**. *AEDC-TR-72-78, Arnold AFB, Tennessee*, 1972. 86

List of Publications

Journal article

1. X. Xue, and Y. Nakamura, **"Computational Analysis of Supersonic Flexible Parachute using Immersed Boundary Method,"** International Journal of Aerospace and Lightweight Structures, Vol. 1, No. 2, pp. 283-299, 2011
2. X. Xue, H. Koyama, and Y. Nakamura, **"Numerical Simulation on Supersonic Aerodynamic Interaction of A Parachute System,"** Transactions of the Japan Society for Aeronautical and Space Sciences, Aerospace Technology Japan, Vol. 11, pp.33-42, 2013
3. X. Xue, and Y. Nakamura, **"Numerical Simulation of Three-Dimensional Flexible Parachute System at Supersonic Conditions,"** Transactions of the Japan Society for Aeronautical and Space Sciences, Aerospace Technology Japan (accepted)

Conference

1. X. Xue, H. Koyama, and Y. Nakamura, **"Numerical Simulation on Supersonic Aerodynamic Interference for Rigid and Flexible Parachutes,"** 42nd AIAA Fluid Dynamics Conference and Exhibit, 25-28 June 2012, New Orleans, Louisiana, AIAA Paper 2012-3269.